

POLITECNICO DI MILANO
Scuola di Ingegneria Industriale e dell'Informazione
Corso di Laurea Magistrale in Ingegneria Aeronautica



Design and dynamic modeling of a VTOL UAV

Advisor: Prof. Marco LOVERA
Co-Advisor: Dr. Mattia GIURATO
Dr. Simone PANZA

Thesis by:
Nicolò BATTAINI Matr. 900120

Academic Year 2018–2019

A papà Giuseppe e zio Paolo

Acknowledgments

Con questa tesi termino i miei studi universitari; voglio quindi ringraziare chi mi ha accompagnato e sostenuto in questo percorso.

Il primo ringraziamento va al mio relatore, il professor Marco Lovera, per avermi offerto la possibilità di lavorare ad un progetto entusiasmante, avermi seguito nel suo sviluppo e per il tempo dedicatomi nonostante i numerosi impegni. A Simone, per la grande disponibilità e pazienza nel seguire questa tesi e a Mattia, per aver messo a disposizione la sua abilità ed esperienza per quanto riguarda gli aspetti pratici della progettazione e costruzione.

Il secondo ringraziamento va ai miei amici, a quelli che conosco da sempre e a quelli che ho conosciuto in università: nominarne alcuni vorrebbe dire dimenticare altri, e ciò non è giusto. Grazie a tutti voi per i bei momenti passati insieme. Un particolare ringraziamento agli amici conosciuti al Politecnico, sia in triennale che magistrale, per aver reso questi anni di studio migliori: senza di voi sarebbe stato tutto più difficile.

Infine, il ringraziamento più importante va alla mia famiglia e ai miei parenti: grazie per avermi supportato e sopportato in questi anni, fino a raggiungere questa meta. Un grazie quindi alla mamma che mi è sempre vicina, a mio fratello con cui ho sempre il piacere di confrontarmi e a te papà che sicuramente avresti voluto vedere questo giorno. Grazie per tutto quello che mi hai insegnato.

Abstract

Nowadays unmanned aerial vehicles (UAVs) are widely studied and manufactured. The first thing everyone associates with the word UAV is the idea of a multi-rotor machine, generally a quad-rotor. This is only one side of the coin: besides multi-rotors there are also fixed-wing UAVs. The two categories of UAVs can be overlapped, obtaining the so-called VTOL UAV: an aircraft capable of vertical take-off and landing (from which the name VTOL) and high energy efficiency horizontal flight, which makes it suitable for medium/long range missions. Given that multi-rotors have been studied in detail and have shown their limitations in terms of flight endurance and, on the other hand, fixed-wing UAVs do not possess vertical take-off and landing capability, VTOL UAVs join the advantages of both configurations and can be the right aircraft for lots of applications, both commercial and military: parcel delivery, aerial mapping, reconnaissance and maintenance, just to mention a few examples.

The objective of this thesis is to develop from scratch a VTOL UAV: starting from a basic set of requirements the whole aircraft design is carried out leading to the technical drawings ready for prototyping. The design procedure adopted follows the conventional phases: conceptual, preliminary, detailed and production. The aircraft is developed considering its aerodynamics, the structure and the internal components (very important given the unmanned nature of the aircraft). Last but not least the propulsion system is studied; this is an important element that characterizes a VTOL machine which has to fly both like a conventional aircraft and like a rotorcraft. Starting from a set of linear time invariant (LTI) models, a linear parameter varying (LPV) model is developed using the aircraft speed as scheduling parameter. The LPV model can be used for control and simulation purposes in the full flight envelope of the aircraft. The natural conclusion of the thesis would be the prototyping of the developed design; however, due to the COVID-19 pandemic it has not been possible to conduct this activity in the laboratories of Politecnico di Milano.

The final output of the thesis is the complete design of a VTOL UAV with take-off weight less than 5 kg_f, a wing span of 2.25 m, a battery of 8500 mAh capacity and a maximum payload of 200 g_f; the expected flight time is about 85 minutes following a delivery mission profile made up of vertical take-off, cruise at constant altitude and vertical landing. Moreover, the developed LPV model of

the aircraft reproduces well the aircraft behavior with respect to the initial set of LTI models.

Sommario

Al giorno d'oggi i velivoli a pilotaggio remoto, generalmente chiamati droni, sono largamente studiati e diffusi. La prima cosa che viene associata alla parola drone è l'idea di un velivolo multi rotore, generalmente un quadricottero. Questa è solo una faccia della medaglia: oltre ai droni multi rotore, infatti, esistono anche droni ad ala fissa. Queste due categorie di velivoli a pilotaggio remoto possono essere sovrapposte, dando origine al cosiddetto drone VTOL: un velivolo capace di decollare e atterrare in verticale (in inglese vertical take-off and landing, da cui il nome VTOL) ma anche di un'elevata efficienza energetica nel volo orizzontale, fatto che lo rende adatto a missioni a media/lunga autonomia chilometrica e/o oraria. Dal momento che i multi rotor sono stati a lungo studiati e hanno mostrato la loro limitazione per quanto riguarda il tempo di volo e che, d'altra parte, i velivoli ad ala fissa non sono in grado di decollare ed atterrare in verticale, i droni VTOL uniscono gli aspetti positivi di entrambe le configurazioni e possono rappresentare il velivolo adatto a molte applicazioni, sia civili che militari: consegna di pacchi, rilievo del terreno, ricognizione e manutenzione per nominarne alcune possibili.

Scopo di questa tesi è lo sviluppo di un velivolo senza pilota VTOL: l'intero progetto viene sviluppato partendo da un gruppo iniziale di requisiti fino ai disegni tecnici pronti per la fase di costruzione. L'iter progettuale seguito è quello convenzionale: progetto concettuale, preliminare, di dettaglio e di produzione. Il velivolo è sviluppato in tutti i suoi aspetti: aerodinamica, struttura, componenti interni (elementi importanti poiché il velivolo è a pilotaggio remoto) e apparato propulsivo. Questo ultimo aspetto è di grande rilievo poiché una macchina VTOL effettua parte della missione volando come un velivolo ad ala rotante e parte come velivolo ad ala fissa. Un modello lineare a parametri variabili (LPV) è stato sviluppato utilizzando come base dei modelli lineari tempo invarianti (LTI); il parametro variabile scelto per il modello è la velocità di volo. Un modello LPV può essere utilizzato per il controllo e la simulazione del velivolo nell'intero intervallo di volo. La conclusione naturale di una tesi come questa sarebbe la realizzazione del progetto sviluppato; tuttavia, a causa dell'emergenza sanitaria dovuta al COVID-19, non è stato possibile costruire il velivolo nei laboratori del Politecnico di Milano.

Risultato finale della tesi è il progetto completo di un velivolo a pilotaggio remoto con ala fissa e capace di decollo e atterraggio verticali. Tale velivolo ha un peso al decollo di poco inferiore ai 5 kg_f, un'apertura alare di 2,25 m, imbarca

una batteria di capacità pari a 8500 mAh e può trasportare un carico pagante massimo di 200 g_f. Il tempo di volo stimato è pari a 85 minuti, ottenuto seguendo un profilo di missione di trasporto pacchi, composto da un decollo in verticale, una fase di crociera a quota costante e un atterraggio in verticale. Ulteriore risultato è il modello LPV sviluppato, modello che ben riproduce il comportamento del velivolo descritto dal set iniziale di modelli LTI.

Contents

Acknowledgments	I
Abstract	III
Sommario	V
List of figures	IX
List of tables	XIII
Introduction	1
1 Aircraft conceptual and preliminary design	5
1.1 Configuration choice	5
1.2 Preliminary sizing method	10
1.3 Preliminary sizing set up	12
1.4 Preliminary sizing values and result	16
1.4.1 Preliminary sizing general parameters	16
1.4.2 Preliminary sizing performance parameters	17
1.4.3 Preliminary sizing results	21
1.5 Sensitivity analysis	21
2 Aerodynamic design	27
2.1 Wing airfoil selection	28
2.2 Wing geometry	30
2.3 Tail configuration	33
2.4 U tail and V tail design	37
2.4.1 U tail design	37
2.4.2 V tail design	42
2.5 U tail and V tail comparison	43
2.6 Wing and tail design summary	48

3	Structural design	51
3.1	<i>v-n</i> diagram	51
3.2	Wing structural layout	56
3.3	Wing spar structural analysis	59
4	Propulsion, onboard systems and fuselage design	65
4.1	Electric motors selection	65
4.1.1	Vertical flight electric motors	65
4.1.2	Horizontal flight electric motors	70
4.2	Battery	71
4.3	Avionics	74
4.4	Fuselage design	75
5	Final design steps	87
5.1	Tail selection	87
5.2	Moving surfaces design	89
5.2.1	Aileron design	89
5.2.2	Elevator design	93
5.2.3	Rudder design	94
5.2.4	Servomotors selection	94
5.3	Production design	95
5.3.1	Wing production	95
5.3.2	Engine mountings	96
5.4	Trimmed polar and flight dynamics analysis	96
6	LPV model of the forward flight mode	103
6.1	LPV model theory	103
6.2	LPV model implementation	106
6.3	LPV model verification and validation	112
	Conclusions	117
A	Aerodynamic software considerations	127
B	Airfoil simulations	129
C	3D printing technologies	135

List of Figures

1	Example of drone delivery service, source [6].	1
1.1	Examples of VTOL UAV configurations among the competitors. . .	7
1.2	VTOL UAV configuration; this drawing shows which is the selected configuration. It is important to consider that tail configuration, fuselage layout and motor set up have not been decided yet: the represented ones are only to give a general idea of the configuration.	9
1.3	Generic sizing matrix plot for a propeller driven aircraft. The constraints used are on maximum speed v_{max} , take-off distance S_{TO} , rate of climb ROC , cruise altitude h_c and stall speed v_s . The acceptable region is crosshatched and the design point is the best in term of power loading. Source [22].	11
1.4	Empty weight W_E as function of take-off weight W_{TO} ; data from Table 1.1.	13
1.5	Delivery mission profile. Phase A-B is a vertical take-off and climb, B-C a cruise in FF mode, C-D is hovering phase using vertical axis engines, D-E is a cruise in FF mode and E-F is vertical descent and landing.	13
1.6	Sizing results for different stall speeds and payload weights.	20
1.7	Initial sizing matrix plot. The stall speed constraint is parameterized as function of the maximum lift coefficient $C_{L_{max}}$, the values of which are written near the corresponding constraint line.	22
1.8	Regression line for $W_E(W_{TO})$ comparison. The change based on the considered database can be seen clearly.	24
1.9	SMP sensitivity.	25
2.1	Nearest airfoils to the desired case. It can be clearly seen that one airfoil, the Selig 2046, is almost coincident with the required values.	31
2.2	Selig 2046 airfoil. It is presented dimensionless with respect to the chord, both in X and Y; airfoil coordinates are taken from [47].	31
2.3	Wing vertical location: (a) is a high wing, (b) is a mid-wing, (c) is a low wing and (d) a parasol wing. Source [22].	32

2.4	High wing pros with respect to a low wing for the VTOL UAV. The advantage from a propulsive point of view is presented on top: FF engines have a greater clearance from ground so they do not touch ground before take-off and after landing. On the lower part it can be seen that it is easier to attach the wing to the fuselage if the wing is high.	32
2.5	Tail configuration options.	34
2.6	V tail moving surfaces as elevator and rudder.	35
2.7	Aircraft aft-part wet surface in the case of a U tail. S_{wet}^{aft} depends only on the tail arm l	38
2.8	Simplified moment equilibrium scheme for tail incidence computation.	41
2.9	U tail model in XFLR5.	44
2.10	V tail model in XFLR5.	44
2.11	One engine inoperative scheme for rudder design; source [22].	45
2.12	Moving surfaces effectiveness parameter as function of the moving surface on main surface chord ratio. Source [22].	46
2.13	Lift coefficient and induced drag distributions along the span of the main wing; results from XFLR5 simulations.	49
3.1	Typical diagram for maneuvering and gust loads of a small UAV; source [16].	52
3.2	Maneuvering diagram for the VTOL UAV.	55
3.3	v - n diagram for the VTOL UAV; it is the superposition of the maneuvering diagram (solid blue lines) and of the gust diagram (red dash-dot lines).	56
3.4	Mixed structural layout inspired by the UAVs of Southampton University [16]. The colors of the components are deliberately not real to better recognize the different elements.	57
3.5	Composite structural layout with semi-monocoque scheme. The same consideration about colors made for Figure 3.4 applies here.	58
3.6	Possible spar sections for the semi-monocoque structural layout.	59
3.7	Semi-wing structural layout overview.	60
3.8	Beam reference frame for stress computation.	61
3.9	Forces acting on the k -th element of the beam, highlighted in red.	63
3.10	Deflection of the i -th element of the beam.	63
3.11	Results of beam analysis with loads from XFLR5.	64
4.1	Considered options for the number of VF engines.	66
4.2	Six VF engines configuration, different positions of the central motor.	67
4.3	Selected engine: KDE Direct KDE2315XF - 2050, source [56].	69
4.4	Vertical motors position along the booms.	69
4.5	Considered options for the number of FF engines.	70
4.6	FF engine position on the forward booms.	70

4.7	Selected engine: KDE Direct KDE2304XF - 2350, source [56]. . .	72
4.8	Avionics components - part 1.	76
4.9	Avionics components - part 2.	77
4.10	Fuselage layout: three positions in the central part are highlighted; the lateral parts are dedicated to the motor booms.	78
4.11	CAD view of the base designed for electronics.	78
4.12	Disposition of the components inside the fuselage; the arrangement for the motor booms can also be seen. The cut A-A, shown on the left, presents the disposition of the wing spar on top of the motor booms.	79
4.13	Carbon fiber tubes locking mechanism.	80
4.14	The fuselage is divided into four parts: a base, a central coverage and two lateral coverages.	81
4.15	Two systems connect the central coverage to the fuselage base: a mechanical pin in the front part and a set of magnets in the rear part.	82
4.16	Housing for the motor booms.	83
4.17	Aircraft support elements.	83
4.18	External views of the fuselage CAD.	84
4.19	External views of the fuselage CAD.	85
5.1	CAD of the UAV in U tail configuration.	88
5.2	CAD of the UAV in V tail configuration.	89
5.3	Incremental change in lift and drag in generating a rolling motion with aileron deflection. Source [22].	92
5.4	Aircraft roll rate response to aileron deflection; source [22].	92
5.5	Corona 939 Metal Gear servomotor for moving surfaces.	95
5.6	VF engine supports.	97
5.7	FF engine supports.	98
5.8	Trimmed drag polar in cruise conditions at W_{TO}	99
5.9	Elevator deflection as function of the speed range.	100
5.10	Longitudinal flight modes in the complex plane.	101
5.11	Lateral flight modes in the complex plane.	101
6.1	Explicit model stitching architecture.	105
6.2	Implicit model stitching architecture.	105
6.3	Forces in symmetric flight, source [70].	109
6.4	Horizontal flight engines thrust as function of the throttle percentage (the values presented are related to the overall thrust output of both FF motors); data from the manufacturer ([56]).	111
6.5	Force scheme for the propulsion decomposition in stability axes. . .	111

6.6	Longitudinal dynamics frequency response: from elevator deflection to pitch rate. The frequency response is performed in cruise conditions.	113
6.7	Frequency domain responses in cruise speed conditions.	114
6.8	Longitudinal dynamics quantities in verification and validation points.	115
6.9	Lateral dynamics quantities in verification and validation points. .	116
6.10	Technical drawings of the VTOL UAV, scale 1:10. The measurements are given in mm.	119
B.1	Airfoil sections analyzed to select the best one; part 1.	130
B.2	Airfoil sections analyzed to select the best one; part 2.	131
B.3	Airfoil sections analyzed to select the best one; part 3.	132
B.4	Airfoil sections analyzed to select the best one; part 4.	133
B.5	Various airfoils for low Reynolds.	134
C.1	FDM printing technology scheme, source [73].	136
C.2	SLS manufacturing (left column) and depowdering (right column), source [16].	137

List of Tables

1.1	Competitors database. Data are taken from manufacturers websites ([6], [27], [10], [28], [29], [26], [30], [31],[32], [33], [34], [35], [36], [37], [9], [38], [39], [40] and [41]); symbol - states that data is not available.	8
1.2	Preliminary sizing parameters.	17
1.3	Competitors speed range. Data are taken from manufacturers websites ([6], [27], [10], [28], [29], [26], [30], [31],[32], [33], [34], [35], [36], [37], [9], [38], [39], [40] and [41]); symbol - states that data is not available.	19
1.4	Summary of preliminary sizing performance parameters.	21
1.5	Sensitivity analysis iterations. The first block shows the sizing result obtained in Section 1.4; the second one the iterations changing the statistical database for $W_E - W_{TO}$ regression.	24
1.6	Final values of the preliminary design.	26
2.1	Tail options pros and cons for an immediate comparison.	36
2.2	Horizontal and vertical tail volumes for aircraft flying in similar conditions.	37
2.3	U tail and V tail results of the XFLR5 simulations.	48
2.4	Wing parameters summary.	49
2.5	U tail parameters summary. The data of the vertical tail are related only to one part, so the overall surface is twice the value presented.	50
2.6	V tail parameters summary. The data are related only to one part, so the overall surface is twice the value presented.	50
3.1	Reference values for maximum and minimum load factors of the $v-n$ diagram.	52
3.2	Reference values for gust loads of the $v-n$ diagram. Reference [19] allows in some cases to consider only half the standard gust velocity, <i>i.e.</i> , $U_1 = 7.6$ m/s and $U_2 = 3.8$ m/s.	53
4.1	Selected VF engine performance as function of the throttle percentage. Data from the manufacturer website [56].	69

4.2	Selected FF engine performance as function of the throttle percentage. Data from the manufacturer website [56].	72
4.3	Weight and dimensions of the avionics components for the fuselage sizing.	75
5.1	U tail parameters summary. The data of the vertical tail are related only to one part, so the overall surface is twice the value presented.	90
5.2	Eigenvalues of the flight modes in forward flight configuration. . .	100
5.3	Flight modes comparison with respect to MIL F 8785 C regulation. $\tau_R = 0.047$ s for the roll mode and $T_2 = 3.8$ s for the spiral mode.	102
6.1	Summary of design parameters. The position of CG is computed from the nose of the aircraft fuselage.	118

Introduction

On April 30, 2020 the BBC published an article titled *“Drone-to-door medicines trial takes flight in Ireland”* ([1]) while on April 9 the American technology news website The Verge wrote *“Alphabet’s nascent drone delivery service is booming”* ([2], Figure 1). The interest in unmanned aerial vehicles (UAVs) for delivery purposes is increasing around the world. This interest is related not only to the actual COVID-19 pandemic but also to the great opportunities this type of aircraft offers: faster delivery time, lower maintenance costs with respect to the conventional delivery systems and environmental friendliness ([3]). Several UAV configurations have been studied and designed for drone delivery purposes but the most promising one is the fixed-wing vertical take-off and landing (VTOL) one: it combines the pros of conventional multi-rotor UAVs (no need of a runway, hovering capability) to the higher speed and range of fixed-wing aircraft. As example of the interest in the field, the German start-up Wingcopter has recently received an investment of several millions dollar to develop further its VTOL UAV and signed a partnership with UPS delivery service ([4] and [5]).



Figure 1: Example of drone delivery service, source [6].

Thesis objective

The objective of this thesis is to design and prototype a VTOL UAV inside the laboratories of Politecnico di Milano. At least, it was up to the COVID-19 pandemic: the lockdown has made impossible to finish the thesis as it was intended, so the prototyping phase has been substituted by a dynamic modeling of the UAV. Since the thesis started months before the current health situation, all the design has been performed with the final prototyping in mind, so practical aspects have been held in higher regard than typically done in on-paper-only academic projects. The VTOL will be built when possible after the end of the thesis.

At the base of every project, both aeronautical and non, there are requirements to be satisfied. In the case of this VTOL UAV they are few:

- the main purpose of this aircraft is to exist, so that its design process can be studied and improved paving the way for future aircraft of this kind. Moreover, designing and building it will bring experience in the field of VTOL UAVs and of small fixed-wing unmanned aircraft. It can be considered with good reason a research-focused machine.
- No specific mission profile or mission requirement has been given from the customer (in this case the thesis advisor) so the UAV will be designed to fulfill a delivery mission profile made up of vertical take-off, horizontal cruise with intermediate hovering phase and final vertical descent.
- Being a research-focused aircraft it has to be modular, so that it can be exploited for the largest number possible of research fields. In particular, the wings are required to be removable, so the UAV can accommodate different wings allowing to test them in real flight. Moreover, to allow an easy transportation the whole aircraft has to be disassembled.
- The VTOL UAV has to be an electric aircraft, so the propulsion has to be based on batteries and electric motors.

This thesis represents the first prototyping experience of a fixed-wing aircraft at Politecnico di Milano long since: the Department of Aerospace Science and Technology (DAER) has not produced, in the last years, aircraft by itself. This thesis, then, is the occasion to start building aircraft again. It has been decided to design the aircraft with simplicity in mind, avoiding, at least for this first VTOL prototyping experience, unnecessary complications.

State of the art

There are several already designed VTOL UAVs around the world, mainly for delivery purposes but also for reconnaissance and aerial mapping. Some models

are directly designed and manufactured by the delivery service providers, for example Alphabet's X Wing ([6]), which has been the first to gain FAA approval for a commercial delivery service ([7]) and Amazon's Prime Air ([8]); other are from aircraft manufactures, like Wingcopter's VTOL ([9]) or Wingtra's Wingtra One ([10]).

Also in the academic world there is interest in this topic: reference [11] presents the preliminary design procedure for an electric VTOL UAV while references [12], [13] and [14] present the design and experimental results of different VTOL UAVs in several configurations, with attention to the control and dynamic modeling aspects. It is important to mention, in the academic field, the experience of Southampton University (UK), [15]: currently it has developed and operated five fixed-wing UAVs with take-off weight ranging from 3 kg_f to 35 kg_f. These UAVs are not VTOL aircraft, however Southampton University experience is of great interest and inspiration due to the high level work done ([16]).

Coming to the state of the art at Politecnico di Milano, at the moment the DAER facilities, in particular the Aerospace Systems and Control Laboratory (ASCL), have designed and manufactured UAVs only in the form of multi-rotors. The great experience in hardware integration and flight control laws development of ASCL people is matched by a in-depth aircraft design course in the Flight Mechanics and Systems Master of Science degree. These two aspects can be overlapped with the aim of designing a VTOL UAV.

The VTOL UAV is developed within the regulatory framework of the European Union, in particular with reference to [17] and [18]. These two regulations, however, set few requirements to the designer (for example for what concerns the structural design). Given that, it has been decided to look for other UAVs regulations with which have a comparison: the selected regulations are the one developed by NATO for military UAVs (NATO Standard AEP-83, reference [19]), useful in particular for the structural design, and the US Department of Defense MIL F 8785 C ([20]) for the flight qualities. This last regulation is clearly out of context for a light and small UAV, however it is the only regulation available for this task.

Structure of the thesis

The thesis is organized as follows:

- in Chapter 1 the conceptual and preliminary design phases are carried out. In the former the initial design requirements are transformed into a general idea of the UAV, *i.e.*, the aircraft general configuration and its specifications (number of wings, engine number and types and so on); in the latter the first figures about the aircraft are computed: take-off weight, wing surface and required power.

- In Chapter 2 the detail design starts. This chapter is devoted to the aerodynamic design of the aircraft: the wing, which is the main responsible of the lift generation, and the tail, designed to keep the aircraft stable. Two tail configurations are selected and compared to identify the best for the VTOL UAV.
- Chapter 3 presents the second part of the detail design: the structure. In this chapter the maximum loading conditions to which the aircraft has to withstand are identified, then the structural layout is selected and it is analyzed with respect to the loads initially identified.
- Chapter 4 completes the detailed design being devoted to the remaining aspects of the design: the propulsion, the onboard systems and the fuselage. These three aspects are closely related and important for the success of the design.
- Chapter 5 presents miscellaneous aspects all related to the conclusion of the aircraft design: the selection of the tail started in Chapter 2 , the design of the moving surfaces, the production design of the wing and of other components, the analysis of the flight dynamics of the designed aircraft.
- Chapter 6 presents the dynamical modeling of the VTOL UAV performed in replacement of the prototyping and assembly phases. The model developed is a linear parameter varying (LPV) model, which can be used to develop the flight controllers of the aircraft and to simulate its motion.

Chapter 1

Aircraft conceptual and preliminary design

At the beginning of a new aircraft project only few specifications and requirements are given. The first step, called conceptual design, consists in transforming these few information into a configuration that can meet the initial requirements: it is a high level operation which defines a general idea of the aircraft, *i.e.*, wings number and position, tail configuration, engines position and so on. In this step several configurations (but also elements of a configuration) can be selected and developed with more details for a final comparison and choice (for example two tail options are selected and investigated further to identify the best one from a control point of view). The second step in aircraft design is called preliminary design; in this phase a set of fundamental parameters are computed: wing surface S , take-off weight W_{TO} and required power P_b . These values are the cornerstone of the whole design, from aircraft size to performance and costs.

This chapter presents these two steps for the sizing of a VTOL UAV: initially the configuration is selected, then fundamental parameters are computed and, to check the robustness of the obtained solution, a sensitivity analysis is performed.

1.1 Configuration choice

Configuration selection is the first thing to be done in designing a new aircraft. At this stage all the possible options are checked so that the wider range of possibilities is considered. There may be more than one configuration that suits the initial requirements. Aircraft design literature ([21], [22] and [23]) and research papers ([12], [14], [24] and [25]) along with configurations adopted by competitors currently on the market are a good starting point for a configuration survey. It is important to consider the state of art of materials and propulsion since lots of aircraft configuration aspects depend on them. After an initial survey, three options for the VTOL configuration are selected and presented in detail:

- **dual system configuration:** this configuration features two separate propulsive systems, one for vertical flight (VF) and one for forward flight (FF). Generally this configuration resembles a conventional fixed wing aircraft with VF propulsive system housed inside booms under the wing. This configuration allows to analyze independently VF and FF phases since propulsion is separate. Another pro is the absence of conversion systems to transform VF propulsion into FF propulsion, avoiding extra complexity and weight. On the other hand, having two sets of motors means more weight and drag during all the mission also when a set is not working. An example of this configuration can be seen in Figure 1.1a;
- **tail sitter configuration:** this configuration has one propulsion system used for both VF and FF. For take-off and landing the UAV stands vertically in the air; once the transition altitude is reached, the aircraft performs a turn and arises horizontal so that the propulsive unit can be used for FF. The pro of this configuration is the absence of redundant parts since there is a complete conversion of the aircraft from VF to FF. The cons are that horizontal flight with payload is more complex (during the transformation between VF and FF the payload changes orientation) and during take-off and landing the large wing surface is fully exposed to gusts and turbulence, *i.e.*, there can be a significant disturbance problem when operating in VF mode. Figure 1.1b shows a tail sitter VTOL UAV;
- **tilt rotor configuration:** this configuration is very similar to the dual system one; the main difference is that in this case VF and FF propulsive system are the same and there is a transition from VF to FF rotating the engines themselves. This configuration has the pro of avoiding double propulsion systems; however, a reduction in weight with respect to the dual system configuration is not granted since the conversion mechanism that rotate the engines to change the thrust direction adds weight. Moreover, the rotation system adds complexity to the design and to the whole aircraft operative life. Increased complexity in the design phase is due to the fact that transition has to be considered in modeling and sizing the aircraft. Figure 1.1c presents a tilt rotor UAV.

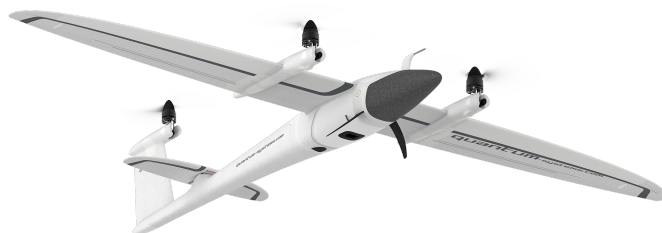
It is useful, in order to choose the best configuration, to consider the trend adopted by competitors. Figure 1.1 shows some of them while Table 1.1 shows a complete list with all the competitors and some of their main specifications. From Table 1.1 it can be seen that the most used configuration is the dual system one. This can be explained considering that the dual system configuration allows a simpler design process and can be the first step in VTOL design for companies that produces multi-rotors UAVs and fixed wing UAVs given that it is the overlap of these two drone categories.



(a) Dual system configuration: Google X Wing. Source [6].



(b) Tail sitter configuration: Wingtra One. Source [10].



(c) Tilt rotor configuration: Quantum Systems Trinity F90+. Source [26].

Figure 1.1: Examples of VTOL UAV configurations among the competitors.

Model	Manufacturer	Configuration	Year	Material	W_{TO} [kgf]	W_E [kgf]	W_{μ} [kgf]	b [m]	\mathcal{E} [mm]	\mathcal{R} [km]
Wing	Google X	Dual system	2017	-	4.8	-	1.5	1.0	-	20
DeltaQuad Pro #Cargo	DeltaQuad	Dual system	2017	EPO	6.2	3.3	1.2	2.3	110	100
Wingtra One	Wingtra	Tail siter	2017	Composite	4.5	3.1	0.8	1.2	55	-
Kapetair VTOL UAV	Kapetair	Tilt rotor	2017	Composite	6.5	-	1.0	3.3	120	120
Tigerwing	Sunbirds	Dual system	-	EPO	2.8	-	-	1.8	90	64
Trinity F90+	Quantum Systems	Tilt rotor	2019	-	5.0	-	0.7	2.4	90	7
Tron F90+	Quantum Systems	Tilt rotor	2019	Composite	13.5	-	2.0	3.5	90	7
Vector	Quantum Systems	Tilt rotor	-	-	6.0	-	0.5	-	120	-
UAV Birdie VTOL	Fly Tech UAV	Dual system	-	Composite	3.9	-	-	1.8	-	30
Skyproowler 2	Krossblade	Dual system	2019	Composite	2.3	-	-	1.1	55	90
Fusion	Heliceo	Dual system	-	Composite	8.5	-	1.6	-	60	-
ZT-3V	Zerotech	Dual system	-	Composite	8.1	-	1.1	2.4	60	-
Avy	Avy	Dual system	2019	Composite	9.5	5.5	2.0	2.7	90	100
Savant	Drone America	Dual system	2016	Composite	18.1	-	3.1	3.6	90	100
EOS C UAS	Thread Systems	Dual system	-	-	13.0	-	-	4.8	180	-
Kestrel	Autel Robotics	Tilt rotor	-	-	14.0	-	2.5	3.5	120	-
Wingcopter 178	Wingcopter	Tilt rotor	2016	Composite	9.6	5.0	2.0	1.8	120	45
Sama UAV VTOL	Tareq UAV	Dual system	-	Composite	6.5	-	0.5	2.1	60	70
SP9 VTOL	TTA America	Dual system	-	-	-	3.2	2.0	2.9	210	-
Hawk-Eagle 01	Honyi	Dual system	-	Composite	10.0	4.0	2.0	2.4	120	80
Eagle Hero VTOL	Sparkle Tech	Dual system	2016	Composite	14.0	8.2	1.5	3.5	120	-
Ranger VTOL	Sparkle Tech	Dual system	2016	Composite	14.0	6.0	1.0	3.0	90	-
Dragon VTOL	Sparkle Tech	Dual system	2016	Composite	4.0	7.0	1.5	3.0	120	-
VTOL UAV [11]	-	Dual system	2017	-	3.7	2.1	0.3	1.7	-	-
Wingcopter 178 HL	Wingcopter	Tilt rotor	2016	Composite	16.0	6.0	6.0	1.8	120	45
Penguin BE	UAV Factory Ltd.	Conventional	2009	Composite	21.5	10.4	6.6	3.3	110	-

Table 1.1: Competitors database. Data are taken from manufacturers websites ([6], [27], [10], [28], [29], [26], [30], [31], [32], [33], [34], [35], [36], [37], [9], [38], [39], [40] and [41]); symbol - states that data is not available.

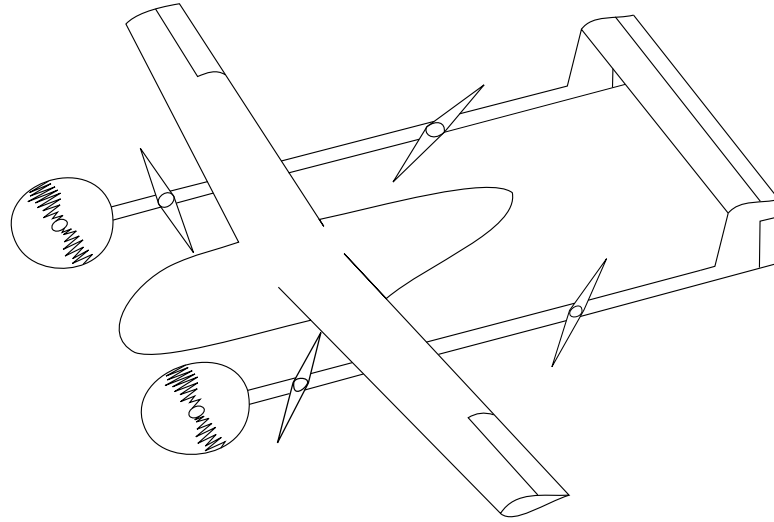


Figure 1.2: VTOL UAV configuration; this drawing shows which is the selected configuration. It is important to consider that tail configuration, fuselage layout and motor set up have not been decided yet: the represented ones are only to give a general idea of the configuration.

The design principle adopted in this thesis, as stated in the introduction, is simplicity since this VTOL UAV is the first aircraft prototyping experience at Politecnico di Milano long since. The idea is to avoid unnecessary complexity, if possible. The tail sitter is excluded even if it is probably the simplest configuration in the set. It is discarded due to the possible gust problems in VF operations considering also that the VTOL UAV is intended for outdoor operations. Between the tilt rotor and the dual system the latter is simpler: the dual system configuration allows to study and design vertical and forward flight phases separately at the only price of a double propulsive system. Considering the nature of the project this is a key advantage, so the dual system configuration is selected as configuration of the VTOL UAV. Following the design principle adopted, it has been decided that the aircraft has only one wing; the tail is attached to the wing with the same booms that house also the engines for VF to make a smart use of these structural components. Figure 1.2 shows a picture of the general idea of the UAV. An important remark: up to now only the general aspects of the configuration have been fixed (number of wings, tail location, propulsive system nature); in the following tail configuration, number and position of VF and FF engines have to be decided. These aspects will be addressed while designing wing, tail and propulsion.

1.2 Preliminary sizing method

Once the conceptual design has been accomplished and a configuration has been selected, it is time to start the preliminary sizing. There are three objectives in this phase: take-off weight, wing surface and required power. In the case of a VTOL UAV the required power can be divided into power for FF, P_b^{FF} , and for VF, P_b^{VF} . This section includes the sizing method adopted. References [42] and [43] present the classical sizing approach for propeller driven aircraft, summarized in the following. Note that this is the general procedure and needs to be adapted to electric unmanned aircraft.

The first step consists in computing the take-off weight: finding W_{TO} is fundamental since mass is paramount in an aeronautical project. Currently the aircraft does not exist so some statistical data about competitors is used in this step. Take-off weight is found solving the weight breakdown

$$W_{TO} = W_E + W_{fuel} + W_{pl} + W_{crew} \quad (1.1)$$

once empty weight W_E and fuel weight W_{fuel} have been written as function of W_{TO} ; payload weight W_{pl} and crew weight W_{crew} are known.

$W_E(W_{TO})$ is found with a statistical regression of similar aircraft empty weight as function of take-off weight. An example can be seen in Figure 1.4, which represents the statistical regression of the UAVs in Table 1.1. $W_{fuel}(W_{TO})$ is written using the fuel fraction method based on the mission profile, as shown in equation (1.2) for a generic mission profile made of take-off, climb, cruise, descent and landing:

$$1 - \frac{W_{fuel}}{W_{TO}} = \frac{W_{final}}{W_{LND}} \frac{W_{LND}}{W_{descent}} \frac{W_{descent}}{W_{cruise}} \frac{W_{cruise}}{W_{climb}} \frac{W_{climb}}{W_{TO}}. \quad (1.2)$$

W_{climb} is the weight at the beginning of the climb (corresponding to the one at the end of the take-off), W_{cruise} is the weight at the beginning of the cruise or at the end of the climb, $W_{descent}$ the one at the beginning of the descent phase or at the end of the cruise, W_{LND} the weight at the beginning of the landing and W_{final} the final weight equal to $W_{TO} - W_{fuel}$. Each fraction represents the change in weight due to the fuel burnt in each flight phase.

Equation (1.1) can be rearranged as

$$W_{TO} = \frac{W_{crew} + W_{pl}}{1 - \frac{W_E}{W_{TO}} - \frac{W_{fuel}}{W_{TO}}}, \quad (1.3)$$

which can be solved once equation (1.2) and the statistical regression $W_E(W_{TO})$ have been computed. The result is the take-off weight W_{TO} .

The second step of the preliminary sizing classical procedure is choosing the design point. The design point is characterized by a value of wing loading $\frac{W_{TO}}{S}$ and a value of power loading $\frac{W_{TO}}{P_b}$. The values of wing and power loading are found

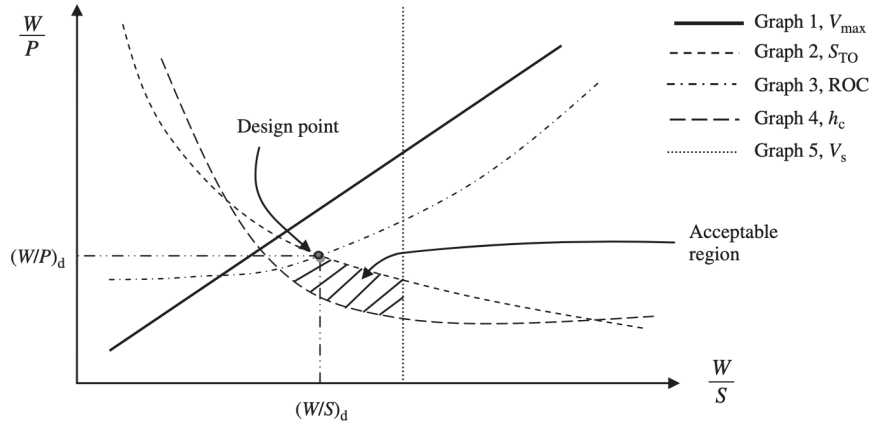


Figure 1.3: Generic sizing matrix plot for a propeller driven aircraft. The constraints used are on maximum speed v_{max} , take-off distance S_{TO} , rate of climb ROC , cruise altitude h_c and stall speed v_s . The acceptable region is crosshatched and the design point is the best in term of power loading. Source [22].

using the sizing matrix plot (SMP), a plane on which all the mission constraints are imposed in graphical way. An example of SMP for a propeller driven aircraft can be seen in Figure 1.3. It is mandatory, to build the SMP, to identify all the constraints (as an example stall speed, maximum turn rate, maximum speed, landing distance) relevant for the design case at hand. For this purpose regulation requirements and customer's requirements are considered. Once the SMP has been drawn, the best place is selected as design point: generally, the best point in the SMP is the one with the highest power loading and wing loading but there can be multiple optimal points; the choice is based on general considerations about the project. This is due to the fact that, for equivalent W_{TO} , an higher power loading brings to a lower required power and an higher wing loading to a smaller wing surface, so smaller aircraft. Once wing loading $\frac{W_{TO}}{S}$ and power loading $\frac{W_{TO}}{P_b}$ are known, S and P_b are computed since W_{TO} is already available.

This is the general procedure for propeller driven aircraft (applicable with small changes to jet aircraft). It is necessary to adapt it to the case of an electric aircraft without pilot onboard. The first thing is to set W_{crew} to zero and change W_{fuel} to W_{batt} , with W_{batt} battery weight. However, the fuel fraction method (equation (1.2)) cannot be used since there is no weight loss due to battery energy consumption. In other words, the take-off weight does not change during the missions because the battery does not lose mass when has released all its energy. Since there is a significant research regarding electric aircraft, some solutions to this design problem have been found. The one adopted in this design procedure is proposed in [44]: weight estimate and SMP are connected and general flight mechanics equations are used to compute energy and power consumptions in each flight phase of the mission profile. These energy and power consumptions are used

to compute the battery weight. Power and wing loadings are used inside the flight mechanics equations to compute it as function of W_{TO} .

1.3 Preliminary sizing set up

This section presents the preliminary sizing set up based on the sizing method explained in Section 1.2. In order of presentation inside this section, the statistical relation between empty weight and take-off weight is obtained, the battery weight is computed and the SMP is developed.

The weight breakdown for this specific electric VTOL UAV sizing is

$$W_{TO} = W_E + W_{batt} + W_{pl}. \quad (1.4)$$

As said in [44], the right hand side members have to be written as functions of W_{TO} , so the only unknown in equation (1.4) is W_{TO} itself.

As already mentioned, the empty weight W_E , which includes structural weight, systems and engines weights, is computed using a statistical regression of existing UAVs. The regression line in Figure 1.4 is based on the competitors database presented in Table 1.1: only the UAVs for which information about both W_{TO} and W_E is available are considered. As suggested both in [42] and [43], a linear regression approximates well the data.

W_{batt} is based on the reference mission profile shown in Figure 1.5. Now the power consumption of each mission profile leg is computed using simple flight mechanics equations.

UAV take-off and climb phase is the first segment; in this leg the VTOL UAV works as a multi-rotor drone, so the required power in climb, P_b^{cl} , is computed using momentum theory in climb as in [45] giving

$$P_b^{cl} = \frac{\mathcal{T}_{cl} v_i}{FM}, \quad (1.5)$$

where \mathcal{T}_{cl} is the thrust during climb, v_i the induced velocity on the rotors disk and FM the rotor figure of merit.

The induced velocity is

$$v_i = \frac{ROC}{2} + \sqrt{\left(\frac{ROC}{2}\right)^2 + \frac{\mathcal{T}_{cl}}{2\rho_0 A_{prop}}} \quad (1.6)$$

while the required thrust in climb is

$$\mathcal{T}_{cl} = W_{TO} + \frac{1}{2}\rho_0 ROC^2 S_p C_{D_{cl}}. \quad (1.7)$$

ROC is the rate of climb, ρ_0 the density at ground level, A_{prop} the overall propeller area, S_p the horizontal projected area of the UAV and $C_{D_{cl}}$ the drag coefficient in

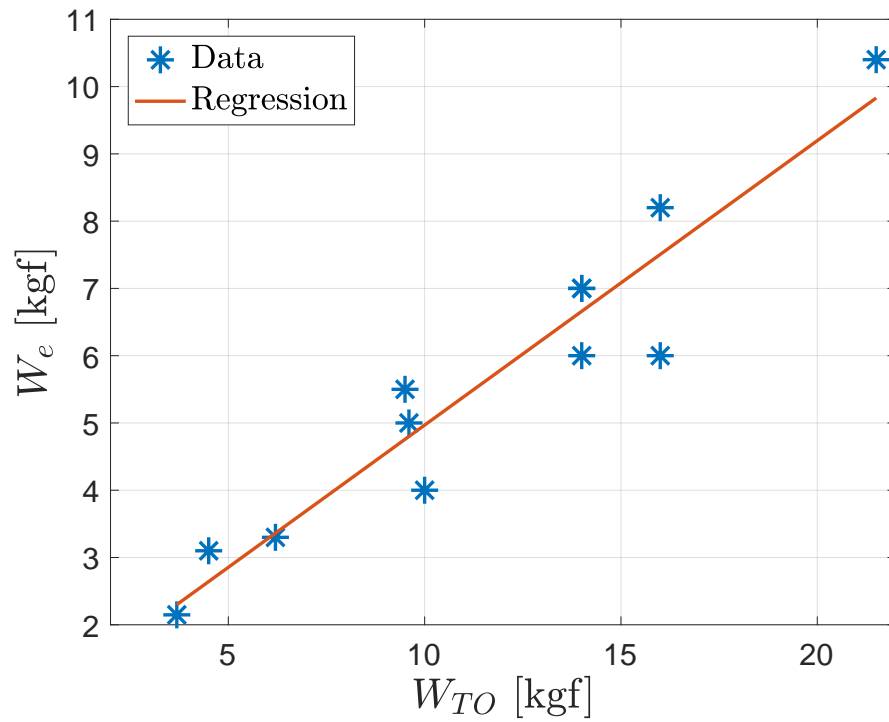


Figure 1.4: Empty weight W_E as function of take-off weight W_{TO} ; data from Table 1.1.

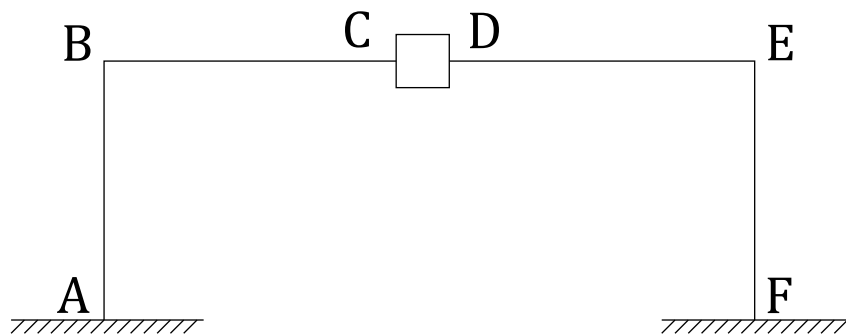


Figure 1.5: Delivery mission profile. Phase A-B is a vertical take-off and climb, B-C a cruise in FF mode, C-D is hovering phase using vertical axis engines, D-E is a cruise in FF mode and E-F is vertical descent and landing.

climb. The power required for climb is assumed equal to the power required for descent, so equation (1.5) can be used for both phases.

Now the cruise phases are analyzed (with reference to Figure 1.5, both the segment B-C and the segment D-E). Power in cruise is computed starting from the horizontal level flight power equilibrium

$$P_b^{cr} = Dv_{cr} \quad (1.8)$$

with D drag and v_{cr} cruise speed. The substitution of the conventional drag definition

$$D = \frac{1}{2}\rho v^2 SC_D \quad (1.9)$$

in equation (1.8) leads to

$$P_b^{cr} = \frac{1}{2}\rho_{cr}v_{cr}^3 C_{D_{cr}} \frac{W_{TO}}{\left(\frac{W_{TO}}{S}\right)_{FF}}, \quad (1.10)$$

where $C_{D_{cr}}$ is the drag coefficient in cruise phase, ρ_{cr} is the density at cruise altitude and $\left(\frac{W_{TO}}{S}\right)_{FF}$ the wing loading for FF obtained from the SMP.

The last mission profile leg to be analyzed is the hovering phase, in Figure 1.5 the part C-D. The VTOL UAV works as a multi-rotor in hovering as in climb and descent phases, so the required power is computed with the momentum theory:

$$P_b^{ho} = \frac{\mathcal{T}_{ho}^{3/2}}{\sqrt{2}\rho_0 A_{prop}}, \quad (1.11)$$

with \mathcal{T}_{ho} thrust in hovering condition defined as

$$\mathcal{T}_{ho} = W_{TO} \quad (1.12)$$

due to vertical equilibrium.

As in [44], the battery is sized considering both energy and power. The energy necessary to complete the mission profile is obtained multiplying the required power of each leg by its time duration. Then, the obtained energy is divided by the battery specific energy \bar{e} and the power is divided by battery specific power p : in this way two battery weights are obtained. The maximum between these two is selected and, by definition, satisfies both energy and power requirements. The relation between W_{batt} and W_{TO} is

$$W_{batt} = \frac{g}{\eta} \max \left\{ \frac{P_b^{ho} \times t_{ho} + P_b^{cr} \times t_{cr} + P_b^{cl} \times 2t_{cl}}{\bar{e}}, \frac{\max \left\{ P_b^{ho}, P_b^{cr}, P_b^{cl}, W_{TO} / \left(\frac{W_{TO}}{P_b} \right)_{FF} \right\}}{p} \right\}. \quad (1.13)$$

The hovering time is indicated with t_{ho} , t_{cr} is the cruise duration and t_{cl} the climb one (it is assumed that climb and descent last the same amount of time), g the gravity field intensity, η the propulsive efficiency and $\left(\frac{W_{TO}}{P_b}\right)_{FF}$ power loading for FF. Note that climb time is considered twice to account also for descent time.

It is worth mentioning again that required power and wing surface are written using the power and wing loading from SMP. In this project LiPo batteries have been considered since they are better than LiOn in terms of energy density; other battery technologies are currently available (NiCd and LiS for example) but they have worse performance or are not fully developed yet ([21] and [46]).

Last element in the take-off weight breakdown is the payload weight. W_{pl} is fixed by the designer: since no specific requirement is set for this project, a range of payload weights is adopted to produce a number of design options. This aspect is explained in detail in Section 1.4 while selecting the parameters to be used in the sizing.

Once the empty weight regression and the battery weight relation have been developed, the SMP is considered. In the case of propeller-driven aircraft the SMP includes all the constraints in the power loading - wing loading space. All the applicable constraints for the SMP are written in the following. It is very important to note that the SMP is used to size the FF part of the UAV, namely P_b^{FF} and S . The preliminary sizing of the VF part is related to the required power for climb/descent and hovering P_b^{VF} . To account for control power while in hovering and climb, $P_b^{VF} = 1.3 P_b^{cl}$ with P_b^{cl} defined in equation (1.5). This aspect will be better considered and explained when selecting the VF engines in Chapter 2.

The first step in making the SMP is to select all the constraints for the case at hand, then to write them in terms of power loading and wing loading. Standard mathematical formulations can be found both in [42] and [43]. Performance and regulation requirements have been considered in making the following list of constraints:

- **stall speed**; this requirement applies to the forward flight phase; it is parameterized by the maximum lift coefficient and it is a constraint on the wing loading. The starting point is the vertical equilibrium in horizontal level flight,

$$\frac{1}{2}\rho_0 v_s^2 S C_{L_{max}} = W_{TO}, \quad (1.14)$$

where $C_{L_{max}}$ is the maximum lift coefficient and v_s the stall speed. With few manipulations the mathematical formulation of the stall speed constraint is obtained as

$$\left(\frac{W_{TO}}{S}\right)_{FF} = \frac{1}{2}\rho_0 v_s^2 C_{L_{max}}. \quad (1.15)$$

- **Maximum horizontal speed;** this is a performance requirement. It is important to pay attention to the fact that design maximum speed v_{max} is different from design cruise speed. This choice has been made to allow the UAV to reach speeds beyond v_{cr} . To write this constraint a power equilibrium in cruise at maximum speed is written:

$$P_b \eta_{FF} = \frac{1}{2} \rho_{cr} v_{max}^3 S C_{D_{cr}}, \quad (1.16)$$

where η_{FF} is the propulsive efficiency in FF mode.

$$\left(\frac{W_{TO}}{P_b} \right)_{FF} = \frac{2}{\rho_{cr}} \frac{\eta_{FF}}{C_{D_{cr}}} \frac{1}{v_{max}^3} \left(\frac{W_{TO}}{S} \right)_{FF} \quad (1.17)$$

is easily obtained from equation (1.16) in the form power loading function of wing loading.

1.4 Preliminary sizing values and result

The last step before choosing the design point on the SMP is the selection of aerodynamics, propulsive and performance values to be used. They can be divided into two groups: general parameters (such as efficiencies and drag coefficients) and performance parameters (such as speeds and mission profile legs duration).

1.4.1 Preliminary sizing general parameters

Considering general parameters, Table 1.2 shows the values adopted and their motivation/source. Most of them are typical values found in literature since in the early stages of the design process, such as the preliminary sizing, the specific values for the designed aircraft are unknown. Among all the values in Table 1.2, a further note is made about the aerodynamic coefficients: the zero lift drag coefficient C_{D_0} , the parabolic drag polar coefficient k and the maximum lift coefficient $C_{L_{max}}$. It is common practice in the early stages of design ([21], [43] and [42]) to assume a parabolic drag polar in the form

$$C_D = C_{D_0} + k C_L^2. \quad (1.18)$$

This assumption allows to reduce all the aerodynamic information to two coefficients: C_{D_0} and k . Reference [21] proposes a method to estimate these two coefficients starting from geometrical information of similar aircraft: considering the database in Table 1.1, data about the aspect ratio AR and wetted surface S_{wet} are collected. The computed value of C_{D_0} has been increased by 20% to make the estimate more conservative. The resulting values are $C_{D_0} = 0.023$ and $k = 0.046$. Now the maximum lift coefficient $C_{L_{max}}$ is considered: since simplicity

Parameter	Value	Motivation
e	0.685	Typical value from [21]
k	0.046	Procedure from [21]
C_{D_0}	0.023	Procedure from [21]
$C_{D_{cr}}$	$1.1 \times C_{D_0}$	Typical value from [42]
$C_{L_{max}}$	1.17	No high lift device required
η_{FF}	0.8	Typical value from [42]
FM	0.65	Typical value from [11]
p	800 W/kg	Typical value for LiPo batteries ([21])
\bar{e}	180 Wh/kg	Typical value for LiPo batteries ([21])
A_{prop}	0.3 m ²	Comparison with competitors

Table 1.2: Preliminary sizing parameters.

is the design philosophy adopted, it has been decided not to instal high lift devices due to the excessive complexity they would bring to a such small aircraft. For this reason, $C_{L_{max}}$ is limited to 1.17.

1.4.2 Preliminary sizing performance parameters

Now the performance parameters are considered. As mentioned in the introduction of the thesis, there is no particular requirement on performance. Given that, a bunch of endurance, stall speed and payload weight values has been investigated to decide the sizing ones. Competitors performance has been used to select a feasible range of values (speed values for competitors are in Table 1.3 while endurance values are in Table 1.1).

Two values of cruise endurance (85 min and 100 min) and hovering endurance (5 min and 10 min) requirements have been considered in the sizing procedure. The aim of this process is to assess if there is a change in battery weight due to higher endurance requirements. Naturally, a change in battery weight brings also a change in the whole sizing result. After some computations it has been verified that there is no change in the obtained values of W_{TO} , S and P_b ; this is due to the battery sizing procedure: the battery weight

$$W_{batt} = \frac{g}{\eta} \max \left\{ \frac{P_b^{ho} \times t_{ho} + P_b^{cr} \times t_{cr} + P_b^{cl} \times 2 t_{cl}}{\bar{e}}, \frac{\max \left\{ P_b^{ho}, P_b^{cr}, P_b^{cl}, W_{TO} / \left(\frac{W_{TO}}{P_b} \right)_{FF} \right\}}{p} \right\} \quad (1.19)$$

is the result of a maximization procedure. Two battery weights are obtained, one

considering required energy and the other considering required power. W_{batt} is selected as the maximum between them.

In all the sizing cases in which endurance in cruise and hovering changes, battery weight considering power is greater than the one considering energy. Since a change in endurance has impact only on required energy and not required power (higher endurance means a longer mission, not higher power requirement), then only the battery weight considering required energy changes with endurance. Because the battery weight is related to power in the design case at hand, a change in endurance of +20% for cruise (100 min instead of 85 min) and +50% for hovering (10 min instead of 5 min) do not produce a change in the sizing. For larger changes to endurance a break-event point will be reached: at this point the W_{batt} considering energy will be larger than the one considering power. However, it is not in the interest of this work to find the endurance value for which this happens. The result of these considerations is that cruise endurance requirement is set to 85 min and hovering endurance requirement to 5 min.

The other parameters to be varied are stall speed and payload weight. Figure 1.6 shows the results of the sizing procedure for different values of these two variables. Considering Figure 1.6a, the 300 g_f payload option has been discarded in order to limit W_{TO} below 4 kg_f for all the considered stall speeds; in this way the VTOL UAV is inside the C2 class of the new European Union (EU) drone regulation ([17] and [18]). Therefore, to maximize the payload weight that can be carried being at the same time in C2 class, $W_{pl} = 200$ g_f. The rationale to select the stall speed is “the lower the better”, so the time for transition from vertical flight only to forward flight only is minimized. Considering Figure 1.6b, the stall speed has been chosen equal to 11 m/s to limit the wing span to 2 m: this is the lowest v_s , among the considered ones, to satisfy $b < 2$ m with $W_{pl} = 200$ g_f.

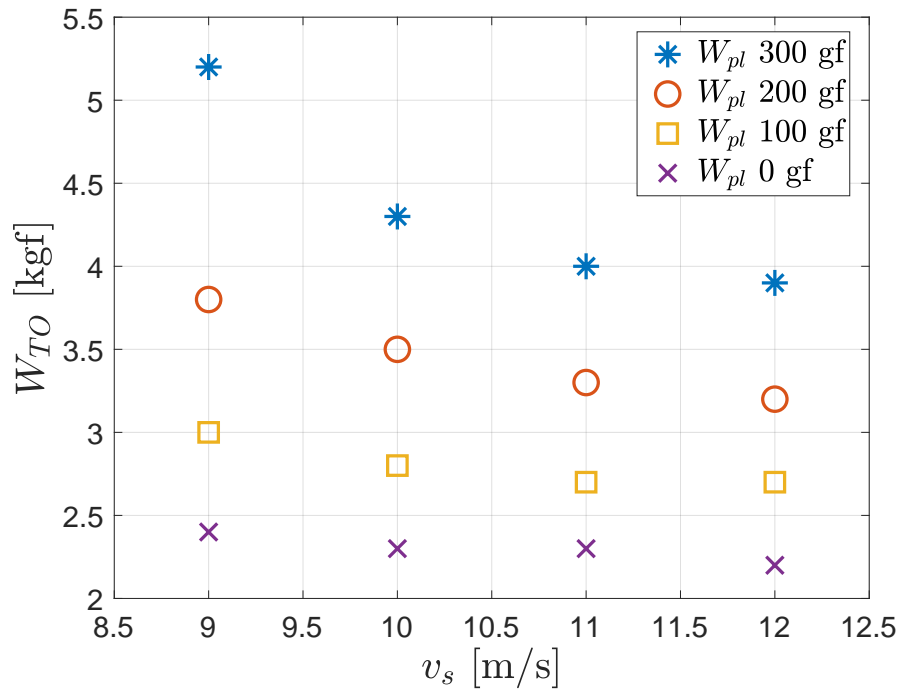
Some other performance parameters are directly fixed and explained in the following list:

- operative altitude is set equal to 120 m above ground level (AGL), as required from the EU drone regulation ([17] and [18]) for UAVs inside the C2 class;
- cruise speed is set equal to 15 m/s and maximum speed to 22 m/s, both similar to competitors;
- the maximum rate of climb ROC is set equal to 2 m/s since NATO standard AEP-83 regulation [19] states that, for UAVs with take-off weight not greater than 150 kg_f and impact energy greater than 66 J, the sea level rate of climb should be at least 1.5 m/s. An attempt of sizing with $ROC = 3$ m/s has been done but the obtained W_{TO} was too large, so ROC has been fixed to 2 m/s.

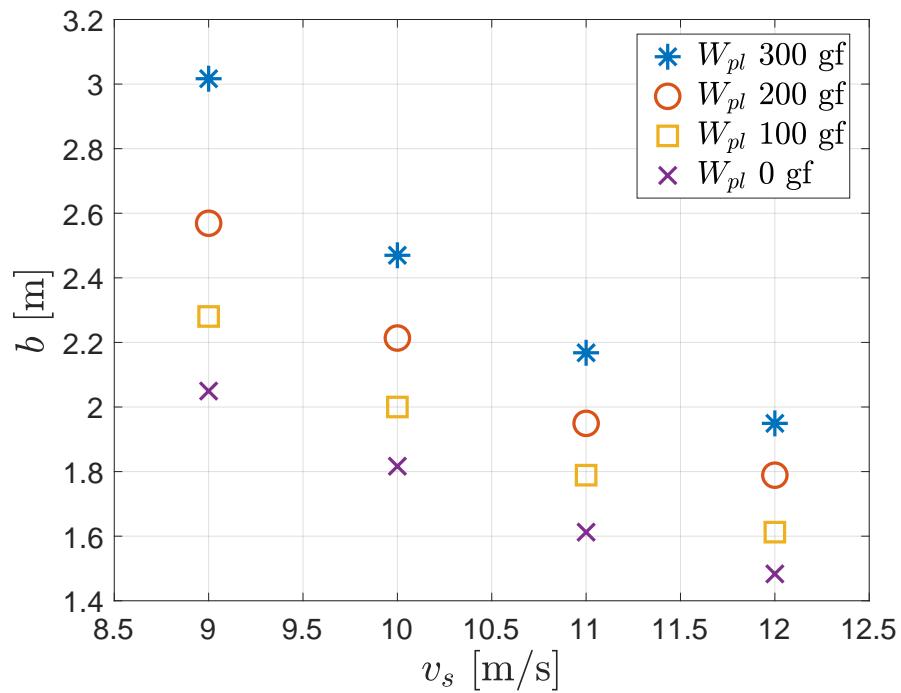
Table 1.4 summarizes all the performance parameters adopted.

Model	v_{max} [m/s]	v_{cr} [m/s]	v_s [m/s]
Wing	31.3	-	-
DeltaQuad Pro #Cargo	28.0	18.0	12.0
Wingtra One	-	16.0	-
Kapetair VTOL UAV	-	18.0	5.6
Tigerwing	-	9.7	-
Trinity F90+	-	17.0	-
Tron F90+	-	18.0	-
Vector	25.0	15.0	-
UAV Birdie VTOL	-	17.0	-
Skyproowler 2	36.0	22.0	-
Fusion	20.0	16.0	12.0
ZT-3V	-	19.5	-
Avy	27.8	19.5	-
Savant	38.0	-	-
EOS C UAS	27.8	-	-
Kestrel	36.0	19.5	-
Wingcopter 178	36.0	-	11.0
Sama UAV VTOL	27.8	19.5	7.0
SP9 VTOL	-	15.0	-
Hawk-Eagle 01	30.6	25.0	-
Eagle Hero VTOL	31.0	24.0	20.0
Ranger VTOL	33.3	16.7	13.3
Dragon VTOL	30.6	23.0	13.3
VTOL UAV [11]	30.0	-	11.0
Wingcopter 178 HL	36.0	-	11.0
Penguin BE	36.0	22.0	11.0

Table 1.3: Competitors speed range. Data are taken from manufacturers websites ([6], [27], [10], [28], [29], [26], [30], [31],[32], [33], [34], [35], [36], [37], [9], [38], [39], [40] and [41]); symbol - states that data is not available.



(a) Take-off weight values changing stall speed and payload weight.



(b) Wing span values changing stall speed and payload weight.

Figure 1.6: Sizing results for different stall speeds and payload weights.

Parameter	Value
v_s	11 m/s
v_{cr}	15 m/s
v_{max}	22 m/s
ROC	2 m/s
h	120 m AGL
t_{ho}	5 min
t_{cr}	85 min
W_{pl}	200 g _f

Table 1.4: Summary of preliminary sizing performance parameters.

1.4.3 Preliminary sizing results

Once the values to be used in the preliminary design phase have been decided, the sizing procedure is performed. The selected design point is shown in Figure 1.7. This point is the best in terms of power loading (higher power loading means lower power requirement) and wing loading (higher wing loading means smaller wing surface). A margin is considered between the design point and the constraints lines to assure tolerance to parameter uncertainties. The results of the sizing procedure are presented in the following list:

- $W_{TO} = 3.3$ kg_f;
- $W_{batt} = 1.0$ kg_f;
- $W_E = 2.1$ kg_f;
- $P_b^{FF} = 90$ W;
- $P_b^{VF} = 430$ W;
- $S = 0.38$ m²;
- $b = 1.95$ m.

1.5 Sensitivity analysis

In the preliminary design stages some parameters are known with uncertainties or are estimated starting from typical values found in literature, so it is worth performing a sensitivity analysis on the most uncertain ones to assure design point robustness. Moreover, there can be trends inside the competitors database based on year or material: thanks to new technologies, recent models can weight

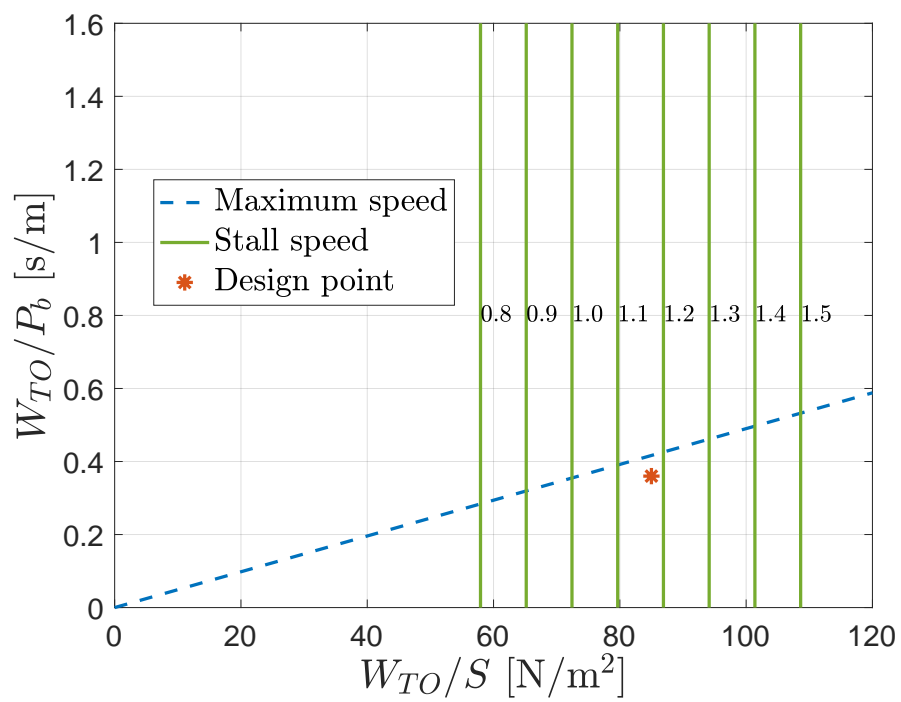


Figure 1.7: Initial sizing matrix plot. The stall speed constraint is parameterized as function of the maximum lift coefficient $C_{L_{max}}$, the values of which are written near the corresponding constraint line.

less than the older one for example. Table 1.5 presents the iterations performed to check this and the related effects on the weight regression line. The statistical database of Table 1.1 has been analyzed in depth considering both materials and year of first production. Four groups are identified:

- all models;
- composite-made models;
- recent (*i.e.*, after 2016) models;
- composite-made and recent models.

It can be seen from Table 1.5 that the greatest change in W_{TO} is due to the year of introduction on the market; this can be explained considering that in the recent years VTOL UAVs and UAVs in general have had a great development. Moreover, one of the older models, the Penguin BE, performs conventional take-off and landing instead of vertical ones. It has been considered due to its higher W_{TO} with respect to the other models to increase the considered range of take-off weights for the W_E regression but it is not a VTOL UAV. Since considerations about construction materials produce only small variations, the selected database for the preliminary sizing is the third one: only models introduced in the market after 2016, regardless of their materials to have a larger database. Figure 1.8 presents the regression line considering the whole database and the one considering only recent models for an immediate comparison.

Sensitivity on C_{D_0} and η_{FF} is shown in Figure 1.9 on the SMP. C_{D_0} is perturbed by $\pm 20\%$ while η_{FF} by $\pm 10\%$. Figure 1.9a shows that a slight change of the design point has been done to ensure robustness to C_{D_0} uncertainty. The design point power loading is moved from 0.36 s/m to 0.32 s/m; the wing loading remain constant to 85 N/m². Figure 1.9b shows that the design point selected after C_{D_0} sensitivity is robust to uncertainties regarding η_{FF} . So, the final design point has wing loading equal to 85 N/m² and power loading equal to 0.32 s/m.

Summarizing after the sensitivity analysis, the final preliminary design point is characterized by the values in Table 1.6. Some considerations about the obtained results: in Section 1.4 it was decided to discard some payload weights and stall speeds to keep W_{TO} below 4 kg_f and the wing span below 2 m. The UAV presented in Table 1.6 does not satisfy both these requirements being $W_{TO} = 4.4$ kg_f and $b = 2.26$ m. This is not considered a problem given the iterative nature of the design process: the difference is quite small (+10 % in W_{TO} and +13 % in b) and it is also the result of a conservative approach. It is important to remember that these two constraints are not mandatory for the project but have been used in the design process as choice criteria. In the following design stages the values of W_{TO} and b will be monitored to check if it is possible to satisfy the proposed constraints ($W_{TO} \leq 4$ kg_f and $b \leq 2$ m).

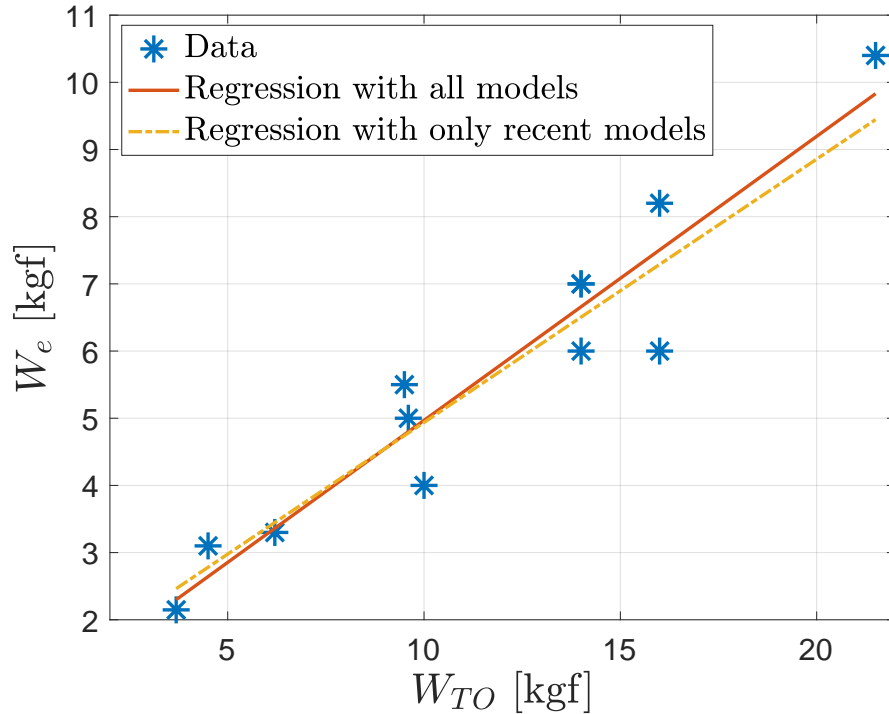
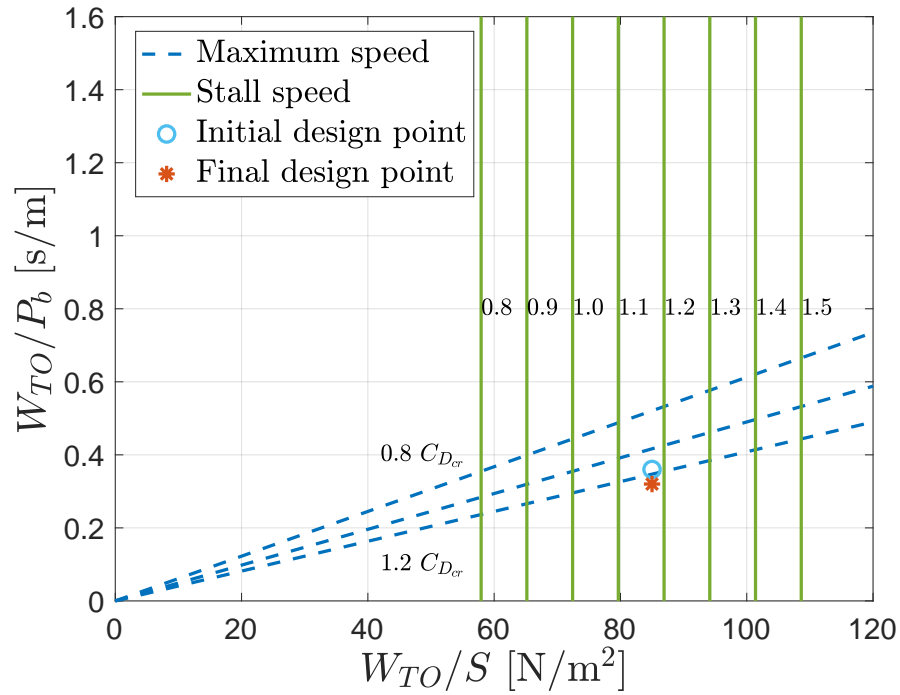


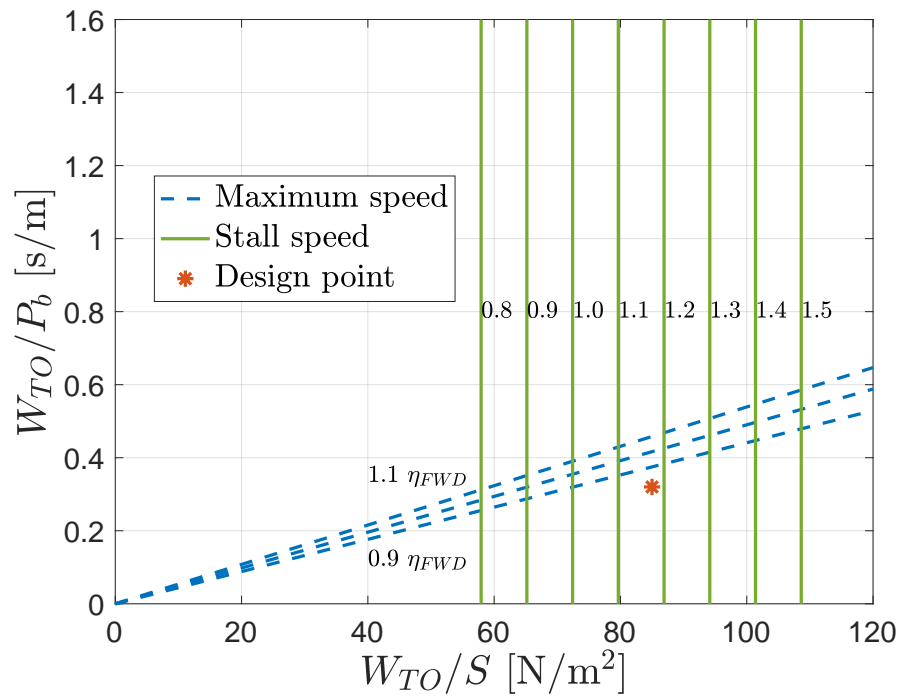
Figure 1.8: Regression line for $W_E(W_{TO})$ comparison. The change based on the considered database can be seen clearly.

W_{TO} [kgf]	W_{batt} [kgf]	W_E [kgf]	P_b^{FF} [W]	P_b^{VF} [W]	S [m ²]	b [m]	Considered database
3.3	1.0	2.1	90	430	0.38	1.95	All models in database
3.4	1.0	2.2	90	450	0.39	1.97	Composite models
4.4	1.5	2.7	120	655	0.48	2.19	Recent models
4.8	1.6	2.9	130	730	0.55	2.35	Composite, recent models

Table 1.5: Sensitivity analysis iterations. The first block shows the sizing result obtained in Section 1.4; the second one the iterations changing the statistical database for $W_E - W_{TO}$ regression.



(a) SMP sensitivity to C_{D_0} .



(b) SMP sensitivity to η_{FF} .

Figure 1.9: SMP sensitivity.

Parameter	Value	Parameter	Value
k	0.046	C_{D_0}	0.023
$C_{D_{cr}}$	$1.1 \times C_{D_0}$	$C_{L_{max}}$	1.15
η_{FF}	0.8	FM	0.65
p	800 W/kg	\bar{e}	180 Wh/kg
v_s	11 m/s	v_{cr}	15 m/s
v_{max}	22 m/s	ROC	2 m/s
h	120 m AGL	t_{ho}	5 min
t_{cr}	85 min	AR	10
S	0.51 m ²	b	2.26 m
W_{TO}	4.4 kg _f	W_{batt}	1.5 kg _f
W_E	2.7 kg _f	W_{pl}	200 g _f
P_b^{VF}	655 W	P_b^{FF}	135 W
$\left(\frac{W_{TO}}{P_b^{FF}}\right)$	0.32 s/m	$\left(\frac{W_{TO}}{S}\right)$	85 N/m ²

Table 1.6: Final values of the preliminary design.

Chapter 2

Aerodynamic design

Once the first aircraft parameters such as W_{TO} , S , P_b^{FF} and P_b^{VF} have been defined, the detail design can start. In this phase aerodynamic and structural design are carried out along with the choice of engines and internal components. It is important to consider the deep interactions between each element: wing aerodynamic design influences the wing structural design, the disposition inside the fuselage of electronics guides the fuselage layout and the aircraft static stability. This is a deeply connected design phase and this must be taken into account for the success of the project. Moreover, this is an iterative phase because changes in one field influences all the project and some parameters have to be updated.

This chapter presents the aerodynamic design of wing and tail. The objective is to define wing and tail configuration: airfoil sections used, geometrical parameters and relative position between wing and tail. The adopted design procedure is taken from [22] and explained in the present chapter.

The starting point of wing design are the required lift coefficient in cruise conditions, $C_{L_{cr}}$, and the maximum lift coefficient $C_{L_{max}}$, fixed when the design point on the SMP was chosen. These values are used in the choice of the airfoil section; the geometrical parameters, instead, are computed starting from literature and simple considerations about aircraft operating conditions. It is important remembering that the wing surface S , the wing span b and the aspect ratio AR have already been fixed in Chapter 1. For what concerns the tail, the first step is the selection of the configuration. Once it has been selected, tail airfoil section and geometrical parameters are designed. It is now possible to simulate the wing-tail assembly with XFLR5, an open-source aerodynamics software which uses a panel method to compute the aerodynamic forces. With this step the proposed design is tested and verified. If necessary some iterations on design parameters are performed to achieve a satisfying result. A brief introduction to XFLR5 for the interested reader can be found in Appendix A.

2.1 Wing airfoil selection

The airfoil section is the main element responsible for generating the required lift. An airfoil can be designed specifically for the case at hand or taken from the numerous databases of already designed airfoils available in the literature. The first option offers the possibility to adopt a custom-made airfoil which suits the aircraft operative conditions perfectly; however, the process of designing an airfoil with good performance is not easy, specially for beginners. The second option allows to use an airfoil already designed and tested from expert aerodynamicists; nowadays there are lots of airfoil sections for every purpose, so a proper one can be easily found even if not tailored.

For this project the second method has been adopted; in the future different airfoil sections could be used, including a custom-made one, since wing interchangeability is one of the requirements. Following the suggestion in [22], the airfoil database of the Department of Aerospace Engineering of the University of Illinois at Urbana - Champaign has been used [47]. Particular attention has been given to the range of Reynolds number R_e for which each airfoil family has been designed, considering that the UAV flies at low Reynolds number, more or less 2×10^5 , in cruise conditions. The Reynolds number is defined as

$$R_e = \frac{\rho v l}{\mu} \quad (2.1)$$

with ρ air density, v velocity, l characteristic length (in the case of an aircraft it is the mean aerodynamic chord MAC) and μ kinematic viscosity. This last value is obtained using the Sutherland formula suggested in [21],

$$\mu = 0.00001716 \left(\frac{T}{273.1} \right)^{1.5} \frac{383.7}{T + 110.6}, \quad (2.2)$$

where T is the air temperature in degree Kelvin.

The following list presents the airfoils selected from the adopted database and suitable for low Reynolds flight:

- Eppler airfoils for low Reynolds;
- Eppler airfoils for general purpose;
- Eppler airfoils for general aviation;
- NACA series 4;
- NACA series 5;
- NACA series 6;
- Selig airfoils for low Reynolds;

- Wortmann airfoils for low Reynolds;
- various airfoils for low Reynolds ¹.

The airfoil selection method explained in [22] has been used to choose the proper one. This method is presented in the following applied to the VTOL UAV case.

- First, the desired airfoil lift coefficient in cruise conditions, $C_{l_{cr}}$, and the airfoil maximum lift coefficient, $C_{l_{max}}$, have to be computed. As it can be seen from the notation, the airfoil lift coefficient C_l is different from the aircraft lift coefficient C_L . The passage from one to the other is done as follows:

$$C_l = \frac{C_L}{0.90 \times 0.95}. \quad (2.3)$$

The factors 0.90 and 0.95 account for the fact that, in a conventional configuration, the tail is down-lifting so the wing lift must be greater than lift required for vertical equilibrium and that the wing AR is finite, so the generated lift is less than the one of a theoretically infinite wing.

The desired lift coefficient $C_{l_{cr}}$ is computed starting from vertical equilibrium in cruise conditions,

$$W_{TO} = \frac{1}{2} \rho_{cr} v_{cr}^2 S C_{L_{cr}}; \quad (2.4)$$

the desired airfoil lift coefficient is easily obtained substituting

$$C_{L_{cr}} = \frac{2W_{TO}}{\rho_{cr} v_{cr}^2 S} \quad (2.5)$$

into equation (2.3). The maximum airfoil lift coefficient $C_{l_{max}}$ is computed from the $C_{L_{max}}$ adopted in the SMP with the transformation in equation (2.3).

The required $C_{L_{cr}}$ is computed substituting the UAV values shown in Table 1.6 inside equation (2.5). The obtained value is transformed into the equivalent airfoil value with equation (2.3); the result is $C_{l_{cr}} = 0.738$. With the same procedure, $C_{l_{max}} = 1.368$ is obtained.

¹This group includes airfoils from different families; since they are few for each one they are collected together. They are all designed for low Reynolds operations. This group includes airfoils designed by B. Dillner, C. Robertson, M. Drela, D. Fraser, M. Bame, M. Hepperle and M. Fox.

- The next step is to compute the lift coefficient in cruise conditions and the maximum lift coefficient for each considered airfoil. Cruise is selected since it is the longest operating condition for the UAV. To compute these two values, all the considered airfoils are simulated using XFLR5 at Reynold number conditions equivalent to the cruise one. The simulations are performed using potential flow computations. $C_{l_{max}}$ is the maximum value reached in the simulation while $C_{l_{cr}}$ is the lift coefficient of best lift to drag ratio. This last consideration stems from the fact that, for propeller driven aircraft, the maximum lift to drag ratio condition is the one which maximizes cruise range as explained in [48].
- The selection of the proper airfoils is performed with a graphical comparison: the desired $C_{l_{max}}$ and $C_{l_{cr}}$ are plotted in a graph with the corresponding values of each airfoil; the airfoil nearest to the desired values is selected. In case of not-evident situation with multiple nearer airfoils, an optimization procedure can be used considering other aerodynamics aspects such as zero lift drag coefficient or stall behavior. The graphical comparison of each airfoil family is presented in Appendix B for the interested reader. From each plot the nearer cases, if any, are collected; Figure 2.1 shows them all together. In this case, an airfoil is almost coincident with the desired one, so there is no need of further investigations. This airfoil is the Selig 2046, shown in Figure 2.2; its $C_{l_{cr}}$ is 0.738 (equal to the desired one) while its $C_{l_{max}}$ is 1.364 (the desired one is 1.368). The maximum airfoil thickness over chord ratio is 9%, which gives a small maximum thickness of 2 cm since the wing mean aerodynamic chord is 22 cm. However, only structural components have to be inside the wing since no fuel tank has to be installed, so the reduced thickness is a marginal problem.

2.2 Wing geometry

Once the airfoil has been selected, the other wing parameters are chosen. The first one is the wing vertical position; there are several possibilities: low wing, mid-wing, high wing and parasol wing, shown in Figure 2.3. References [21] and [22] recommend to consider the operational requirements of the project (for example high wing for cargo aircraft to ease loading and unloading operations around it). In the case of this UAV, the wing vertical location is chosen based on the disassembly requirement and engine position: it is easier to attach the wing to the fuselage if it is in the upper part of the aircraft facing directly the operator. Moreover, with a high wing the FF engines can be installed with a larger distance from the ground. Figure 2.4 shows these two advantages of a high wing with respect to a low wing.

For what concerns the dihedral angle Γ and the sweep angle Λ , they are set both to zero. The dihedral angle is related to lateral stability and, since an high

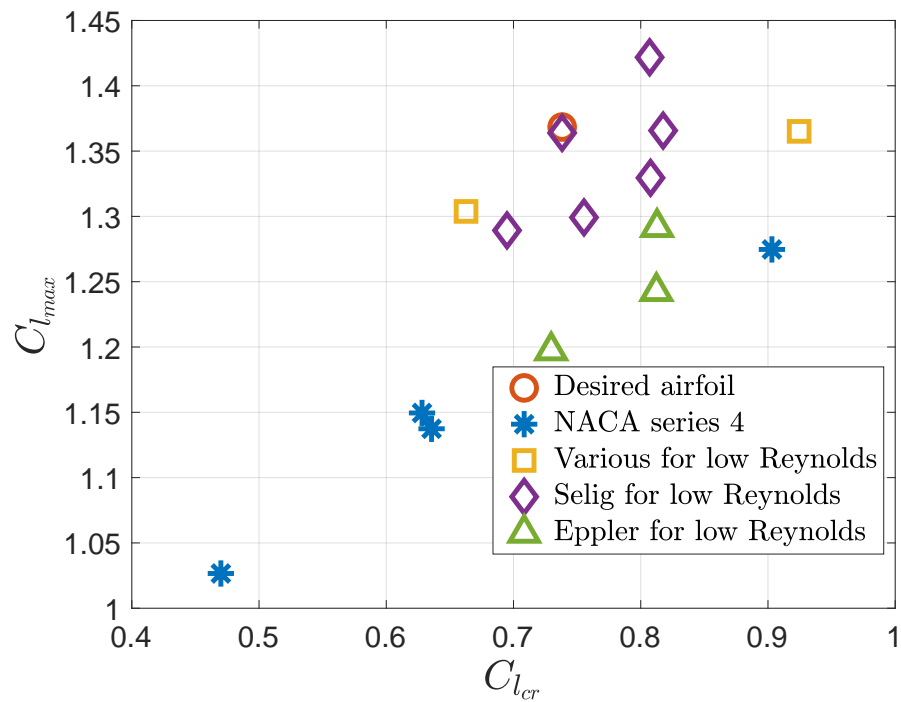


Figure 2.1: Nearest airfoils to the desired case. It can be clearly seen that one airfoil, the Selig 2046, is almost coincident with the required values.

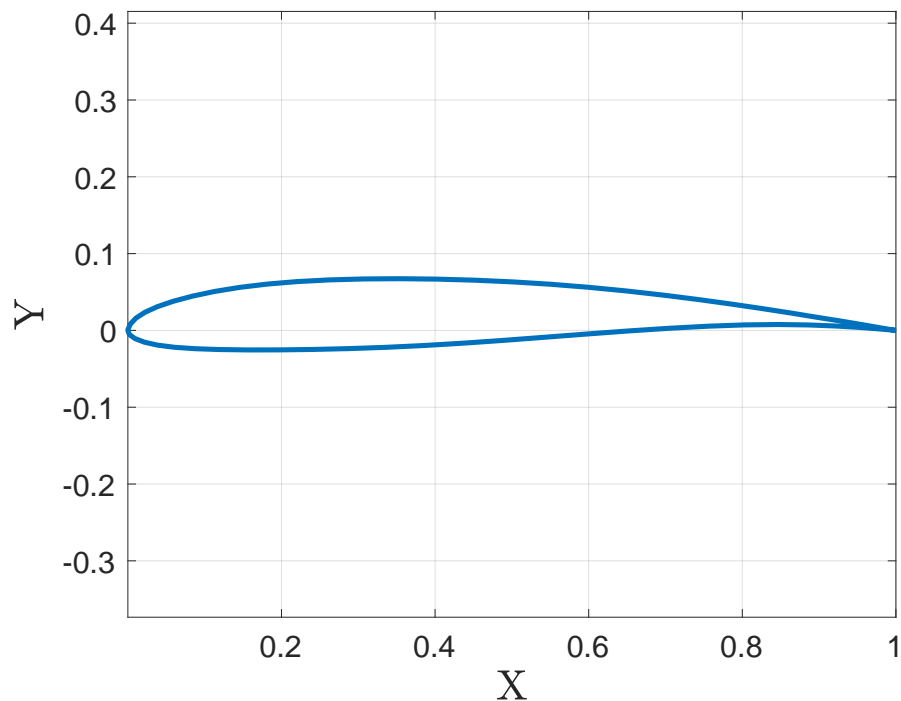


Figure 2.2: Selig 2046 airfoil. It is presented dimensionless with respect to the chord, both in X and Y ; airfoil coordinates are taken from [47].

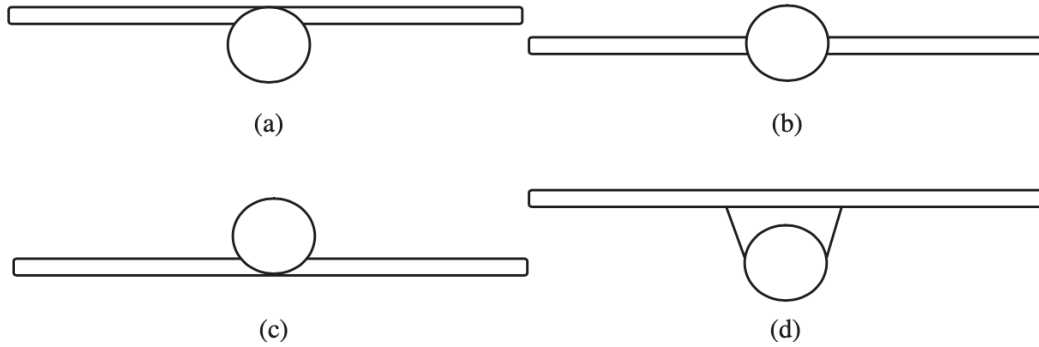


Figure 2.3: Wing vertical location: (a) is a high wing, (b) is a mid-wing, (c) is a low wing and (d) a parasol wing. Source [22].

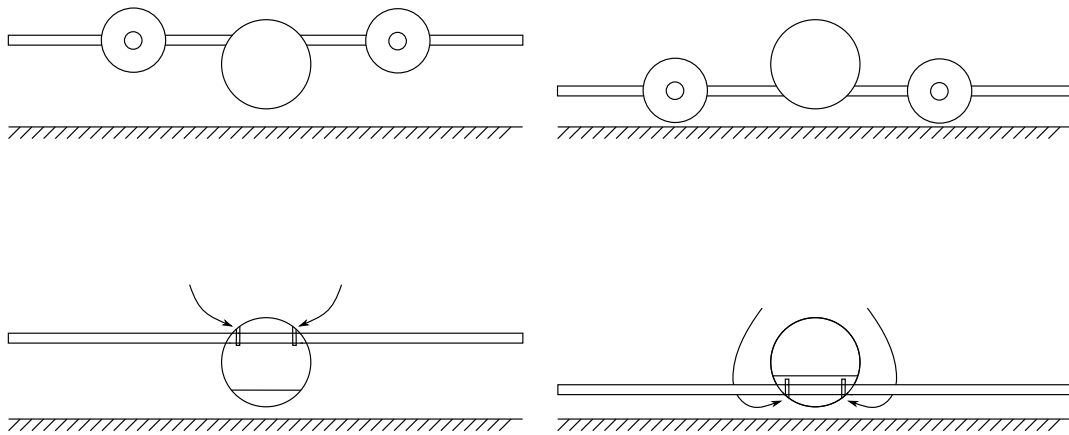


Figure 2.4: High wing pros with respect to a low wing for the VTOL UAV. The advantage from a propulsive point of view is presented on top: FF engines have a greater clearance from ground so they do not touch ground before take-off and after landing. On the lower part it can be seen that it is easier to attach the wing to the fuselage if the wing is high.

wing has a stabilizing effect, Γ should be negative to compensate and avoid a too stable aircraft, *i.e.*, a not very maneuverable one. In this case it has been decided to set $\Gamma = 0^\circ$ considering that high maneuverability is not the focus of the aircraft; moreover, no dihedral angle makes the construction easier. As explained in reference [22], no sweep angle is recommended for low subsonic aircraft (less than Mach number 0.3) since its disadvantages would negate all the improvements produced. The Mach number is defined as

$$M_a = \frac{v}{a} \quad (2.6)$$

with a speed of sound. Given that the Mach number M_a of the UAV is 0.084, the flight regime is highly subsonic.

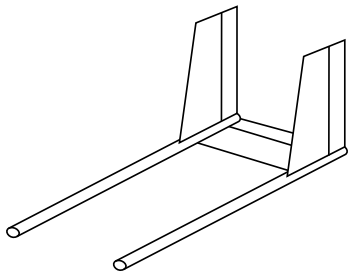
Only the taper ratio λ and the wing incidence i_w have to be fixed to define completely the wing geometry. λ is chosen considering the lift and induced drag distributions along the wing span. Since these distributions are computed with XFLR5 simulation of the wing-tail assembly, the taper ratio will be fixed once the tail has been designed. Regarding wing incidence, the angle i_w is chosen starting from Selig 2046 potential flow analysis so that, when the aircraft angle of attack (AoA) is zero, the airfoil AoA is equal to the one of maximum lift to drag ratio. As already mentioned, best lift to drag ratio condition is the one which maximizes the endurance, so it is the best one for cruise. The AoA corresponding to best lift to drag ratio condition, according to XFLR5 simulations, is 4° , so it is decided $i_w = 4^\circ$.

2.3 Tail configuration

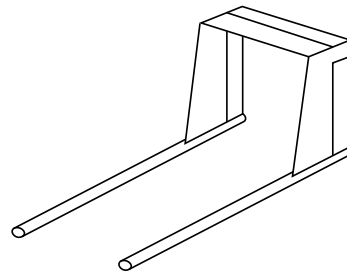
The first step to design the tail is the definition of its configuration. After a literature survey ([21], [22] and [23]) four tail options are selected for comparison. Since the dual system configuration selected in Section 1.1 for the VTOL UAV has two booms under the wings for VF engines, it is a smart choice to use these booms also for the tail. Figure 2.5 presents the four options: a U tail (Figure 2.5a), an inverted U tail (Figure 2.5b), a V tail (Figure 2.5c) and an inverted V tail (Figure 2.5d).

To ease the comparison, the information in the literature is collected in Table 2.1, which presents pros and cons of each tail option. Control and structural aspects are the main drivers in the choice. Since the UAV is not an academic exercise but has actually to be produced, also simple practical aspects related to construction are considered in the evaluation.

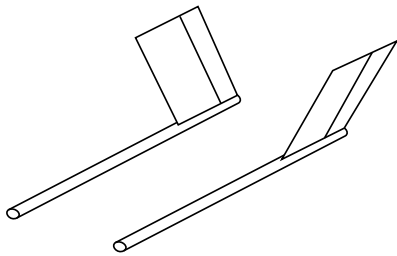
Considering Table 2.1, several groups can be highlighted. There is a clear division between hyperstatic (U, inverted U and inverted V options) and non-hyperstatic (V option) structures: from a structural design perspective the latter is more attractive. There is a group with conventional control surfaces (the U tails) and one with non conventional (the V tails). The two U options feature



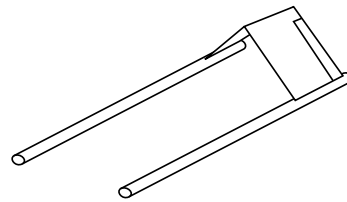
(a) U tail configuration.



(b) Inverted U tail configuration.



(c) V tail configuration.



(d) Inverted V tail configuration.

Figure 2.5: Tail configuration options.

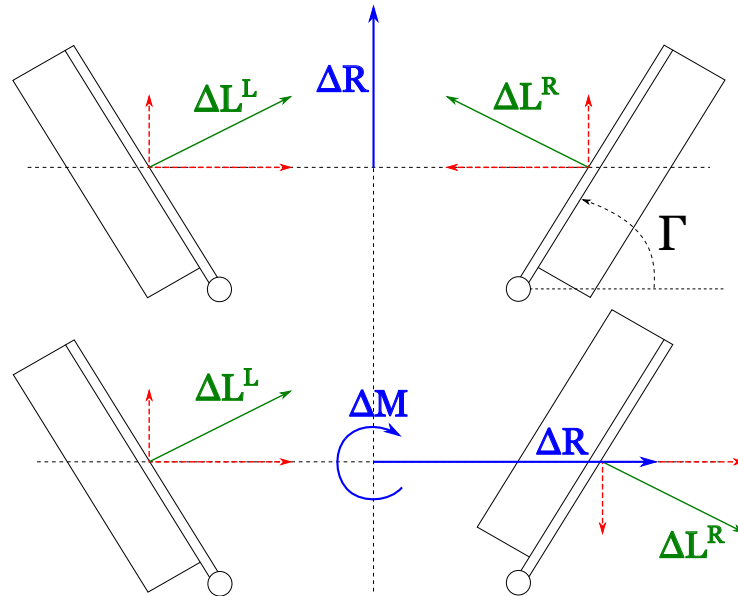


Figure 2.6: V tail moving surfaces as elevator and rudder.

horizontal elevator and vertical rudder. The V tails have only two surfaces and their deflection has to be combined to act as elevator or rudder, as shown in Figure 2.6: a symmetric deflection results in a vertical-only resultant like a conventional elevator; an anti-symmetric deflection produces a lateral force as a conventional rudder. In this last case there is also a moment due to the distance from the central axis.

Between V and inverted V configurations, the former is better since it has few components (as the latter) but it is not hyperstatic. The inverted V tail is then discarded. With only literature information it is not possible to evaluate if the V tail stiffness is (too) inferior compared to the U/inverted U one. Given this, a more in depth structural analysis is required. Moreover, also longitudinal static stability has to be compared since [22] states that the V tail configuration may have some deficiencies in it. A U tail and a V tail with similar characteristics will be designed and compared both from a structural and a static stability point of view.

Some further considerations before starting the double tail design: the U configuration is a more common option and seems to be structurally better. The V tail is preferable from a practical point of view, since it has less parts (so less joints and easier production) and less actuators for moving surfaces; however, it seems to be less rigid since it is not a closed structural loop. Looking to competitors (Table 1.1), it can be noticed that all options presented in Figure 2.5 are used; however, only Google X Wing (shown in Figure 1.1a) adopts the V tail on separate booms, the other V tails are directly attached to the fuselage.

	Pros	Cons
U tail	This tail features separated control surfaces, so there is no interference between rudder and elevator action. From a structural point of view, this is a closed loop with the wing, so it should have higher stiffness.	Being an hyperstatic structure, the structural design is a little more complicated. There can be aerodynamic interference between the FF engines and the elevator since this moving surface is in their wake. There are three moving surfaces, so more components and actuators than for V and inverted V tails.
Inverted U tail	This tail configuration has the same pros of a U tail (separate moving surfaces and higher stiffness) plus there is no/less interference between FF engines and the elevator.	As for the U tail, also the inverted U tail has three parts and is structurally hyperstatic.
V tail	This tail is composed of only two surfaces, so there is less components to be manufactured and less actuators to be installed. This structure is very easy to be studied since it is not hyperstatic.	Elevator and rudder effects are obtained, respectively, by symmetric deflection and by asymmetric deflection, so the use of tail moving surfaces is more complex. Since there is no structural closed loop, this tail could have less structural stiffness. Also, it may presents deficiencies in maintaining longitudinal static stability.
Inverted V tail	As for the V tail, there are only two moving surfaces so less components to be manufactured and less actuators. This is a closed loop structure, so it has higher rigidity with respect to the V tail option.	Same cons of the V tail plus the fact that it is a hyperstatic structure.

Table 2.1: Tail options pros and cons for an immediate comparison.

Reference	V_h	V_v
[22]	0.50 - 0.70	0.030 - 0.040
[23]	0.50	0.020 - 0.040
[11]	0.53 - 0.70	0.022 - 0.032
Selected value	0.50	0.030

Table 2.2: Horizontal and vertical tail volumes for aircraft flying in similar conditions.

2.4 U tail and V tail design

In this section the U tail and the V tail are designed. The procedure proposed in [22] is used for the U tail; for the V tail a custom procedure is developed based on references [22] and [23]. First the U tail design is explained, then the V tail one.

2.4.1 U tail design

The tail objective is to ensure equilibrium and stability in the horizontal and directional planes. A simple means to evaluate the tail effects on trim and stability are the horizontal tail volume

$$V_h = \frac{l S_h}{MAC S} \quad (2.7)$$

and vertical tail volume

$$V_v = \frac{l S_v}{b S}, \quad (2.8)$$

where l is the tail arm (distance between wing aerodynamic center and horizontal tail aerodynamic center), S_h is the horizontal tail surface, S_v the vertical tail surface, MAC is the wing mean aerodynamic chord, S the wing surface and b the wing span.

Typical values are assumed for both these coefficients starting from similar aircraft. Table 2.2 presents the values proposed by references [11], [22] and [23] for gliders, home-build and general aviation single prop-driven engines (no particular indication is given for small unmanned aircraft so “similar” categories are considered).

The selected values are the mean ones of each proposed range. As it is clear from equation (2.7) and equation (2.8), it is necessary either to fix or the tail arm or the tail surface to compute the other, once the tail volume is selected. In fact, the same tail volume can be obtained both with a long tail arm and a small tail surface or with a short tail arm and a large tail surface. To select the optimal couple arm-surface a criterion has to be selected. Both reference [22] and

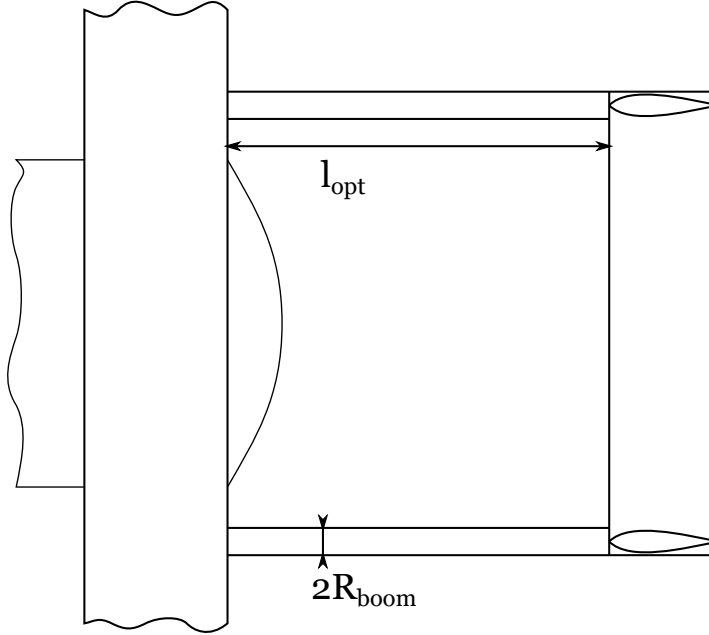


Figure 2.7: Aircraft aft-part wet surface in the case of a U tail. S_{wet}^{aft} depends only on the tail arm l .

reference [23] suggest to consider the wetted surface area of the rear part of the fuselage. This wetted area is related to the induced drag produced by the aircraft: minimizing the wetted area also the induced drag is minimized. The wetted area of the aircraft aft-part, S_{wet}^{aft} , is function of both the tail arm and the tail surface. The tail surface can be written as function of the tail arm manipulating equations (2.7) and (2.8); the result is

$$S_{wet}^{aft}(l) = 4\pi R_{boom}l + 2\frac{V_h S MAC}{l} + 2\frac{V_v Sb}{l} \quad (2.9)$$

based on the scheme in Figure 2.7. The three right hand side terms of equation (2.9) are, respectively, the boom wetted area, the horizontal tail wetted area and the vertical tail wetted area. R_{boom} is the tail boom radius.

To minimize S_{wet}^{aft} its derivative with respect to the tail arm l is computed

$$\frac{dS_{wet}^{aft}}{dl} = 4\pi R_{boom} - 2\frac{S(V_h MAC + V_v b)}{l^2}; \quad (2.10)$$

setting the right-hand side of equation (2.10) to zero and solving for l gives the optimum tail arm l_{opt}

$$l_{opt} = \sqrt{\frac{S}{2\pi} \frac{V_h MAC + V_v b}{R_{boom}}}. \quad (2.11)$$

A consideration about equation (2.9): the contribution of the fuselage behind the wing is neglected (whatever shape the fuselage has) since it is constant, so in the derivation of S_{wet}^{aft} with respect to l (equation (2.10)) it adds zero to l_{opt} .

The resulting l_{opt} for $V_h = 0.5$, $V_v = 0.03$ and S , b and MAC from Table 1.6 is 1.25 m. Starting from equations (2.7) and (2.8), the equations for horizontal tail surface and vertical tail surface are easily obtained:

$$S_h = \frac{V_h MAC S}{l_{opt}} \quad (2.12)$$

and

$$S_v = \frac{V_v b S}{l_{opt}}. \quad (2.13)$$

The computed tail surfaces are $S_h = 0.05 \text{ m}^2$ and $S_v = 0.01 \text{ m}^2$ (this last value is referred to one of the two vertical tails, the overall vertical tail surface is twice this value).

The next step is the selection of the tail airfoil. References [22] and [43] suggest to use a symmetric airfoil for both horizontal and vertical tail, so that the tail performs in the same way for both positive and negative AoA. Moreover, [22] states that the tail has to be free of compressibility effects. To enforce this the tail lift coefficient has to be less than the wing lift coefficient. This translates into the tail airfoil section being thinner than the wing one. An airfoil which satisfies both these criteria is the NACA 0008, which will be used as airfoil for both horizontal and vertical tail.

The tail sweep angle (both horizontal, Λ_h , and vertical, Λ_v) and the dihedral angle (both horizontal, Γ_h , and vertical, Γ_v) are set equal to the wing one, as suggested in [22]. So $\Gamma_h = \Gamma_v = \Lambda_h = \Lambda_v = 0$. The horizontal tail aspect ratio is

$$AR_h = \frac{2}{3} AR \quad (2.14)$$

according to [22]. For the vertical tail aspect ratio, AR_v , reference [22] suggests a value between 1 and 2. It is decided to select $AR_v = 2$. For both horizontal and vertical tail the taper ratio, respectively λ_h and λ_v , is set equal to 1 for ease of production. Moreover, given the small dimensions of the tail, it is not advisable to reduce at one end the chord length to prevent too small components.

An important parameter for the longitudinal static stability is the horizontal tail setting angle i_h . It is determined so that in cruise conditions the aircraft trim is reached without elevator deflection. Obviously the angle i_h obtained with this criterion does not guarantee the trim without control deflection in every flight condition. However, cruise is the longest flight phase. The starting point in the computation of i_h is the moment equilibrium around the center of gravity (CG)

$$\mathcal{M}_{ac}^{wf} + Ld - L^t l = 0 \quad (2.15)$$

for a generic two surface aircraft (Figure 2.8 as reference). The tail pitching moment is neglected since it is small with respect to the other terms. Thrust and drag are considered applied on a line passing through the CG to simplify the notation. Normalizing equation (2.15) with respect to $\frac{1}{2}\rho v^2 S$, the following is obtained:

$$C_{Mac}^{wf} MAC + C_L d - \gamma \sigma C_L^h l = 0 \quad (2.16)$$

where C_{Mac}^{wf} is the wing-fuselage pitching moment estimated as

$$C_{Mac}^{wf} = C_m \frac{AR \cos \Lambda^2}{AR + 2 \cos \Lambda} \quad (2.17)$$

according to reference [22] with C_m wing airfoil moment coefficient and Λ wing sweep angle. d is the distance between wing aerodynamic center and aircraft CG, C_L^h is the horizontal tail lift coefficient, l is the distance between aircraft CG and tail aerodynamic center,

$$\gamma = \frac{\frac{1}{2}\rho v_h^2}{\frac{1}{2}\rho v^2} \quad (2.18)$$

is the ratio between tail dynamic pressure and wing dynamic pressure and σ is the ratio between tail surface and wing surface. From equation (2.16)

$$C_L^h = \frac{C_{Mac}^{wf} MAC + d C_L}{\gamma \sigma l} \quad (2.19)$$

is computed and easily rearranged as

$$C_L^h = \frac{C_{Mac}^{wf} + \bar{d} C_L}{\gamma V_h} \quad (2.20)$$

with $\bar{d} = \frac{d}{MAC}$. From the tail lift coefficient the tail AoA, α_h is computed as

$$\alpha_h = \frac{C_L^h}{C_{L\alpha}^h}, \quad (2.21)$$

where $C_{L\alpha}^h$ is the tail lift curve slope. Reference [22] computes this value starting from the airfoil lift curve slope, *i.e.*,

$$C_{L\alpha}^h = \frac{C_{l\alpha}^h}{1 + \frac{C_{l\alpha}^h}{\pi AR_h}}. \quad (2.22)$$

The value of $C_{l\alpha}^h$ is taken from the aerodynamic data of the NACA 0008 airfoil at the proper Reynolds number range. The tail incidence is defined as

$$i_h = \alpha_h + \varepsilon \quad (2.23)$$

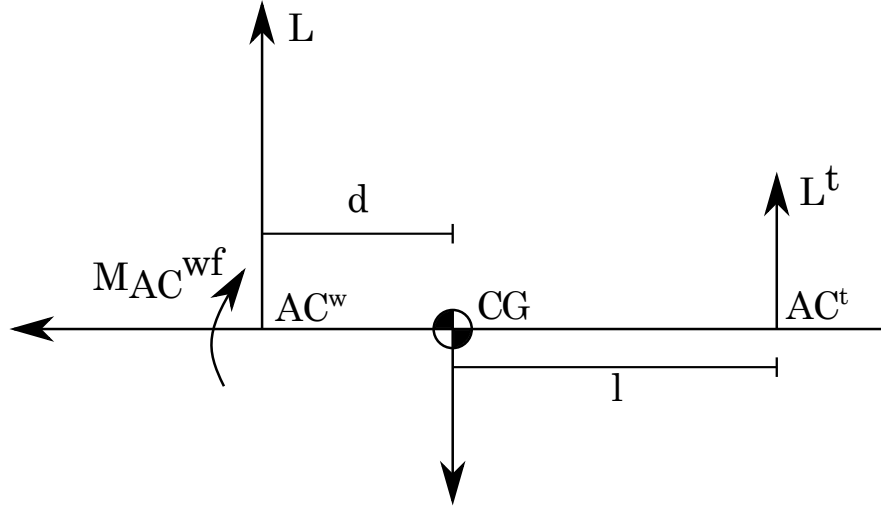


Figure 2.8: Simplified moment equilibrium scheme for tail incidence computation.

with ε downwash due to the main wing. A model of the downwash is proposed in reference [22] with a constant term ε_0 and a term proportional to the wing AoA α :

$$\varepsilon = \varepsilon_0 + \frac{\partial \varepsilon}{\partial \alpha} \alpha. \quad (2.24)$$

The downwash terms are computed according to the formulation proposed in [22] as

$$\varepsilon_0 = \frac{2C_L}{\pi AR} \quad (2.25)$$

and

$$\frac{\partial \varepsilon}{\partial \alpha} = \frac{2C_{L_\alpha}}{\pi AR} \quad (2.26)$$

where C_L and C_{L_α} are related to the wing. The value of wing C_{L_α} is computed with an analogous formulation as the one in equation (2.22). The final result of this procedure is a horizontal tail setting angle i_h of 3° . The choice of the vertical tail setting angle is much easier since [22] advises to select 0° ; in this way the vertical tail does not produce forces without control surface deflection.

To define completely the U tail, some geometrical parameters have to be decided: span b and mean aerodynamic chord MAC (both horizontal and vertical). They are found solving the following system of two equations in two unknowns:

$$AR_h = \frac{b_h}{MAC_h} \quad (2.27)$$

$$S_h = MAC_h b_h. \quad (2.28)$$

The same system can be written for vertical tail quantities changing the subscript h with v . The horizontal tail has $b_h = 63$ cm and $MAC_h = 10$ cm while the vertical tail has $b_v = 14$ cm and $MAC_v = 10$ cm.

2.4.2 V tail design

Once the U tail has been designed, the V tail is considered. The design procedure is developed starting from [22] and [23]. The parameters to be determined are:

- tail horizontal location,
- tail dihedral angle Γ , shown in Figure 2.6,
- airfoil section,
- tail surface,
- tail AR ,
- tail taper ratio,
- tail span and MAC .

The first parameter is determined as for the U tail: the wetted area of the aircraft aft-part is modeled as

$$S_{wet}^{aft}(l) = 4\pi R_{boom}l + 2\frac{V_v b S}{l} \frac{1}{\sin \Gamma} \quad (2.29)$$

where the first term is the booms wetted area and the second is the tail wetted area. As for the U tail, the aft-fuselage part is neglected since constant, so in the derivation process it goes away. The dihedral angle Γ is computed as in [23]:

$$\Gamma = \arctan\left(\frac{S_v}{S_h}\right), \quad (2.30)$$

where S_h is the projected area on the horizontal plane and S_v on the vertical plane. The tail vertical projected surface S_v and the horizontal projected surface S_h are computed with equations (2.12) and (2.13). Substituting them into equation (2.30), the following is obtained:

$$\Gamma = \arctan\left(\frac{V_v b}{V_h MAC}\right), \quad (2.31)$$

with b and MAC of the wing. Differentiating the right-hand side of equation (2.29) with respect to l and setting it to zero as for the U tail, it is obtained

$$l_{opt} = \sqrt{\frac{1}{2\pi} \frac{V_v b S}{\sin\left(\arctan\left(\frac{V_v b}{V_h MAC}\right)\right)} \frac{1}{R_{boom}}}. \quad (2.32)$$

The resulting l_{opt} for the case at hand, with the same horizontal and vertical tail volumes of the U tail ($V_h = 0.5$ and $V_v = 0.03$) is $l_{opt} = 1.03$ m. The dihedral angle Γ is computed with equation (2.31); the result is $\Gamma = 31^\circ$.

The selected airfoil section is the same as the U tail since the requirements on the tail airfoil are the same. The V tail surface S_{vt} is computed as

$$S_{vt} = \frac{S_v}{\sin \Gamma} \quad (2.33)$$

with S_v lateral area of the V tail, equivalent to the vertical area of a conventional tail. The result is $S_{vt} = 0.03$ m² for each one of the two parts. The V tail aspect ratio, AR_{vt} is set equal to $\frac{1}{3}AR$ starting from the value suggested in [22] ($\frac{1}{3}$ instead of $\frac{2}{3}$ to reduce the lateral dimensions of the tail). The taper ratio λ_{vt} is set, as for the U tail, to 1 to avoid difficulties in the production phase.

The last parameters needed to completely determine the V tail are the span b_{vt} and MAC_{vt} . They are computed with equations (2.27) and (2.28). The results are $b_{vt} = 33$ cm and $MAC_{vt} = 9$ cm.

2.5 U tail and V tail comparison

As stated in Section 2.3, the U tail and the V tail have to be compared from both a structural and a longitudinal static stability points of view. These comparisons are based on the data from XFLR5 simulations. A model made up of the sole lifting surfaces (wing and tail) is prepared for both tail options; Figure 2.9 and Figure 2.10 show the two models in XFLR5. The software produces an estimate of both aerodynamic loads and neutral point position. The aerodynamic loads are used for the structural comparison, the neutral point position for the longitudinal static stability evaluation.

In the structural comparison, the more concerning situation is a rudder maneuver: when the rudder is fully deflected the V tail should have larger displacement in the directional plane than the U tail since it is open. It is then decided to design a provisional rudder for both a V and a U tail. An equal deflection maneuver is simulated with XFLR5 to compute aerodynamic loads on the tail in each case. The obtained results are then compared to assess the structural effect. The rudder for U tail is designed with the procedure explained in [22]: a sizing condition has to be selected among asymmetric thrust due to one-engine-inoperative flight, crosswind landing or spin recovery; the rudder design is performed with reference to the most demanding condition. In the case at hand, the most demanding condition is asymmetric thrust since landing is performed vertically as multi-rotor and no acrobatic maneuver is required. The V tail rudder is sized using the procedure proposed in [49] starting from the values of control derivatives $C_{n\delta_r}$ (yawing moment coefficient derivative with respect to rudder deflection) and $C_{m\delta_e}$ (pitching moment coefficient derivative with respect to elevator deflection) of the

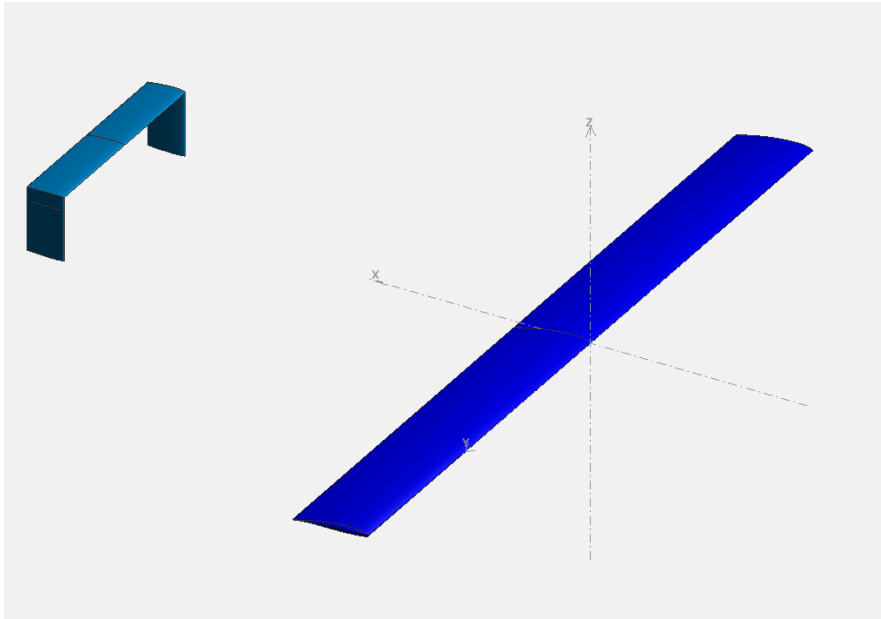


Figure 2.9: U tail model in XFLR5.

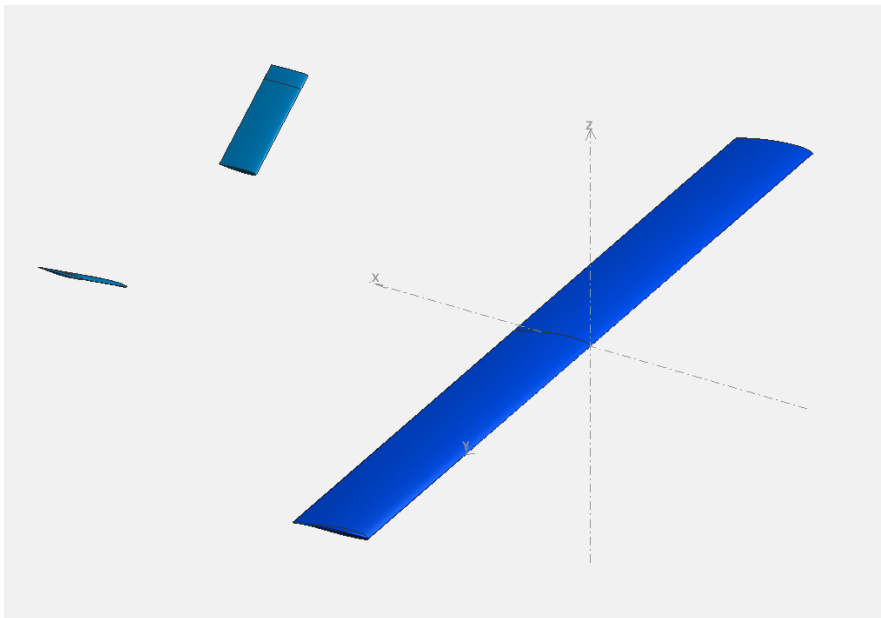


Figure 2.10: V tail model in XFLR5.

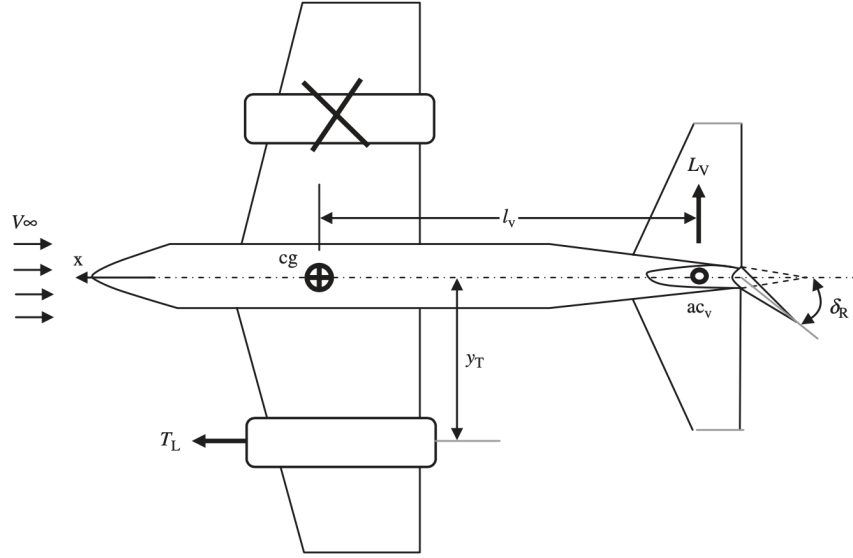


Figure 2.11: One engine inoperative scheme for rudder design; source [22].

U tail. This choice is done to ensure similar control performance between U and V tails.

A rudder is completely designed when its span b_r , chord MAC_r and maximum positive and negative deflections, δ_r^{max+} and δ_r^{max-} , are defined. The typical values suggested in [22] are $\frac{b_r}{b_v} = 0.7$, $\delta_r^{max+} = 30^\circ$ and $\delta_r^{max-} = -30^\circ$. The chords ratio $\frac{MAC_r}{MAC_v}$ will be determined starting from the one engine inoperative condition scheme in Figure 2.11. The CG position is assumed, in a preliminary way, coincident with the point at $\frac{MAC}{2}$ of the wing. This consideration is based on the assumptions that the VF engine distribution is symmetric between front and rear part of the aircraft and that the fuselage CG is approximately located at half of the wing chord. The FF engine is supposed to be at half of the semi wingspan, so the engine location $y_T = \frac{b}{4}$ from the center line of the aircraft. Information about VF and FF motors is available at this stage of design (even if they are explained in Chapter 4 due to the topic-oriented rather than time-oriented organization of the thesis). The one engine operative is assumed to produce its maximum thrust which is, in the case of the selected VF engine, $\mathcal{T}_L = 750 \text{ gf}$.

The yawing moment about the aircraft CG due to the one engine inoperative condition is

$$\mathcal{N}_a = -\mathcal{T}_L y_T; \quad (2.34)$$

to restore equilibrium the rudder is deflected to produce an opposite moment

$$\mathcal{N}_a = \frac{1}{2} \rho v^2 S b (C_{n_0} + C_{n_\beta} \beta + C_{n_{\delta_a}} \delta_a + C_{n_{\delta_r}} \delta_r) \quad (2.35)$$

where C_{n_0} is the constant yawing moment coefficient, C_{n_β} is the yawing moment

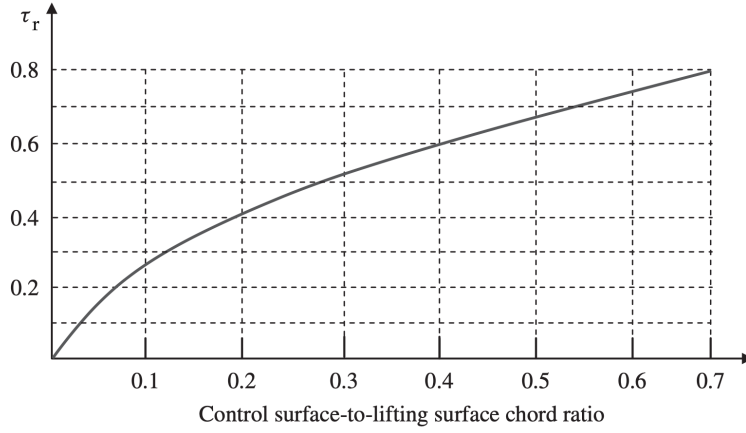


Figure 2.12: Moving surfaces effectiveness parameter as function of the moving surface on main surface chord ratio. Source [22].

coefficient derivative with respect to the sideslip angle β , $C_{n_{\delta_a}}$ the yawing moment coefficient derivative with respect to aileron deflection δ_a and $C_{n_{\delta_r}}$ the yawing moment coefficient derivative with respect to rudder deflection δ_r . Some simplifying assumptions are made: the aircraft is assumed to be symmetric about xz plane so $C_{n_0} = 0$, the aircraft is flying with no sideslip so $\beta = 0$ and there is no aileron deflection so $\delta_a = 0$. Equation (2.35) can be manipulated to give

$$C_{n_{\delta_r}} = \frac{\mathcal{N}_a}{\frac{1}{2}\rho v^2 S b} \frac{1}{\delta_r}. \quad (2.36)$$

The rudder control derivative $C_{n_{\delta_r}}$ can also be written as function of the tail parameters:

$$C_{n_{\delta_r}} = -C_{L_{\alpha}^v} V_v \gamma \tau_r \frac{b_r}{b_v} \quad (2.37)$$

with $C_{L_{\alpha}^v}$ vertical tail lift curve slope; since the vertical tail and the horizontal tail share the same airfoil, $C_{L_{\alpha}^v}$ has the same value of $C_{L_{\alpha}^h}$ computed with equation (2.22). The variable τ_r is the rudder effectiveness parameter related to the chords ratio by the curve in Figure 2.12 from [22]. Figure 2.12 can be used to compute the value of $\frac{MAC_r}{MAC_v}$, which results to be 0.17.

The computed value of $C_{n_{\delta_r}}$ will be used in the sizing procedure of the ruddervators of the V tail. As for the rudder the parameters to be computed are ruddervator span, chord and maximum positive and negative deflections. The sizing procedure adopted is from [49]; as for the rudder the chord ratio is computed using the ruddervator effectiveness parameter τ_{re} . Since a ruddervator serves both as rudder and as elevator, two values of τ_{re} are computed. One is considering it as rudder and the other considering it as elevator. The largest among these two

values will be selected since it satisfies both requirements on rudder action and on elevator action. The equations of τ_{re} are

$$\tau_{re} = \frac{-C_{m\delta_e}}{\gamma \frac{l}{MAC} C_{L\alpha}^N \sigma \cos \Gamma} \quad (2.38)$$

and

$$\tau_{re} = \frac{-C_{n\delta_r}}{\gamma \frac{l}{b} C_{L\alpha}^N \sigma \sin \Gamma}, \quad (2.39)$$

taken from [49] and based on experimental results in [50] and [51]. γ is the ratio between dynamic pressures defined in equation (2.18), l is the distance between tail aerodynamic center and aircraft CG, $C_{L\alpha}^N$ is the lift curve slope of the tail at zero dihedral, computed with data in [50] and σ the surface ratio between tail and wing, *i.e.*, $\frac{S_{vt}}{S}$. The only missing parameter is $C_{m\delta_e}$ since the U tail elevator has not been designed yet. A typical value is selected from [22], namely $C_{m\delta_e} = -0.3$ 1/rad. The obtained τ_{re} value allows to find $\frac{MAC_r}{MAC_{vt}}$ using the experimental curve in [52]; the resulting value is 0.25. The value of $\frac{b_r}{b_{vt}}$ is set to 0.8 (inside the typical range suggested in [22]); the maximum deflections are $\delta_r^{max+} = 30^\circ$ and $\delta_r^{max-} = -30^\circ$ as for the U tail rudder.

The designed moving surfaces are added to the XFLR5 model and an analysis is set up with the following conditions:

- $\rho = 1.197$ kg/m³,
- $v = 15$ m/s,
- $\beta = 0^\circ$,
- $W_{TO} = 4.4$ kg_f,
- $\delta_r = 10^\circ$,
- right turn.

The same analysis is performed both on the U tail and the V tail model. The results are summarized in Table 2.3. The yawing moment generated is similar, as expected since the control derivatives and tail volumes of both options are the same (mind that the tails have been designed to produce the same effects). The side forces on the U tail are smaller than the one of the V tail. It is important to state that the magnitude of the lateral forces is reasonably small, even if applying a scale factor to consider that the simulation are not performed at the maximum

²The value of δ_r is less than the maximum due to a convergence problem in XFLR5 for large deflection angles. A scale factor will be applied to the results to achieve an estimate of the loads in case of larger δ_r .

	U tail	V tail
Left surface lateral force magnitude [N]	0.38	1.54
Right surface lateral force magnitude [N]	0.55	1.17
Yawing moment magnitude [Nm]	1.13	1.44
Neutral point position after wing leading edge [cm]	13	10

Table 2.3: U tail and V tail results of the XFLR5 simulations.

control deflection. There is a significant difference in the tail forces, however they are small in both cases so it can be stated that there is no concern about the structural integrity since rigid carbon fiber booms will be used. Care will be applied to design the junctions between the tail booms and the fuselage.

Considering the longitudinal static stability it can be seen in Table 2.3 that, as stated in [22], the V tail has a neutral point which is closer to the nose of the aircraft with respect to the U tail and this may lead to reduced static stability or to instability. The neutral point position alone is useless because longitudinal static stability is evaluated considering the distance between neutral point and aircraft CG. Up to now it is not possible to make a final decision between V tail and U tail; it is necessary to wait until a value of CG position is available (after Chapter 4, once the fuselage has been designed and the internal components selected). To draw a temporary conclusion, the structural concern is solved while the longitudinal static stability is still unsolved.

2.6 Wing and tail design summary

This section is devoted to the summary of wing and tail parameters. Before presenting them in some tables, there is one last wing parameter to be determined: the taper ratio λ . As mentioned in Section 2.2, it is selected based on wing lift and induced drag distributions. These distributions are computed with XFLR5 in the V tail case; Figure 2.13 shows the lift coefficient and the induced drag distributions along the wing span. The focus to select λ is on the distributions shape, not on the values of the coefficients. The taper ratio, as reported in every aircraft aerodynamic/design text, is used to make the lift distribution elliptical so that induced drag is reduced. Considering Figure 2.13, the selected value of taper ratio is 0.8 since it is the value which reduces induced drag without increasing too much the lift at wing tip (a larger tip lift causes a higher bending moment at the wing root). Once the taper ratio is selected, it is straightforward to compute root and tip chord; their values are presented in Table 2.4, Table 2.5 and Table 2.6 along with all the other parameters of lifting surfaces.

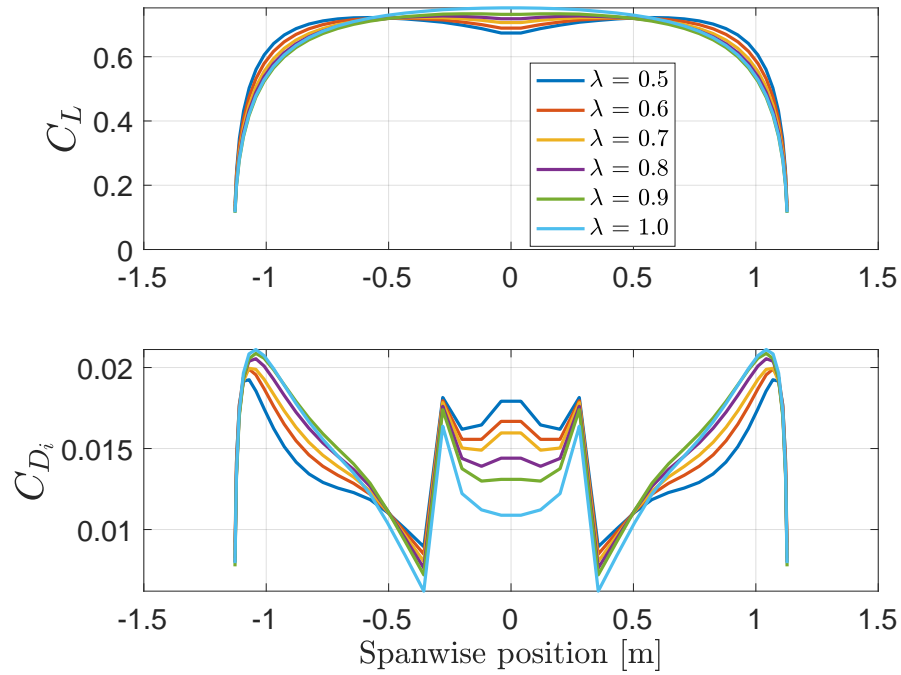


Figure 2.13: Lift coefficient and induced drag distributions along the span of the main wing; results from XFLR5 simulations.

Parameter	Value
Vertical position	high
Airfoil	Selig 2046
Incidence i_w [deg]	4
Sweep angle Λ [deg]	0
Dihedral angle Γ [deg]	0
AR	10
Taper ratio λ	0.8
MAC [cm]	23
b [cm]	225
S [m ²]	0.5
C_{root} [cm]	25
C_{tip} [cm]	20

Table 2.4: Wing parameters summary.

Parameter	Value
Tail arm l_{opt} [cm]	125
Horizontal surface S_h [m ²]	0.05
Vertical surface S_v [m ²]	0.01
Horizontal span b_h [cm]	63
Vertical span b_v [cm]	14
Airfoil	NACA 0008
AR_h	6.7
AR_v	2.0
Horizontal chord MAC_h [cm]	10
Vertical chord MAC_v [cm]	10
Horizontal tail incidence i_h [deg]	3

Table 2.5: U tail parameters summary. The data of the vertical tail are related only to one part, so the overall surface is twice the value presented.

Parameter	Value
Tail arm l_{opt} [cm]	103
Surface S_{vt} [m ²]	0.03
Dihedral angle Γ [deg]	31
Span b_{vt} [cm]	33
MAC_{vt} [cm]	9
Airfoil	NACA 0008
AR_{vt}	3.3

Table 2.6: V tail parameters summary. The data are related only to one part, so the overall surface is twice the value presented.

Chapter 3

Structural design

This chapter presents the structural design of the VTOL UAV. The objective of the structure is to support the loads to which the aircraft is subject during the operative life so that it can fulfill its mission. Moreover, the structural mass has to be minimized to reduce the lift that has to be generated to fly. This chapter is devoted to the structural design of the wing and tail designed in Chapter 2. The fuselage is dealt with in Chapter 4.

The first section of the chapter shows the flight envelope of the UAV used to identify the most demanding load condition, the second explains the selected structural layout and the last one presents the structural analysis of the wing spar. Practical aspects such as manufacturability and costs are taken into account in the design process.

3.1 v - n diagram

The first step in designing the structure is to identify the loads it has to bear. This is done, as suggested in [16], [21] and [23], through the maneuvering diagram and the gust load diagram. An example of them can be seen in Figure 3.1. The maneuvering diagram presents the flight envelope in which the UAV can fly safely. The gust diagram superimposed (in Figure 3.1 the straight dashed lines labelled as *Gust*) presents the load conditions that can derive from a gust. The result of the superposition of the maneuvering and gust diagrams is called v - n diagram since it presents the load condition in terms of load factor n as function of the airspeed v .

To build the v - n diagram for this VTOL UAV some references are considered: [23] for the operative procedure, [16] and [53] for reference values of similar UAVs, [19] for regulation requirements. A note has to be made about this last reference, the NATO Standard AEP-83 regulation: the European Union regulations applicable to the current UAV are [17] and [18] but they give no particular structural requirement; it has been therefore decided to consider [19] even if it is related to

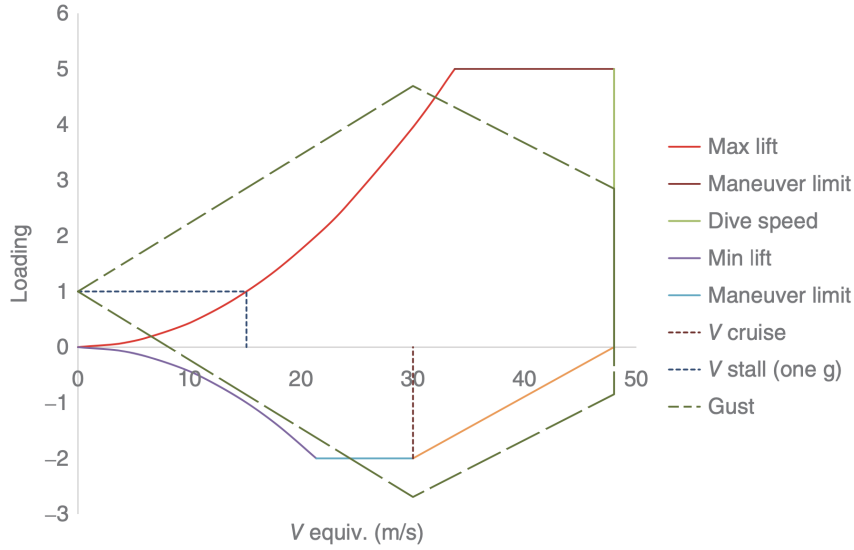


Figure 3.1: Typical diagram for maneuvering and gust loads of a small UAV; source [16].

Source	n_{max}	n_{min}
[19]	at least 3.8	at least -1.5
[16]	between 4.0 and 5.0	between -1.5 and -2.0
[53]	6.0	-3.0

Table 3.1: Reference values for maximum and minimum load factors of the v - n diagram.

military UAVs of higher class since it presents some indications about structural requirements.

The practical steps to build the v - n diagram are presented in the following:

- list all regulation and customer requirements in terms of speeds and load factors. The maximum and minimum load factors, respectively n_{max} and n_{min} , have to be identified. As mentioned in the Introduction of the thesis, there is no particular customer requirement that can lead to a load factor requirement. Therefore it has been decided to collect information from similar aircraft ([16] and [53]) and from the NATO Standard AEP-83 regulation [19]. Table 3.1 presents a summary of the values. It has been decided to select $n_{max} = 3.8$ and $n_{min} = -1.5$ since they are the lowest values in Table 3.1 but, at the same time, allow a good maneuverability to the aircraft.
- Define the gust loads which the UAV has to withstand. Generally the gust is defined in terms of gust velocity. Adopting the notation of [23], two types

Source	U_1 [m/s]	U_2 [m/s]
[19]	15.2	7.6
[16]	9.1	4.6
[53]	15.2	7.6

Table 3.2: Reference values for gust loads of the v - n diagram. Reference [19] allows in some cases to consider only half the standard gust velocity, *i.e.*, $U_1 = 7.6$ m/s and $U_2 = 3.8$ m/s.

of gusts are defined: one up to the cruise speed, called U_1 , and the other up to the maximum speed, called U_2 . The definition of U_1 and U_2 is based on the regulations since they present typical gust values based on atmospheric models. In the case at hand, also the values adopted in the structural design of similar UAVs are considered ([16] and [53]) since the regulation values are referred to larger aircraft that fly at higher altitude and in different conditions. Table 3.2 presents a summary of values from the same sources of load factors. As it can be seen from Table 3.2, the minimum gust velocities are from [16]; they have been used in UAVs of a similar scale of the VTOL UAV while the ones from [53] and [19] are intended for larger aircraft ([53] refers to FAR-23 for its structural requirements). Given this, the selected values are $U_1 = 9.1$ m/s and $U_2 = 4.6$ m/s from [16].

- Build the maneuvering diagram starting from the load factors identified at the previous point and the speeds of the aircraft. The starting point of the maneuvering diagram is the one of coordinates $n = 1$ and airspeed equal to the stall speed v_s , labelled A in Figure 3.2. From this point the stall curve at increasing load factor is drawn up to the maximum load factor n_{max} . This curve represents the aerodynamic limitation of the flight envelope (for positive load factors). The first point of this curve to reach n_{max} has airspeed $v_A = \sqrt{n_{max}}v_s$, called corner speed or maneuvering speed for its position in the maneuvering diagram. This point is called B in Figure 3.2. The equation of the maneuvering speed is obtained from the vertical equilibrium in maneuvering conditions at n_{max} and maximum lift coefficient

$$n_{max}W_{TO} = \frac{1}{2}\rho v_A^2 S C_{L_{max}}, \quad (3.1)$$

which can be easily rearranged as

$$v_A = \sqrt{\frac{2n_{max}W_{TO}}{\rho S C_{L_{max}}}} = \sqrt{n_{max}}v_s. \quad (3.2)$$

This speed is the minimum speed at which n_{max} can be reached. The structural limitation is represented by a straight line at the maximum load factor which goes from the corner speed to the maximum speed (in Figure 3.2 it is the segment B - C). The vertical line C - D at maximum speed is the graphical representation of the propulsive limitation. The same lines are drawn in the negative load factor part of the plane (segments D - E, E - F, F - G).

Three important airspeeds are highlighted with vertical lines: the stall speed, the cruise speed and the dive speed. This last speed has been selected to be higher than the maximum speed v_{max} used in the preliminary sizing in Chapter 1: it is $1.1 \times v_{max} = 24$ m/s. This choice has been made to extend the UAV flight envelope so that n_{min} can be reached. This forward shift of the propulsive limitation can be done considering that the selected engines for FF can deliver the required amount of power (the choice of the motors is presented in Chapter 4).

One last notice has to be done considering Figure 3.2: in general the cruise speed v_{cr} is larger than the maneuvering speed so that at cruise speed the aircraft can reach the maximum load factor to maneuver. In the case of this VTOL UAV, the cruise speed is below the corner speed, so at v_{cr} the aircraft cannot reach n_{max} and it has to speed up to v_a before reaching it. This is a peculiarity of this type of vehicles since also the competitors (whose speeds are presented in Table 1.3) present it: the maneuvering speed is $v_A = \sqrt{n_{max}v_s}$ and, assuming $n_{max} = 3.8$ also for them, it can be seen that most of them present a value of v_A higher than their cruise speed v_{cr} .

- The next step is to build the gust diagram and superimpose it to the maneuvering one to obtain the complete v - n diagram. Reference [23] presents the adopted method. As this reference states, the aviation authorities allow to reduce the gust loads due to the fact that generally the gust follows a sinusoidal shape, *i.e.*, it gradually rises to its maximum value. To account for this fact, a gust alleviation factor K_g is computed as

$$K_g = \frac{0.88\mu_g}{5.33 + \mu_g} \quad (3.3)$$

where μ_g is the aircraft mass ratio defined as

$$\mu_g = \frac{2 \frac{W_{TO}}{S}}{\rho MAC C_{L\alpha} g}, \quad (3.4)$$

g is the gravity field intensity and both MAC and $C_{L\alpha}$ are the ones of the wing. The intensity of the gust load in terms of load factor n_g is computed

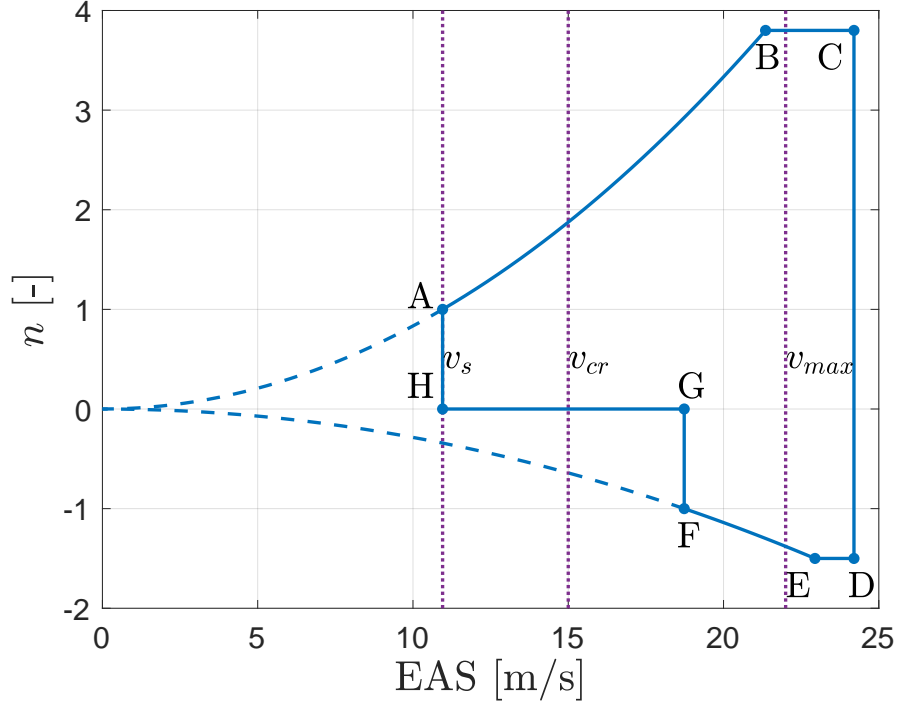


Figure 3.2: Maneuvering diagram for the VTOL UAV.

as

$$n_{g_1}(v) = 1 + \frac{1}{2} \frac{\rho K_g U_1 v C_{L\alpha}}{\frac{W_{TQ}}{S}} \quad (3.5)$$

and

$$n_{g_2}(v) = 1 + \frac{1}{2} \frac{\rho K_g U_2 v C_{L\alpha}}{\frac{W_{TQ}}{S}}. \quad (3.6)$$

The resulting gust loads are linear functions of the airspeed v . The gust load diagram can be seen in Figure 3.3 directly superimposed to the maneuvering diagram. Observing the complete v - n diagram of Figure 3.3 it can be seen that the gust loads with $U_1 = 9.1$ m/s are well outside the flight envelope and do not intersect it. Due to this fact it has been decided to design the structure so that it can withstand only gust loads with $U_2 = 4.6$ m/s.

Once the procedure has been completed and the v - n diagram is ready, it is possible to identify the sizing condition: the point characterized by the higher load factor is the most demanding condition from a structural point of view. Considering Figure 3.3, given that the higher gust loads have been discarded to avoid stretching the flight envelope, the higher load factor is $n = n_{max} = 3.8$. This will be the sizing condition for the structure.

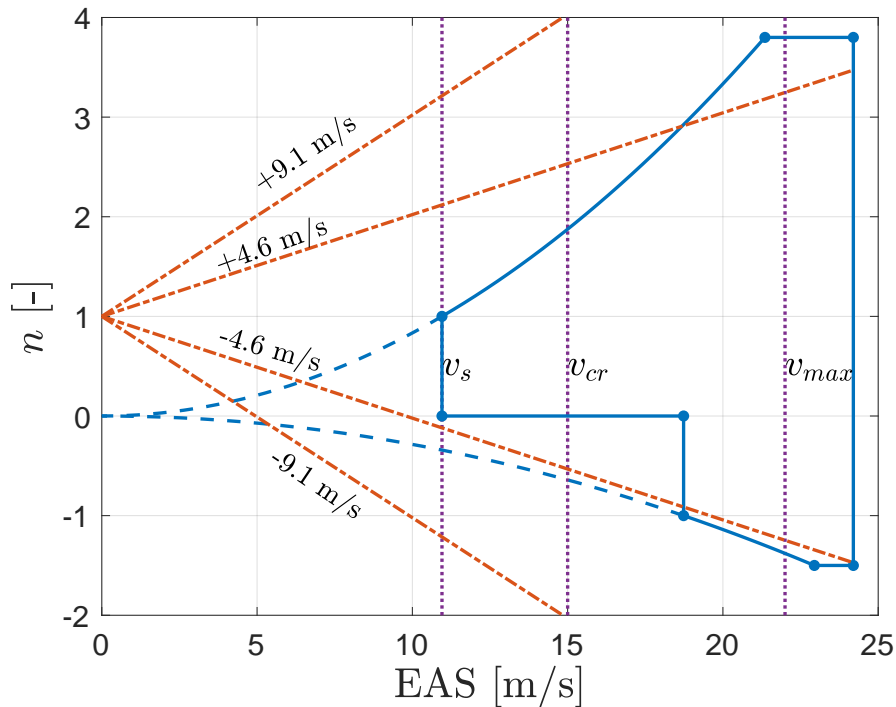


Figure 3.3: v - n diagram for the VTOL UAV; it is the superposition of the maneuvering diagram (solid blue lines) and of the gust diagram (red dash-dot lines).

3.2 Wing structural layout

The wing has been designed from an aerodynamic point of view in Chapter 2. It is now time to design the structure that composes this aerodynamic shape and, in case, to make some changes to ensure the structural integrity. To identify the structural layout means to select the materials and the shapes that can support the sizing loading condition identified in Section 3.1. As done also for the general UAV configuration, a literature survey is performed as first thing.

An important source has been reference [16] since it presents the design and construction of small unmanned fixed wing aircraft. Moreover, these UAVs are developed and manufactured by a university so the means (both practical and economical) are more or less the same as the one of the Department of Aerospace Science and Technology (DAER) of Politecnico di Milano. This reference has been a great source of inspiration for this VTOL UAV. The structural layout in Figure 3.4 is derived from this source. It is made up of mixed materials:

- carbon fiber tubes for the spars;
- hot wire cut foam for the aerodynamic shape;
- Mylar cladding to protect the foam during ground handling;

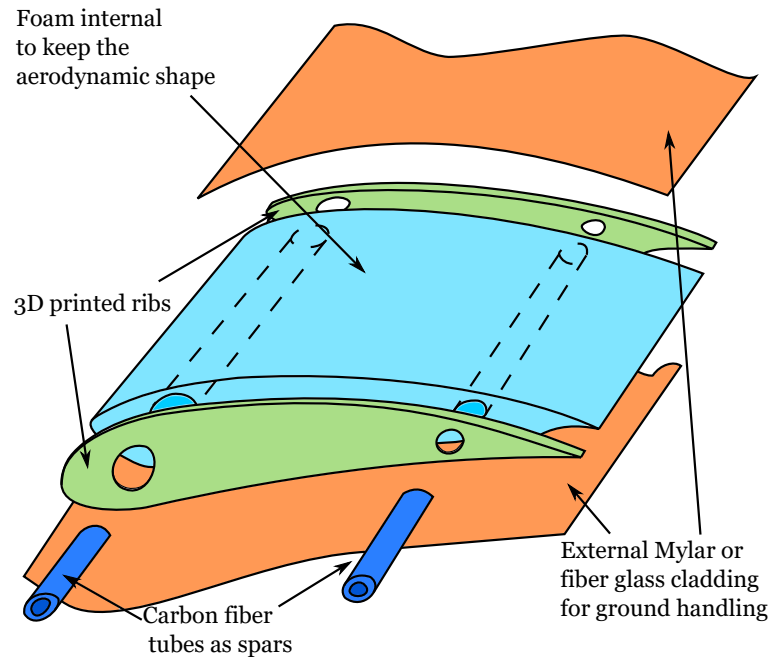


Figure 3.4: Mixed structural layout inspired by the UAVs of Southampton University [16]. The colors of the components are deliberately not real to better recognize the different elements.

- 3D printed ribs to transfer loads to the spar and to connect the foam blocks.

This structural layout is the last step of an evolution through several structural layouts adopted by Southampton University in the projects presented in [16]. Therefore, it can be considered a mature option. It has the pro of being economic and lightweight, with off-the-shelf components like the carbon fiber tubes for the spar and easy to produce components such as the hot wire cut foam elements and the 3D printed ribs. Several 3D printing technologies can be adopted: fused deposition modeling (FDM), which uses ABS or PLA filaments, or selective laser sintering (SLS) of nylon powder. A presentation of these two additive manufacturing technologies can be found in Appendix C. It is important to state that this layout can be easily produced inside the laboratories of Politecnico di Milano.

The second option is a conventional structural layout made up of composite materials in a semi-monocoque scheme, as suggested in [21] and adopted in [53]. A picture of this layout is in Figure 3.5. This layout is composed of:

- one or two composite spars to bear the loads. The section shape can be circular, C shape or H shape based on the type of the main load. Some spar sections are presented in Figure 3.6;
- composite ribs to keep the aerodynamic shape and transfer the loads from the skin to the spar;

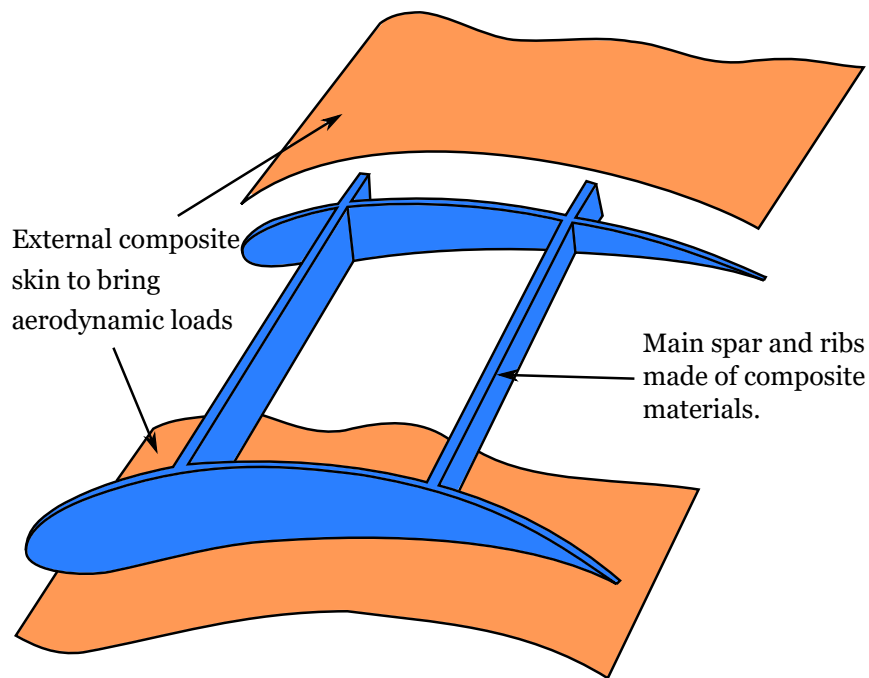


Figure 3.5: Composite structural layout with semi-monocoque scheme. The same consideration about colors made for Figure 3.4 applies here.

- composite skin to close the wing box and bear the aerodynamic pressure.

The pro of this structure is that it has been employed long since on lots of aircraft, so it is well studied and can be easily optimized to reduce the structural weight. Furthermore, the high structural performance of the composite materials allows to produce a lightweight structure. This type of structure can be considered long lasting and damage tolerant. This structural layout, although Politecnico di Milano has its own composite material laboratories, probably has to be outsourced given its dimensions and complexity. It is also significantly more expensive to produce, given the need for custom molds.

Each one of the two layouts proposed offers some pros and some cons. Cost and practical aspects are pivotal in the choice of the one to be adopted. The first layout, even if it seems a bit artisanal, is considered the best option since it is relatively simple to be produced. Moreover, several real UAV models have been built with this technique and used in real life missions by Southampton University. It has to be acknowledged that wing and tail can be disassembled and changed, so in the future the actual layout can be replaced by something different (for example

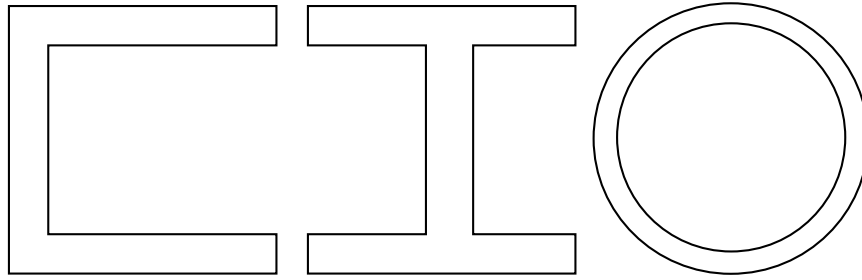


Figure 3.6: Possible spar sections for the semi-monocoque structural layout.

the second proposed layout). For all these motivations, the first structural layout is selected. The structural layout in Figure 3.4 can be adopted also on the tail.

Now a more in depth presentation of the selected structural layout is done. Since the wing and tail structures have small chord, reference [21] suggests to adopt only one spar. It will be placed at the quarter of chord location and the moving surfaces hinges (both on the wing and on the tail) will be attached to the ribs. In the case of the wing a circular section carbon fiber tube with inner diameter of 14 mm and outer diameter of 16 mm will be used. For the tail a carbon fiber tube with inner diameter 4 mm and outer diameter 6 mm is selected. This choice is made considering the maximum thickness of the wing and tail airfoils determined in Chapter 2. The ribs will be printed in FDM ABS since, at the moment, only this technology is available in the DAER facility (SLS components have to be outsourced). In the case of the wing, the ribs have a thickness of 5 mm; their disposition is:

- one at the root to connect wing and fuselage,
- one at the wing tip to conclude the wing and attach the aileron hinge,
- one at the aileron inboard position to attach the other hinge,
- one in the middle between root and aileron inboard position.

A drawing of the wing structure is presented in Figure 3.7.

In the case of the tail, the rib disposition and thickness depend on the tail configuration adopted. In any case, given the dimensions of the tails only two ribs will be used: one at the tip and one at the root to attach the moving surfaces hinges. Their thickness will be similar to the wing ribs one.

3.3 Wing spar structural analysis

The last step in the structural design of wing and tail is the structural analysis in the load condition determined in Section 3.1. The objective is to verify that

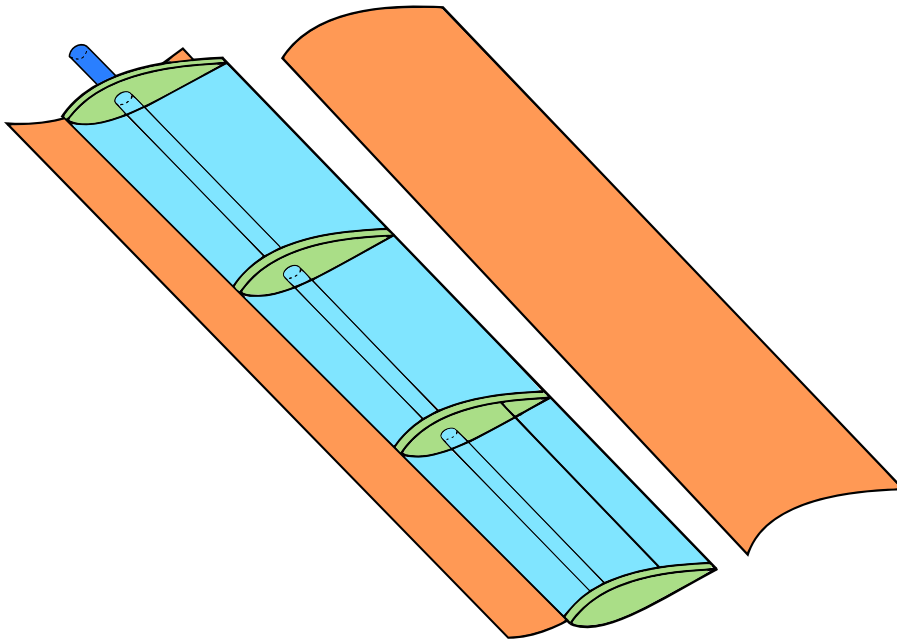


Figure 3.7: Semi-wing structural layout overview.

the structural elements detailed in Section 3.2 can withstand these loads. A decision has been taken to simplify this analysis: only the wing is checked, the tail components are sized with a margin to ensure structural survivability. As it has been highlighted in Section 2.5, the tail is subject to small forces so the use of carbon fiber tubes with 2 mm thickness (same as for the wing) to build the spars is considered warranty of structural integrity.

The main structural element of the wing is the spar: the foam is used to obtain the required airfoil section and the ribs connect the foam blocks together and with the spar. It is easy to model the wing spar as an Euler-Bernoulli beam with uniform properties along its axis. Since the wing is a symmetric structure loaded in a symmetric way, only half structure is considered. Given this, the structural analysis is performed on one semi-wing encastred at the root. The section properties are computed with the formulation proposed in [16] but they can be recovered from any structural mechanics textbook. For a hollow cylinder with outer diameter d and thickness t , the second moment of area I is

$$I = \frac{\pi(d^4 - (d - 2t)^4)}{64}. \quad (3.7)$$

For the considered tube for the wing spar, with $d = 16$ mm and $t = 2$ mm, equation (3.7) gives $I = 2200$ mm⁴. This value is used to compute the bending

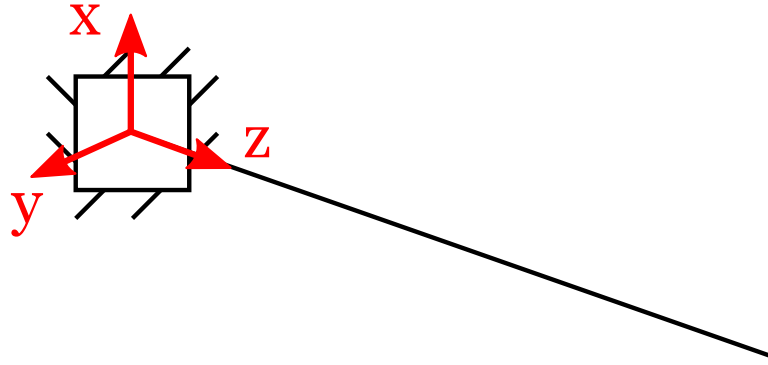


Figure 3.8: Beam reference frame for stress computation.

stress $\sigma_{bending}$ as

$$\sigma_{bending} = \frac{M_{yy}(z)\bar{x}}{I} \quad (3.8)$$

with $M_{yy}(z)$ bending moment around the beam y axis at the coordinate z and \bar{x} maximum distance from the beam axis z . The beam reference system is presented in Figure 3.8 for an immediate understanding. In this case \bar{x} is the section radius, *i.e.*, 8 mm.

The only unknown element, up to now, is the bending moment $M_{yy}(z)$. For a first rough calculation the beam is considered under a uniform distributed load w equal to

$$w = \frac{n_{max}W_{TO}}{b} \quad (3.9)$$

with b wing span. This load is equal to the lift required to reach equilibrium in a maneuver at the maximum load factor n_{max} identified in Section 3.1. In the case of a uniformly distributed load w , the bending moment is

$$M_{yy}(z) = \frac{w(j^2 - 2jz + z^2)}{2} \quad (3.10)$$

with j beam length and z distance from the beam reference frame origin along the longitudinal axis. In this case $j = \frac{b}{2}$ (the analysis is on half of the wing) and $z = 0$ since the maximum bending moment is at the wing root. The result obtained from equation (3.10) is 41 Nm. With equation (3.8) it is possible to compute the bending stress, which is 150 MPa. Considering the typical values presented in [16] for the carbon fiber tube, the maximum admissible stress is $\sigma_{max} = 570$ MPa. As it can be seen, $\frac{\sigma_{bending}}{\sigma_{max}} \approx \frac{1}{4}$ so there is a large margin from the maximum stress.

It is interesting to check also the tip deflection δ_{tip} of the beam under the same distributed load w . The general equation for the deflection along the beam is

$$\delta(z) = \frac{wz^2(6j^2 - 4jz + z^2)}{24EI} \quad (3.11)$$

with E Young modulus of the carbon fiber tube. The value from reference [16] is 70 GPa. δ_{tip} is obtained setting $z = j$ in equation (3.11), so

$$\delta_{tip} = \frac{wj^4}{8EI}. \quad (3.12)$$

The obtained result is $\delta_{tip} = 9.5$ cm, which can be accepted without problems considering that each semi-wing is 112.5 cm long. Given the results of the computation, it can be stated that the carbon fiber tube for the wing spar can bear the flight loads. Moreover, there is a great margin from the maximum admissible stress. However, it has been decided to increase the detail of the analysis further using the aerodynamic loads computed with XFLR5. In fact, this load has the proper distribution and it is not uniform along the wing span. As previously done, only half of the wing is considered. It is discretized in 22 elements connected by 23 nodes. On each k -th element the distributed aerodynamic load is computed as

$$w^{(k)} = \frac{1}{2}\rho_{cr}n_{max}v_{cr}^2MAC\sqrt{\left(C_L^{(k)}\right)^2 + \left(C_D^{(k)}\right)^2} \quad (3.13)$$

with $C_L^{(k)}$ and $C_D^{(k)}$ lift coefficient and drag coefficient on the k -th element, respectively. As it can be seen from Figure 3.9, each k -th element of length $j^{(k)}$ is subject to its part of distributed aerodynamic load $w^{(k)}$, to the resultant of forces on the previous elements

$$\mathcal{P}^{(k)} = w^{(k)}j^{(k)} + \mathcal{P}^{(k-1)} \quad (3.14)$$

and to the resultant of moments on the previous elements

$$\mathcal{Q}^{(k)} = w^{(k)}\frac{\left(j^{(k)}\right)^2}{2} + \mathcal{P}^{(k-1)}j^{(k)} + \mathcal{Q}^{(k-1)}. \quad (3.15)$$

Computing the bending moment M_{yy} at the root is equivalent to evaluate equation (3.15) for $k = 22$. Being the wing tip free, $\mathcal{P}^{(1)} = 0$ and $\mathcal{Q}^{(1)} = 0$. The result substitution inside equation (3.8) allows to compute the stress due to bending at the root. It is obtained $\frac{\sigma_{bending}}{\sigma_{max}} \approx \frac{1}{5}$.

The deflection of each i -th element of length $j^{(i)}$ is

$$\delta^{(i)} = \delta_{bending}^{(i)} + \delta^{(i-1)} + \vartheta^{(i-1)}j^{(i)} \quad (3.16)$$

where $\delta_{bending}^{(i)}$ is the tip deflection due to the bending moment of the i -th element, $\delta^{(i-1)}$ is the deflection at the tip of the previous element and $\vartheta^{(i-1)}$ is the rotation

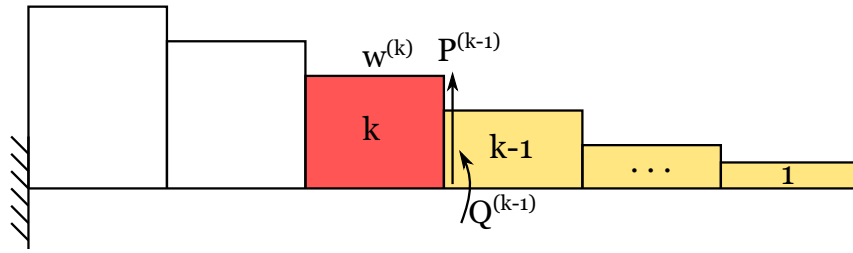


Figure 3.9: Forces acting on the k -th element of the beam, highlighted in red.

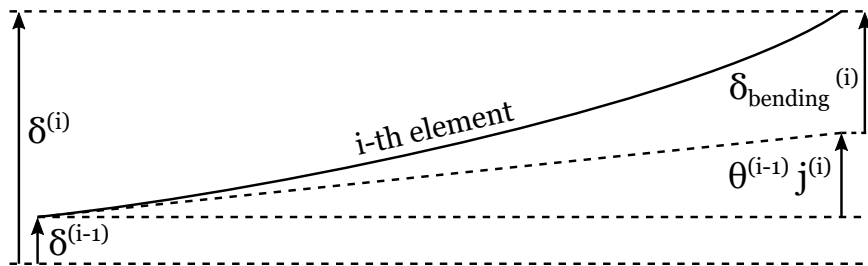


Figure 3.10: Deflection of the i -th element of the beam.

at the tip of the previous element. A graphical representation is shown in Figure 3.10. The tip deflection due to the bending moment is

$$\delta_{bending}^{(i)} = \frac{w^{(i)}(j^{(i)})^4}{8EI} + \frac{\mathcal{P}(j^{(i)})^3}{3EI} + \frac{\mathcal{Q}(j^{(i)})^2}{2EI} \quad (3.17)$$

while the rotation on each i -th element is computed as

$$\vartheta^{(i)} = \frac{w^{(i)}(j^{(i)})^3}{6EI} + \frac{\mathcal{P}(j^{(i)})^2}{2EI} + \frac{\mathcal{Q}j^{(i)}}{EI}. \quad (3.18)$$

To compute the deflection at the tip it is necessary to start from the wing root: being encastred, the wing root has deflection $\delta^{(1)} = 0$ and rotation $\vartheta^{(1)} = 0$. Evaluating equation (3.16) for $i = 22$, the following result is obtained: $\delta_{tip} = 7$ cm. As it can be observed, both $\sigma_{bending}$ and δ_{tip} are smaller than the case of uniformly distributed load w . This is due to the fact that the load distribution is better approximated with a non uniform load, in fact the real aerodynamic load is smaller at the tip and larger at the root¹. Figure 3.11 shows the forces and moments acting on each of the 22 elements of the wing and the resulting deformation. It is possible to see, also, the global deformed shape of the wing (note that the y axes have different scales for each quantity).

¹A smaller tip load brings to a smaller tip deflection and root bending stress.

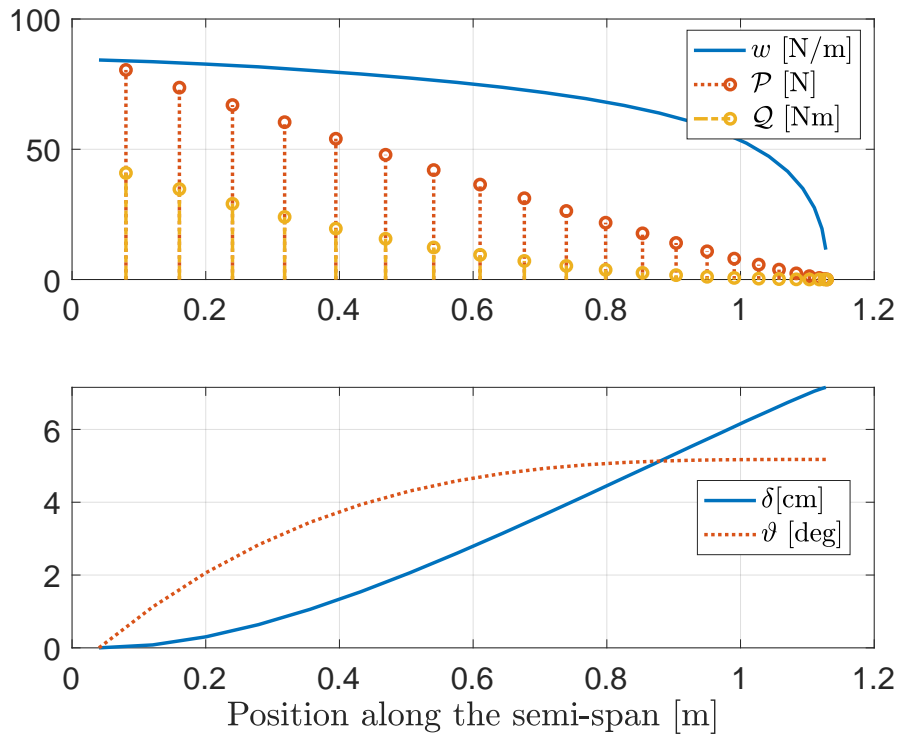


Figure 3.11: Results of beam analysis with loads from XFLR5.

Concluding the structural analysis of the wing spar, it has been verified that the selected carbon fiber tube with internal diameter 14 mm and outer diameter 16 mm is capable of sustaining the maximum flight loads with a large margin with respect to the maximum admissible stress. Considering that the tail spar tubes have equal thickness but have to bear lower loads, it is reasonable to neglect a structural analysis of the tail spars.

Chapter 4

Propulsion, onboard systems and fuselage design

This chapter completes the detail design started in Chapter 2 and continued in Chapter 3. In fact, all the remaining items of the UAV are designed: the motors, the battery, the avionics and the fuselage. Among the previous items, only the fuselage is custom-designed and produced. The motors, the avionics parts and the battery are off-the-shelf components. With the definition of these elements the detail design is almost finished, so the aircraft CG position can be estimated for the evaluation of the UAV longitudinal static stability (presented in Chapter 5). This chapter is organized in four sections, the first devoted to the engines selection, the second to the battery, the third to the avionics and the last one to the fuselage.

4.1 Electric motors selection

As decided in Chapter 1, this UAV is equipped with two separate sets of motors, one for vertical flight (VF) and one for forward flight (FF). The criteria with which they are selected are different: the VF engines sizing is performed considering the UAV as a rotorcraft, the FF engines sizing considering it as a conventional fixed-wing aircraft. Each electric engine needs its own electronic speed controller (ESC) and a propeller to work properly. Then, each propulsive unit to be selected is made up of these three elements: brushless motor, ESC and propeller. Before starting the selection of the engines from one of the numerous engine manufacturers, the number of VF and FF engines has to be decided.

4.1.1 Vertical flight electric motors

In the VF engines case an even number of motors has to be selected since the engines are installed on two separate booms. Figure 4.1 presents the possible

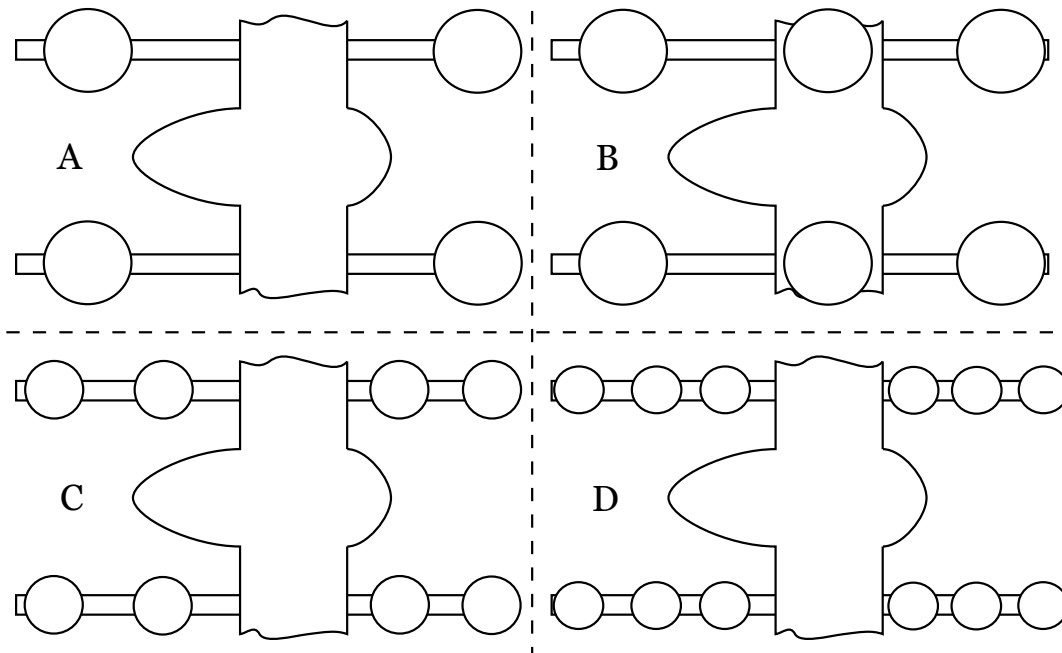


Figure 4.1: Considered options for the number of VF engines.

options:

- **option A:** 4 VF motors,
- **option B:** 6 VF motors,
- **option C:** 8 VF motors,
- **option D:** 12 VF motors.

Option B is discarded since it is difficult to position the motors: one ahead of the wing, one behind and the third? Figure 4.2 presents the possible options. Installing it on one side or the other of the wing brings to an asymmetric thrust with respect to the wing axis. Installing it inside the wing to prevent asymmetric thrust messes up the wing aerodynamics. For this reason option B is discarded. Also option D is discarded to keep the number of components limited: less motors means reduced possibilities of faults.

Fault tolerance aspects have to be considered in the choice between option A and option C. In this thesis this aspect has not been investigated in detail and it is source of a possible future work; only basic considerations have been done. Generally, when there is an engine fault the way to keep the rotorcraft flying is to produce the required amount of thrust keeping moment equilibria around all the three axes. In some cases, to achieve this result, one or more engines are stopped. A simple consideration can be made: in the case of a VF engine fault, option C

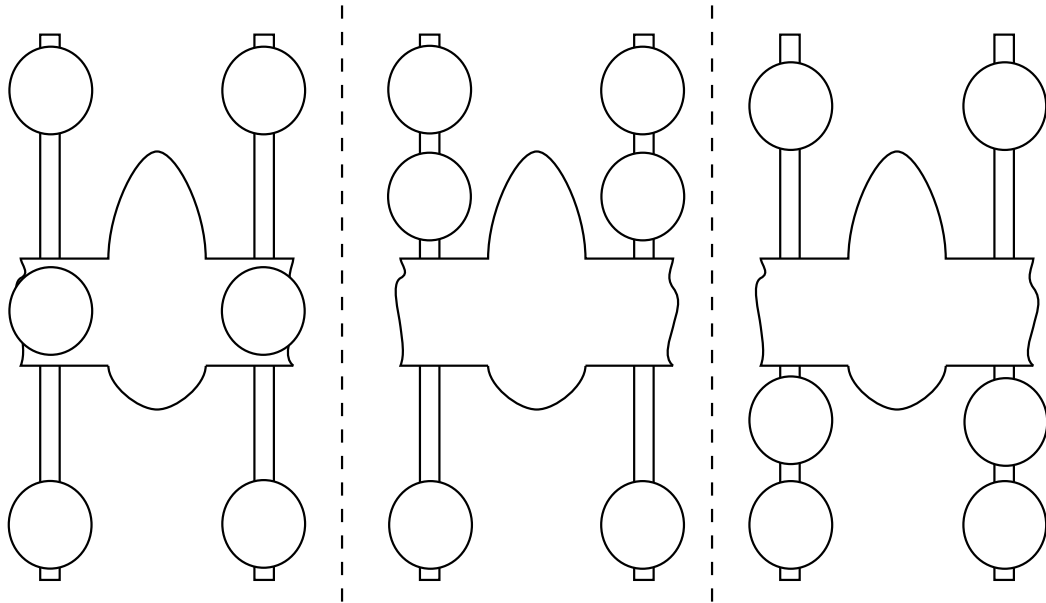


Figure 4.2: Six VF engines configuration, different positions of the central motor.

can be reconfigured to achieve moment equilibria around all the axes and vertical forces equilibrium, while this is not possible in the case of option A. Based on this simple consideration, option A is discarded and it is decided to install 8 VF engines.

As already mentioned, the UAV works as a rotorcraft when the VF engines are operative. The control action is performed producing a different thrust with each motor; in this way moments around the three aircraft axis are generated. An electric motor produces its thrust based on the throttle input: the thrust increases for increasing throttle percentage. To ensure a thrust margin for control purposes, the thrust required in hovering (which is equal to the take-off weight W_{TO}) has to be generated at most at 50% of the throttle. As shown in Chapter 1, the maximum required power for VF engines is the climb power P_b^{cl} . To ensure the thrust control margin also in climb, the maximum power required to the engines has to be $1.3 \times P_b^{cl}$. Summarizing all this information and considering the preliminary sizing values of Table 1.6, it can be stated that the desired VF motor has

- to produce at least 600 g_f with at most 50% of throttle (hovering condition),
- to produce at least 850 W of power with maximum throttle (climb condition).

A broad range of engine manufacturers has been considered starting from the database of the website eCalc ([54]) used for the preliminary sizing of rotorcraft

UAVs and performance evaluation. A progressive selection has been performed: only the manufacturers with performance information as function of the throttle have been considered inside the complete eCalc database (5 out of 44). The selected manufacturers are: Dualsky Ltd. ([55]), KDE Direct ([56]), Scorpion Power System Limited ([57]), MAD Components ([58]) and T-MOTOR ([59]). The data of produced thrust and required power of an electric motor are related to the propeller to which the motor is connected and to the battery that powers it. Given that, the same motor can present different values of thrust and power based on the propeller and the battery with which it has been tested. A database of electric motors from the selected manufacturers has been set up collecting data about thrust at 50% of throttle, maximum required power, battery technology, cost and propeller. More than 150 electric motors have been considered for this database.

The propeller diameter has been a key factor in the choice of the VF engine: eight VF motors means four engines on each side, two ahead of the wing and two behind it. To keep the engine booms length reasonable, the propeller diameter has to be the smallest possible. Considering this, the engine database has been organized for increasing propeller diameter.

A series of filters have been applied to select the VF motor:

- propeller diameter below 10 inches,
- thrust at 50% of the throttle in the range 600 g_f and 800 g_f,
- increasing weight of the whole propulsive system: motor, ESC and propeller.

Downstream of this procedure, the selected engine has been the KDE Direct KDE2315XF - 2050 with propeller 5 × 4.5 bull nose (BN) and a 4S battery (*i.e.*, four cells connected in series with overall 14.8 V input voltage). The recommended ESC from the manufacturer is the model KDEXF - UAS55. Figure 4.3 shows the VF engine and Table 4.1 presents its performance. The overall weight of the propulsive system is 138 g_f for each one of the eight motors (1104 g_f globally).

Once the propeller diameter has been fixed, it is possible to choose the engine location along the booms. Figure 4.4 presents the disposition of the VF motors; this set up can be changed slightly if it is necessary to modify the aircraft CG position. The details of the engine - boom connection are shown in Chapter 5. Each ESC will be positioned next to the engine on the same frame. Considering the diameter and the number of power and signal cables to be connected to the engine, it has been decided to use carbon fiber tubes with inner diameter of 16 mm and outer diameter of 18 mm as motor booms. These tubes are used for both front and rear engines.



Figure 4.3: Selected engine: KDE Direct KDE2315XF - 2050, source [56].

Voltage [V]	Propeller	Throttle [%]	Power input [W]	Thrust output [g _f]
14.8 (4S)	5 × 4.5 BN	25.0	81	310
		37.5	145	470
		50.0	210	610
		62.5	268	730
		75.0	327	840
		87.5	427	1030
		100.0	580	1250

Table 4.1: Selected VF engine performance as function of the throttle percentage. Data from the manufacturer website [56].

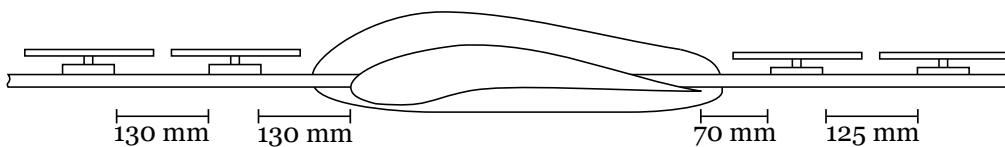


Figure 4.4: Vertical motors position along the booms.

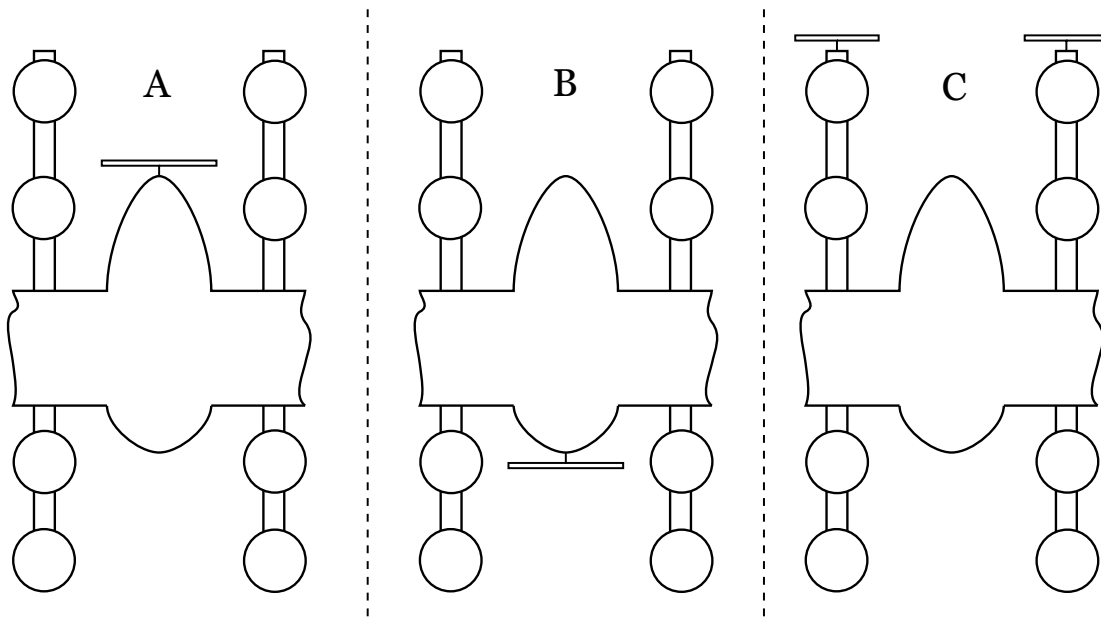


Figure 4.5: Considered options for the number of FF engines.

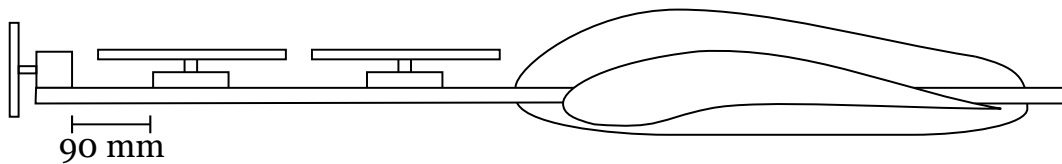


Figure 4.6: FF engine position on the forward booms.

4.1.2 Horizontal flight electric motors

As for the VF engines, the first step to select the FF propulsive system is to choose the number of motors. Three main options are available:

- **option A:** single engine in tractor configuration inside the fuselage,
- **option B:** single engine in pusher configuration inside the fuselage,
- **option C:** multiple engines on the wing or on the booms.

Figure 4.5 presents the three options. It has been decided to use multiple engines for redundancy in the FF propulsive system, so option C is selected. To limit the number of engines and make a smart use of already available components, it has been decided to install only two FF engines on the tip of the front VF engine booms, as shown in Figure 4.6. Each FF motor is at 90 mm from the first VF engine. The detailed FF engine - boom connection is shown in Chapter 5.

The requirement for the FF motors is on maximum power; the value of P_b^{FF} is taken from the preliminary design of Chapter 1: $P_b^{FF} = 135$ W. This is equivalent, more or less, to a maximum output power of 70 W for each engine. The output power is a fraction of the input power; it is reasonable to assume $\frac{P_{output}}{P_{input}} \approx 0.75$, so each engine has to be powered with at least 87 W (the manufacturers give the input power data, not the output one). Some manufactures state that the maximum indicated power can be kept only for few seconds. The maximum power required for flight, however, has to be produced for a continued period of time. To take into consideration this fact, the required power input of 87 W at least has to be the value at 75% of throttle. In this way it is a continuous power and not a peak power.

In the case of FF motors a broader range of engines is considered (more or less 200) since some manufacturers, even if they do not provide performance data as function of throttle, provide information about maximum continuous power. The manufacturers considered are: Dualsky Ltd. ([55]), KDE Direct ([56]), Scorpion Power System Limited ([57]), T-MOTOR ([59]) and Innov8tive Designs, Inc. ([60]). To ensure compatibility with the battery of the VF engines, only motors powered by a 4S battery are considered. The following series of filters is applied to identify the FF engine:

- input power from a 4S battery (14.8 V),
- power input greater or equal to 87 W,
- increasing propeller diameter,
- increasing weight of the whole propulsive system: motor, ESC and propeller.

The selected motor is KDE Direct KDE2304XF - 2350 with 5×3 propeller; the ESC, from the same manufacturer, is the model KDEXF - UAS20LV. The overall weight of the FF propulsive system is 62 g for each one of the two motors (124 g globally). Figure 4.7 shows the FF motor while Table 4.2 presents its performance.

4.2 Battery

The battery is the power source of the UAV. As said in Chapter 1, LiPo batteries have been selected. The battery type stems from the motors chosen: both VF and FF engines have to be powered from a 4S battery to produce the same performance as the one declared from the manufacturer. The battery specifications adopted in the conceptual design are:

- energy density \bar{e} of 180 Wh/kg,



Figure 4.7: Selected engine: KDE Direct KDE2304XF - 2350, source [56].

Voltage [V]	Propeller	Throttle [%]	Power input [W]	Thrust output [g_f]
14.8 (4S)	5×3.0	25.0	27	170
		37.5	47	240
		50.0	69	300
		62.5	96	380
		75.0	132	480
		87.5	188	620
		100.0	249	750

Table 4.2: Selected FF engine performance as function of the throttle percentage. Data from the manufacturer website [56].

- power density p of 800 W/kg.

It is important to respect, if possible, the values adopted in the preliminary sizing. In this way the assumptions under which the preliminary results have been computed are respected. The required energy to complete the mission profile is $E_r = 88$ Wh. The manufacturers present the battery performance in terms of capacity C , which is defined as

$$C = \frac{E}{V} \quad (4.1)$$

with E battery energy and V battery voltage. $V = 14.8$ V for a 4S battery; the required capacity C_r is obtained from equation (4.1) with $E_r = 88$ Wh: $C_r = 5900$ mAh. To ensure a small margin the value is set to 6000 mAh. A database of 4S batteries with at least C_r is set up considering all the models available in the online shop HobbyKing ([61]) and from the manufacturer Gens Ace & Tattu ([62]), which is not sold on HobbyKing. The result is a database of 21 batteries. The specific energy \bar{e} , the specific power p , the capacity C , the energy E and the weight W_{batt} are collected for each model.

The selection of the battery is based on a series of filters applied to the database:

- current availability on the market,
- battery maximum power output greater or equal to 850 W (power required for vertical climb increased of a 30% to ensure control margin, as explained in Subsection 4.1.1),
- battery weight less or equal to 1500 g_f to respect the preliminary sizing results (see Table 1.6),
- energy density greater or equal to 180 Wh/kg and power density greater or equal to 800 W/kg to respect preliminary sizing input (see Table 1.2),
- increasing battery weight.

The result is a model sold by Gens Ace & Tattu with 8500 mAh capacity, a weight of 670 g_f and dimensions 155 mm × 48 mm × 43 mm. As it can be seen, the battery weight is less than half the W_{batt} obtained in the preliminary sizing due to the higher power density of the models on the market: the database mean value is seven times the one adopted in Chapter 1. This is due to the peculiarity of LiPo batteries which can achieve high power output. However, this power output can be sustained only for short time (in the case of the selected battery approximately 10 minutes). This aspect has to be investigated further in case of future electric aircraft sizing procedures.

4.3 Avionics

The avionics is made up of several components used to control and power the UAV and connect it to the ground operator. The selection of the avionics items has been performed together with Dr. Giurato and Dr. Panza to ensure full compatibility with the hardware and software already in use within the Aerospace Systems and Control Laboratory (ASCL). A list of the components and their function is presented in the following:

- **flight control unit (FCU)**; it is the main flight computer and runs the control algorithms of the aircraft. The model selected is the Pixhawk 4 by Holybro ([63]), which runs the open source autopilot PX4 ([64]). It is equipped with its own processor, 3-axes accelerometers and gyroscopes, a magnetometer and a barometer. Pixhawk 4 has been selected since it the only available PX4-compatible hardware with more than 15 PWM outputs. In fact, PWM outputs are used to control the eight FF engines, the two VF motors and the moving surfaces servomotors¹. Pixhawk 4 by Holybro, shown in Figure 4.8a, has 16 PWM outputs.
- **Power module (PM)**; it is sold together with Pixhawk 4 and it is used to distribute power from the battery to all the components at the proper voltage and current values. Figure 4.8b shows the power module selected.
- **Telemetry module**; it is a radio telemetry module compatible with Pixhawk 4. It is used to transmit and receive telemetry information from the ground control station to the aircraft (and vice versa) when it flies outside the FlyART laboratory, *i.e.*, the indoor telemetry system cannot be used. This module can reach 300 m range “out of the box”, *i.e.*, the range can be extended with an antenna on the ground. The telemetry module installed on the UAV, made by Holybro, is shown in Figure 4.8c.
- **Receiver (RX)**; it is used to receive the control input from a remote controller used by the UAV operator. In this way it is possible to send set points to the UAV to perform the desired mission. It is important to have the possibility of manually controlling the UAV in case of problems during the mission. The model adopted is a FrSky X8R ([65]), shown in Figure 4.8d.
- **Companion computer (FCC)**; this small board is connected to the FCU and it is used for communications with the ground control station when the UAV is operated inside the laboratory. The model selected, shown in Figure 4.8e, is a NanoPi NEO Air-LTS by FriendlyElec ([66]). Moreover, it can be used to perform heavy CPU load operations that cannot be performed by the FCU, such as high level guidance and control laws.

¹In the case of V tail the servomotors are four, in case of the U tail the servomotors are five.

Component	Weight [g _f]	Dimensions [mm × mm × mm]
FCU	16	44 × 84 × 12
FCC	8	40 × 40 × 2
PM	40	65 × 50 × 10
BEC	11	54 × 25 × 11
RX	17	46 × 27 × 14
Telemetry module	30	48 × 28 × 11
Digital airspeed sensor	15	5 × 5 × 2
GPS	32	$\pi 25^2 \times 14$

Table 4.3: Weight and dimensions of the avionics components for the fuselage sizing.

- **Digital airspeed sensor**; this sensor is used to provide airspeed information to the FCU. It is made up by a Pitot tube to measure static and total pressure and by a transducer which transforms the pressure measurements in electrical signals sent to the FCU. The model selected, shown in Figure 4.8f, is made by Holybro.
- **GPS module**; this sensor is included with the selected FCU. It is useful since the UAV is intended for outdoor operations; the GPS module will be used to recover position information. Figure 4.9a shows the GPS module.
- **Battery elimination circuit (BEC)**; this device is a voltage regulator and it is used to convert the voltage output from the battery to a lower voltage. It is used to power the 5V electronics, such as the moving surfaces servomotors. Figure 4.9b shows the chosen BEC.

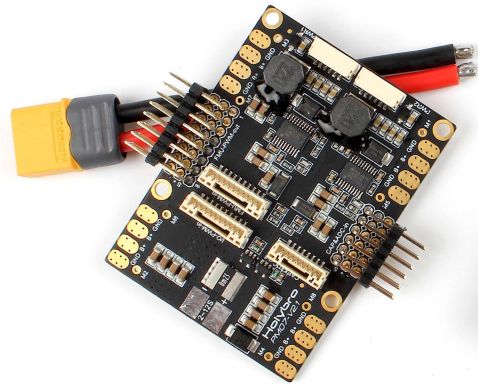
A summary of all the avionics and their specifications is done in Table 4.3. The weight and dimensions of each component are useful in the design of the fuselage presented in Section 4.4.

4.4 Fuselage design

The avionics components, the battery and the payload have to be hosted inside the fuselage. One possible method to design the fuselage, according to [23], is to place all the internal components to achieve the desired CG position, then to draw the best shape that contains them. In the case at hand one more thing has been taken into consideration: to make wing change easier, the motor booms have to be connected to the fuselage instead of to the wing. In this way, when a new wing is designed and attached to the fuselage there is no need to connect again all the booms and the engines to it. This simplifies and speeds up a lot the possibility



(a) Pixhawk 4 FCU, source [63].



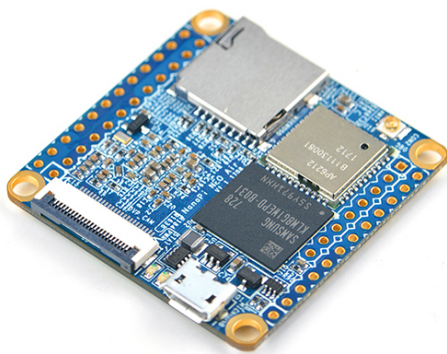
(b) Power module, source [63].



(c) Telemetry module, source [63].



(d) Receiver, source [65].



(e) Companion computer, source [66].



(f) Digital airspeed sensor, source [63].

Figure 4.8: Avionics components - part 1.

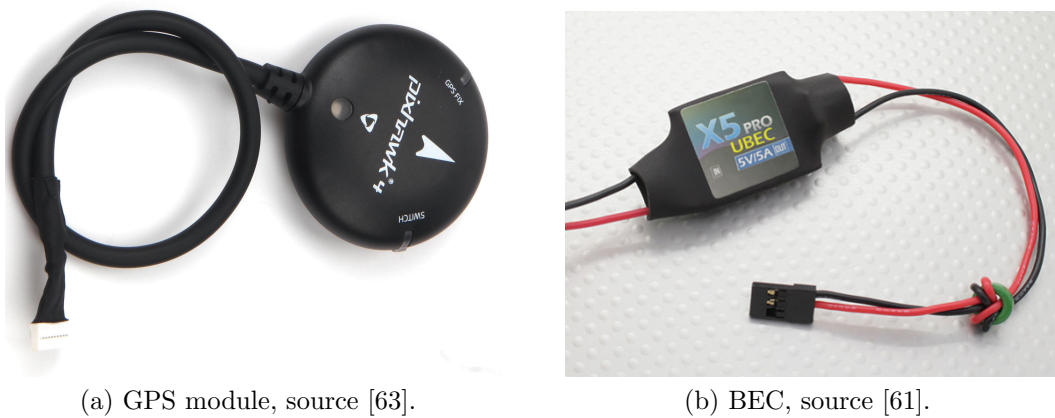


Figure 4.9: Avionics components - part 2.

of wing interchangeability. With this consideration in mind, taking inspiration from some competitors, it has been decided to collect all the internal components in the central part of the fuselage and to leave the lateral parts to the booms connections. Figure 4.10 shows a simple fuselage set up.

To make assembly and maintenance of avionics easier, it has been decided to collect most of the components on a base which is connected with screws to the fuselage. After a trial and error procedure, the final set up shown in Figure 4.11 has been achieved. This base for electronics will be 3D printed with FDM ABS inside the DAER laboratories. As it can be seen from Figure 4.11 there are holes for the screws and openings to connect the cables to the PM in an ordered way.

The disposition of the internal components is done around the wing spar positioned at the quarter of chord. In this way three positions are available, as shown in Figure 4.10:

- **position A:** rear location, behind the wing spar,
- **position B:** central location, in front of the wing spar,
- **position C:** front location, in the nose of the aircraft.

The first element to be positioned is the battery since it is the heaviest one: its position can affect the CG location more than the others. The best location for the battery is position B since it is in the center of the fuselage and, to first approximation, the aircraft CG is more or less in this part of the UAV. The position A can be used for the avionics base since it is larger than position C. Moreover, if the payload was a camera, the front position would be better for visibility. The internal components set up is shown in Figure 4.12. The precise relative position of each element is not given since there can be small adjustment during the fuselage design.

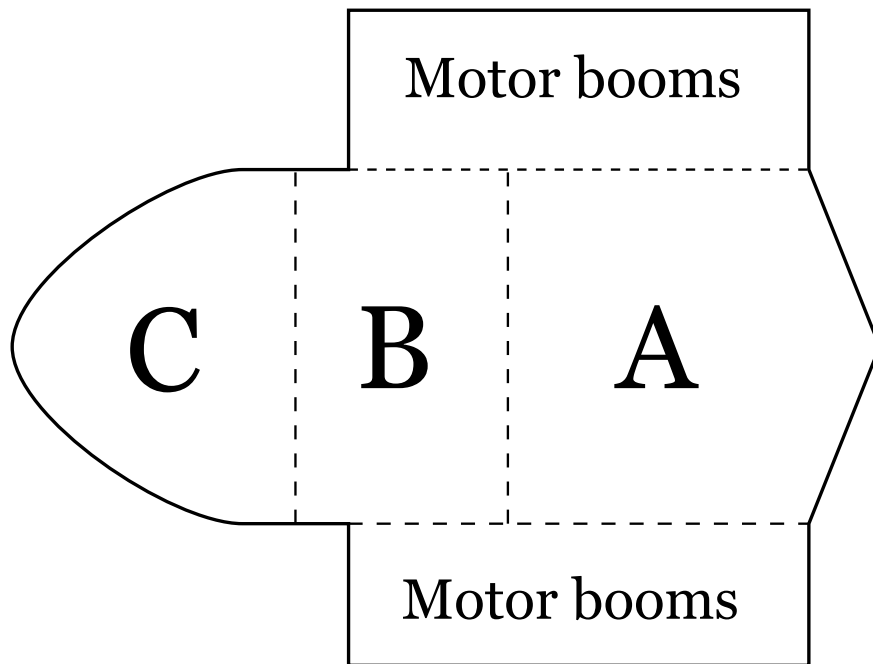


Figure 4.10: Fuselage layout: three positions in the central part are highlighted; the lateral parts are dedicated to the motor booms.

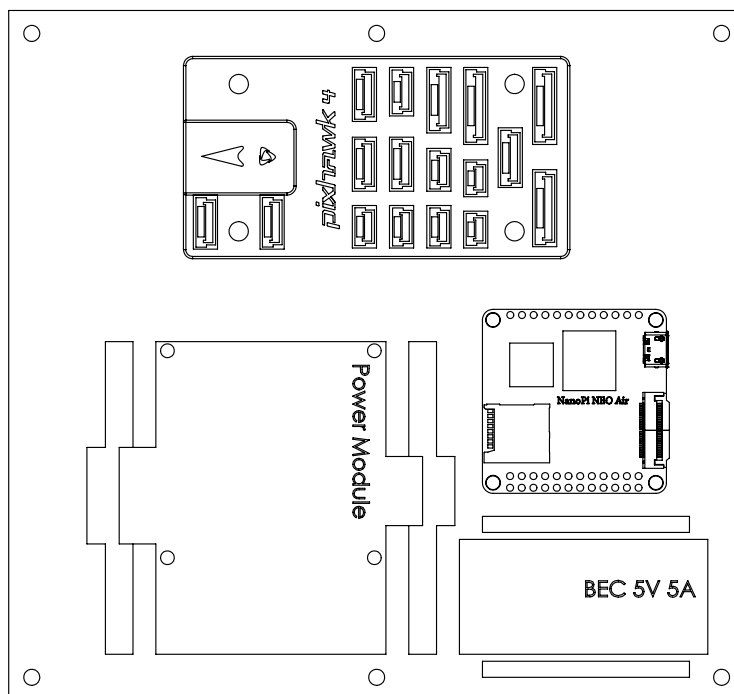


Figure 4.11: CAD view of the base designed for electronics.

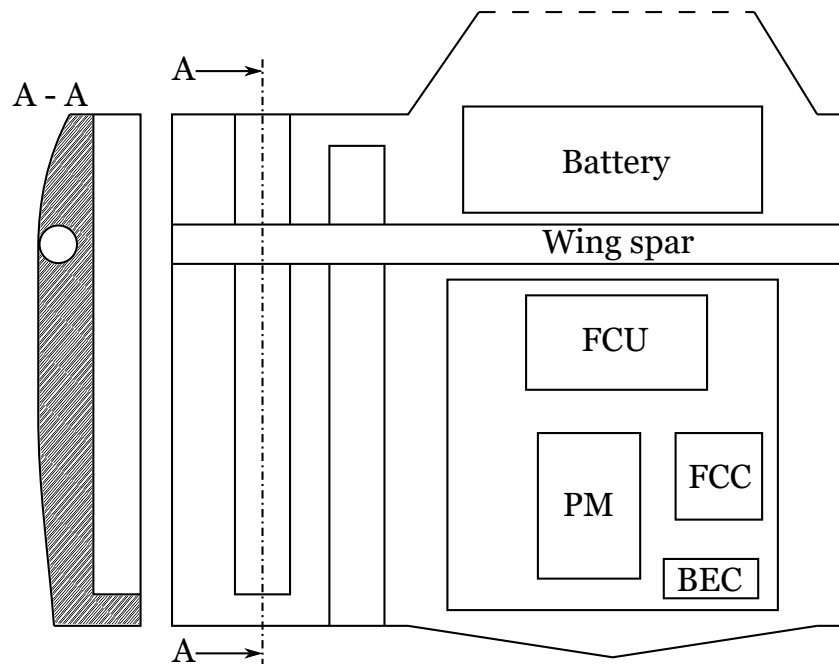


Figure 4.12: Disposition of the components inside the fuselage; the arrangement for the motor booms can also be seen. The cut A-A, shown on the left, presents the disposition of the wing spar on top of the motor booms.

Once the fuselage layout has been decided it is time to consider the fuselage structural design. Given the complex geometry of the fuselage, it has been decided to produce it with additive manufacturing. Considering the experience of Southampton University UAV laboratories (reference [16]), the fuselage will be produced in SLS nylon. A proof of the strength of this material can be found also in [67] and [68], which present the flight testing experience with SLS nylon printed UAVs.

It has to be stated that no detailed structural analysis has been performed on the fuselage. The final layout is the result of an empirical approach and it has been decided to accept a small increase in weight to ensure structural strength. This translates into not optimized wall thickness and in (probably) oversized junctions between the fuselage, the wing spar and the motor booms. Now these elements are analyzed in detail:

- The base wall thickness value has been taken from reference [16], which has been source of great inspiration in the design of the fuselage. The external fuselage walls have a thickness of 2 mm, but are reinforced with ribs to increase the overall structural strength.
- The junctions have been oversized with the use of multiple connections, large encastre area and reinforcement carbon fiber tubes. The front and



Figure 4.13: Carbon fiber tubes locking mechanism.

rear engine booms are two separate elements placed side by side in the fuselage, as it can be seen in Figure 4.12. In this way it is possible to use almost all the fuselage length for the encastre. The two separate booms are then connected with junction elements attached to the fuselage base. The front boom junction is shaped to connect also the wing spar housing to increase the connection between the structural elements inside the fuselage.

- To ensure higher survivability in time, the 3D printed housings for the motor booms and the wing spar are reinforced with other carbon fiber tubes with larger diameter: in the case of the wing spar the reinforcement has inner diameter 16 mm and outer 18 mm while the motor booms reinforcement has inner diameter 18 mm and outer 20 mm.

Some details have to be considered to complete the fuselage design. The wing spar carbon fiber tube and the motor booms are encastred inside housings connected to the fuselage; to avoid them to slide inside their housings, a smart system has been designed: taking inspiration from bicycles and reference [16], a lock mechanism has been designed (Figure 4.13). It is made up of a ring coaxial with the tube and of a lever which allows to tighten the ring around the tube. In this way the tube is locked. Since there is no third-party ring of the desired diameter, the required rings have been printed in ABS. The levers are off-the-shelf components from a bike shop.

The second detail to be considered is related to accessibility. To install the internal components during the assembly and to change battery in operative conditions, it is required to access the inner part of the fuselage. To avoid small openings, it has been decided to remove completely the coverage. This coverage has been divide into three parts: two lateral elements and one in the center. Figure 4.14 shows this division. The lateral parts of the coverage are intended to be

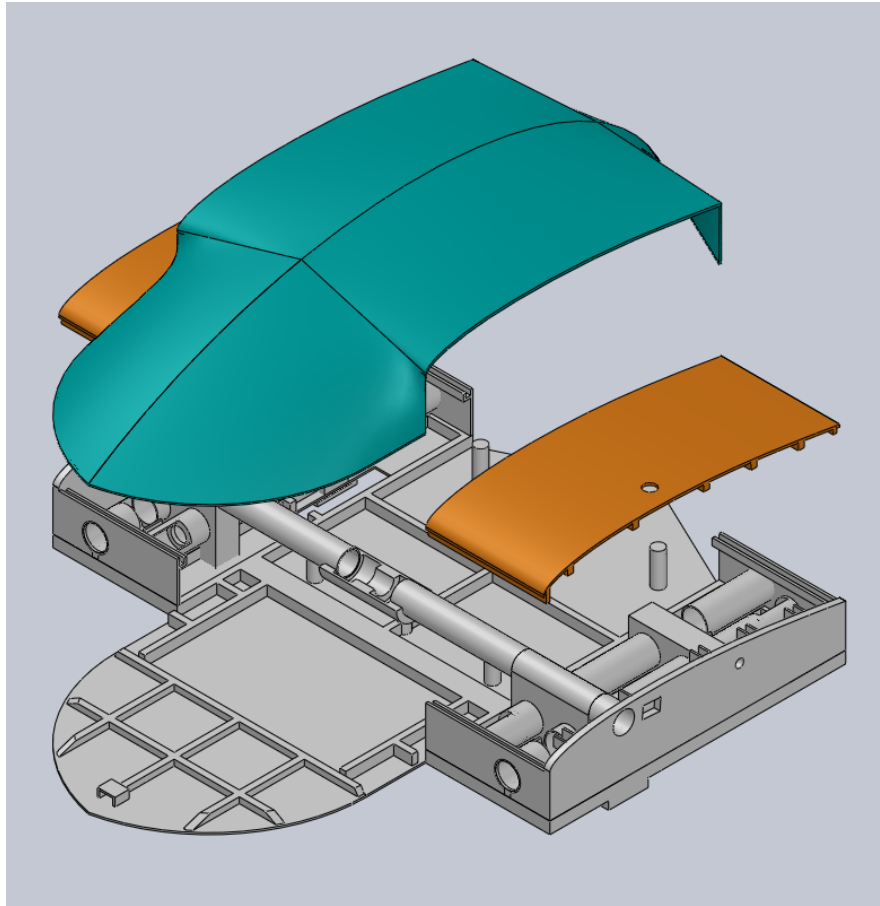
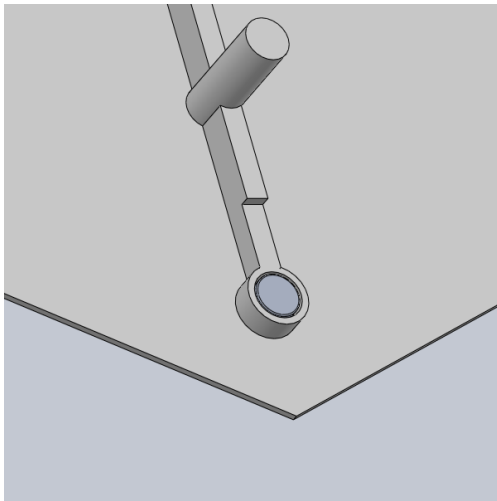


Figure 4.14: The fuselage is divided into four parts: a base, a central coverage and two lateral coverages.

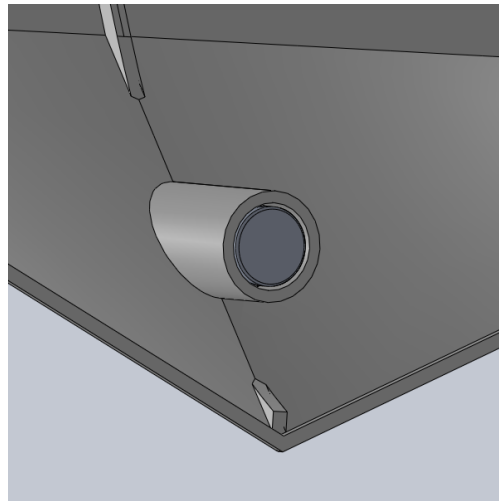
fixed once the assembly is completed while the central part can be removed easily to access the battery and the avionics. A set of magnets has been placed in the rear part of the fuselage to lock the central coverage during flight (Figure 4.15a and Figure 4.15b) together with a front pin, shown in Figure 4.15c and Figure 4.15d.

The last elements to be considered are the motor booms: it has been decided to insert all the power and signal cables that connect the avionics/battery to the motors inside the carbon fiber tubes. A custom design of the fuselage housings for the motor tubes has been performed to guarantee easy cable management in the assembly phase and in the daily operative life (Figure 4.16). These housings present also a portion in which the locking elements of Figure 4.13 can be placed, as it can be seen in Figure 4.16a.

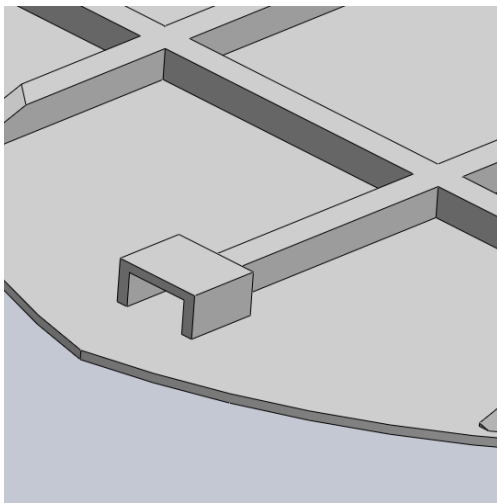
Last but not least, a set of support points have been designed to be attached to the bottom of the fuselage. These small feet are designed to prevent the FF propellers from touching the ground before take-off and after landing. Figure 4.17



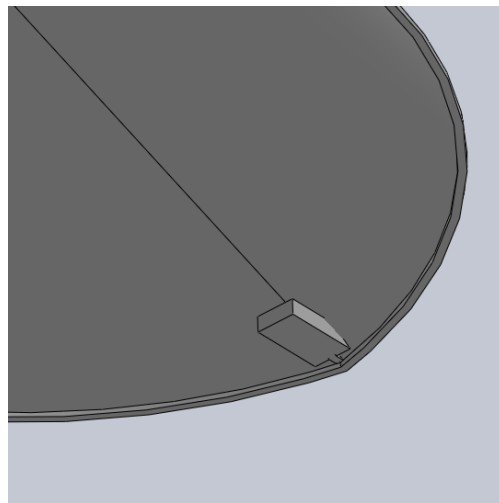
(a) Magnets on the fuselage base.



(b) Magnets on the fuselage cover.

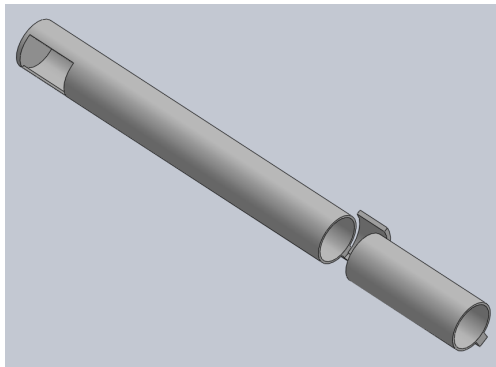


(c) Pin housing on the fuselage base.

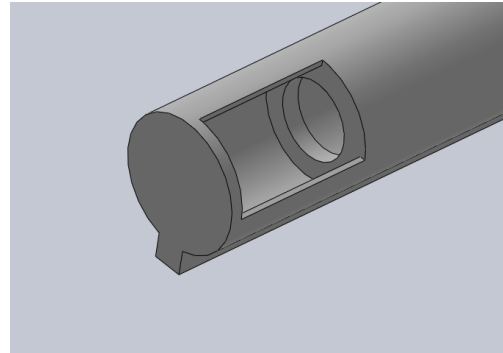


(d) Frontal pin on the fuselage cover.

Figure 4.15: Two systems connect the central coverage to the fuselage base: a mechanical pin in the front part and a set of magnets in the rear part.

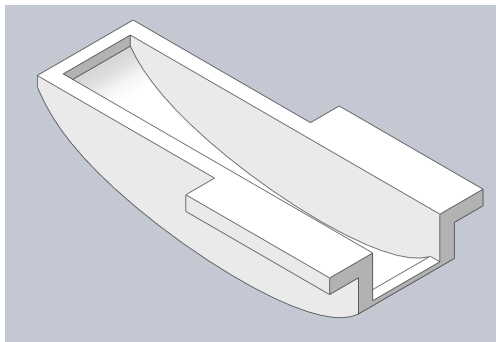


(a) Complete view.

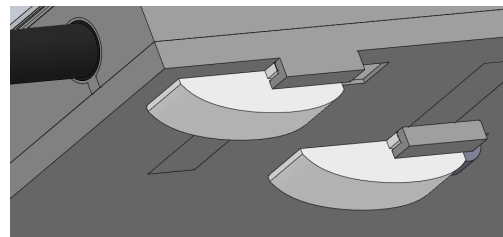


(b) Detail of the terminal part which allows to insert motor power cables.

Figure 4.16: Housing for the motor booms.



(a) View of a single aircraft support.

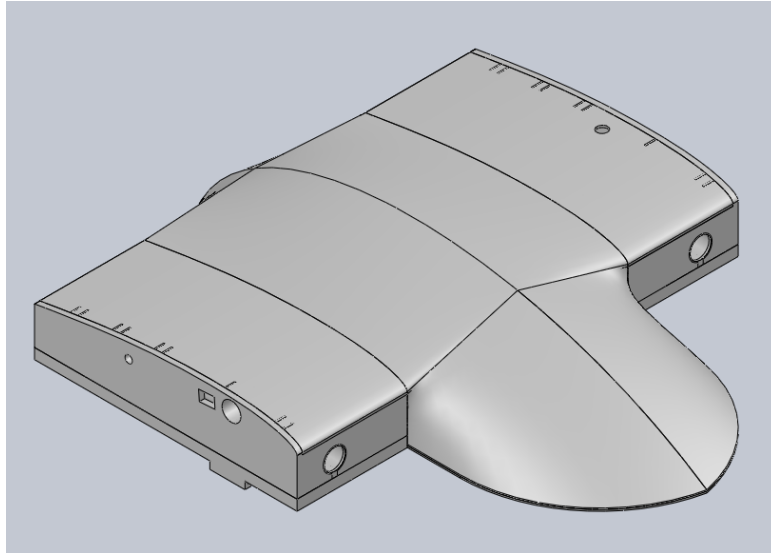


(b) Aircraft supports connected to the fuselage.

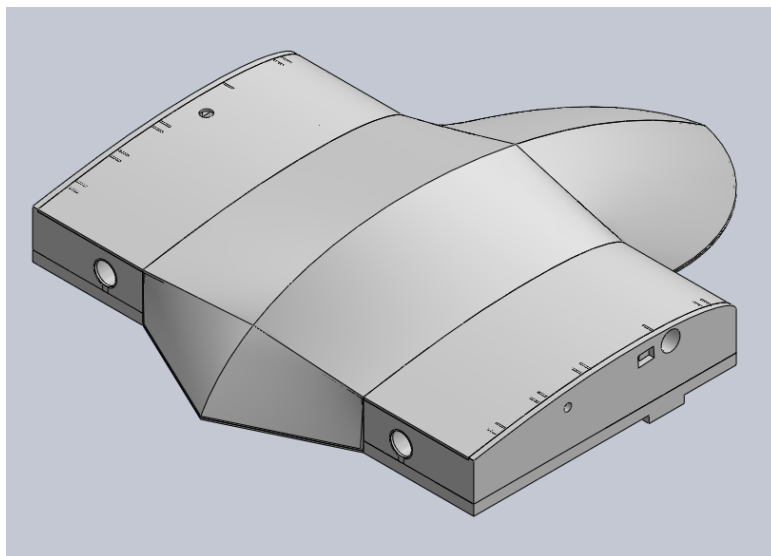
Figure 4.17: Aircraft support elements.

presents these elements; they are in-house printed in ABS.

A complete set of pictures of the fuselage is presented in Figure 4.18 and Figure 4.19.

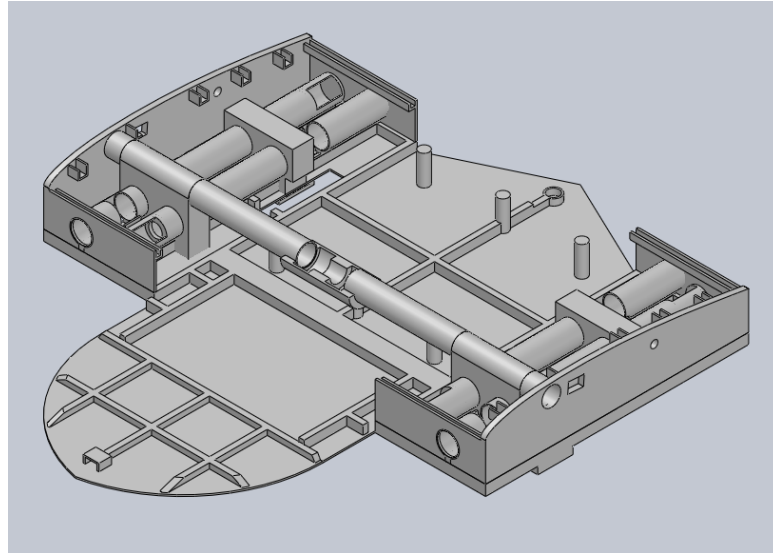


(a) Front view of the outside.

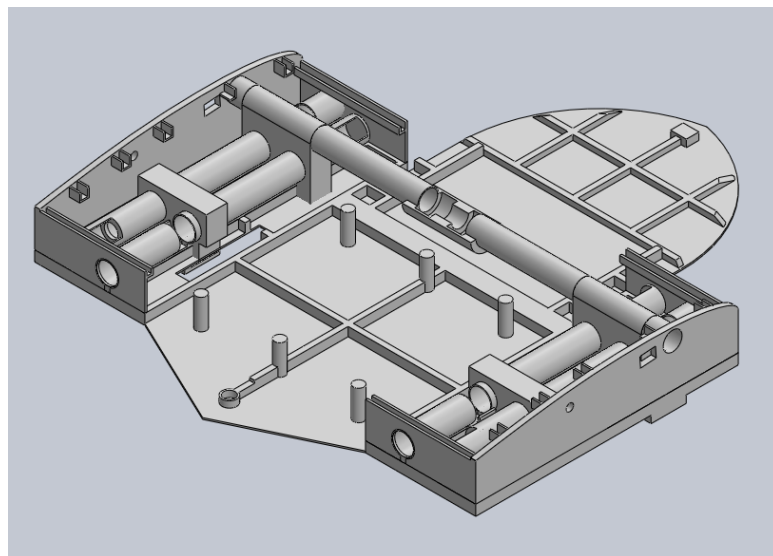


(b) Rear view of the outside.

Figure 4.18: External views of the fuselage CAD.



(a) Front view of the inside.



(b) Rear view of the inside.

Figure 4.19: External views of the fuselage CAD.

Chapter 5

Final design steps

This chapter is made up of independent aspects, all related to the conclusion of the design: selection of the tail and design of the moving surfaces, preparation of the production files and analysis of the flight dynamics. Each one of the chapter sections is devoted to one particular aspect.

5.1 Tail selection

As stated in Section 2.5, the final tail choice is based on the longitudinal static stability. A detailed design of the two tail options has been done considering the structural layout shown in Section 3.2. It has been decided to redesign the U tail with the tail arm of the V tail. In this way the two options are fully interchangeable without the need of changing the rear motor booms. It is then possible to evaluate the longitudinal static stability through the static margin

$$e = \frac{x_{CG} - x_N}{MAC} \quad (5.1)$$

where x_N and x_{CG} are the neutral point position and the CG position in a reference frame directed from the tail to the nose, respectively. The aircraft is longitudinally statically stable if $e > 0$, *i.e.*, the CG is in front of the neutral point. The neutral point position has been estimated using XFLR5, as presented in Table 2.3. For ease of reading the values of x_N for both the tail options are presented in the following, measured from the leading edge of the wing:

- U tail: $x_N = -13 \text{ cm}^1$
- V tail: $x_N = -10 \text{ cm}$.

¹Being the axis from the tail to the nose, a negative value means that the point is behind the wing leading edge.

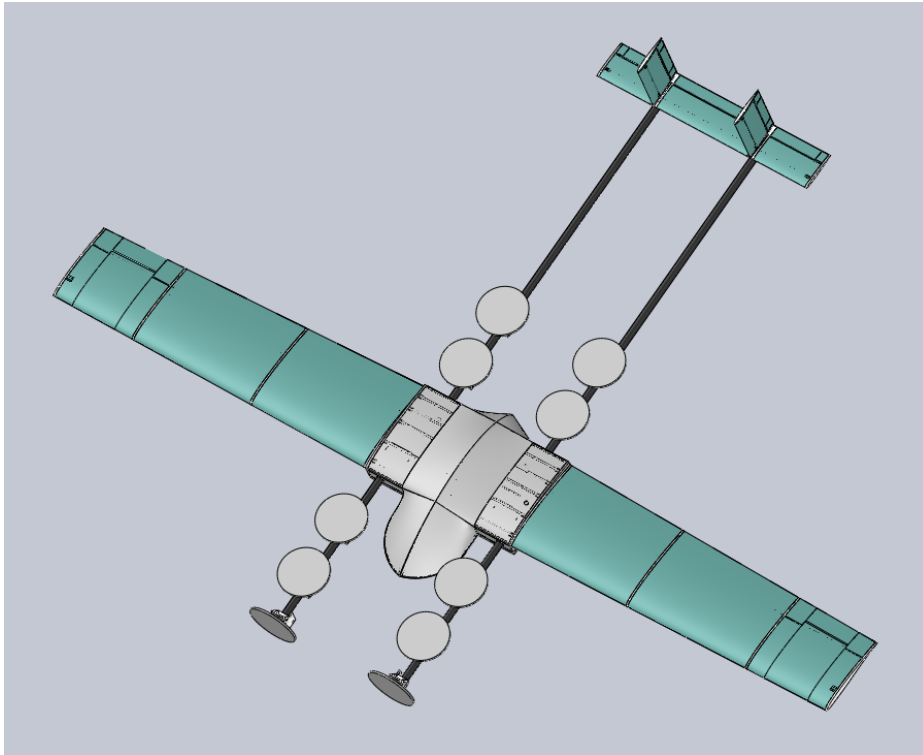


Figure 5.1: CAD of the UAV in U tail configuration.

The position of the center of mass has been estimated using the CAD developed in SolidWorks. Figure 5.1 and Figure 5.2 present the whole aircraft in the two tail configurations. All the main elements such as the fuselage, the wing, the tail, the avionics components and the engines have been considered. Only the moving surface servomotors have been neglected since they have not been selected yet. However, their weight is in the order of 10 g_f so they do not affect too much the CG position.

The position of the CG is presented in the following list, measured from the leading edge of the wing:

- U tail: $x_{CG} = -10\text{ cm}$
- V tail: $x_{CG} = -9\text{ cm}$.

Considering equation (5.1), the positions of neutral point and center of gravity and that $MAC = 23\text{ cm}$, the resulting static margins are:

- U tail: $e = 13\%$
- V tail: $e = 4\%$.

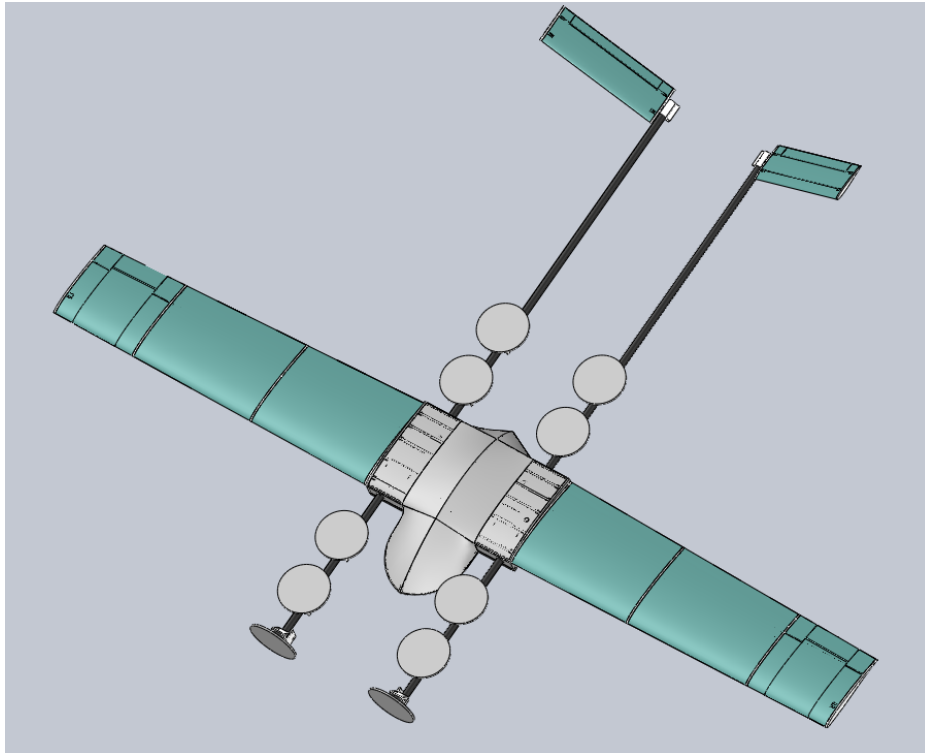


Figure 5.2: CAD of the UAV in V tail configuration.

Considering that there are some uncertainties and approximations both in the estimate of the neutral point (for example, XFLR5 neglects the fuselage) and in the computation of the CG, it can be stated that the V tail configuration has very reduced (or indifferent) static stability. The U tail, on the other side, presents a reduced, but positive, static margin. After these two considerations it has been decided to select the U tail as tail configuration. The design values of this tail are presented in Table 5.1.

5.2 Moving surfaces design

Once the tail has been selected, the aircraft moving surfaces have to be designed. In the actual configuration wing ailerons, tail elevator and tail rudder have to be designed. Then the servomotors can be selected considering the hinge moments computed through XFLR5. The procedure adopted for the sizing of the moving surfaces is taken from [22].

5.2.1 Aileron design

The ailerons are mainly used to perform lateral control producing a rolling moment. The aileron maximum deflections (both positive and negative), the span,

Parameter	Value
Tail arm l_{opt} [cm]	103
Horizontal surface S_h [m ²]	0.06
Vertical surface S_v [m ²]	0.02
Horizontal span b_h [cm]	61
Vertical span b_v [cm]	18
Airfoil	NACA 0008
AR_h	6.7
AR_v	2.0
Horizontal chord MAC_h [cm]	10
Vertical chord MAC_v [cm]	10
Horizontal tail incidence i_h [deg]	3

Table 5.1: U tail parameters summary. The data of the vertical tail are related only to one part, so the overall surface is twice the value presented.

the position and the chord have to be defined to design successfully the ailerons. According to reference [22], a criterion useful in sizing the aileron is to achieve a desired bank angle in a fixed time. It is suggested to consider the MIL F 8785 C regulation for flight qualities² (reference [20]) and to select the class and flight phase adapted to the aircraft that is being designed. The aircraft class appropriate for the VTOL UAV is class 1 (small and light aircraft with low maneuverability), the flight phase is B (climb, cruise, loiter, descent and aerial delivery). These class and flight phase have been used also in the design of the UAVs of the Southampton University (reference [16]). MIL F 8785 C requires, for aircraft in class 1 and flight phase B, to reach a bank angle $\phi_{required}$ of 45° in 1.7 s for acceptability level 1 or 2.5 s for acceptability level 2. Both levels of acceptability can be considered according to reference [16].

The next step is to fix the aileron position on the wing: it is convenient for the aileron to be as far away as possible from the roll axis to generate the highest rolling moment. Then, the aileron is placed at the tip of the wing. It has been decided the span b_a of each aileron to be 20% of the wing span, namely $b_a = 225$ mm. Considering the suggestion in [22], the aileron chord is $MAC_a = 20\%MAC$. Considering the aileron chord, it is possible to compute the aileron effectiveness parameter τ_a using Figure 2.12 from [22]. The obtained value is $\tau_a = 0.4$. The typical values of deflection for the aileron, according to [22], are $\delta_a^{max+} = 20^\circ$ and $\delta_a^{max-} = -20^\circ$.

The aileron roll performance is now evaluated for a comparison with the initial requirement from [20]. First, the rolling moment coefficient derivative with respect

²This regulation is intended for military manned aircraft. Since there is no handling qualities regulation for UAVs, MIL F 8785 C has been selected, as done in [16].

to aileron deflection is computed as

$$C_{\mathcal{L}\delta_a} = \frac{2C_{L\alpha}\tau_a C_{root}}{Sb} \left[\frac{y^2}{2} + \frac{2}{3} \left(\frac{\lambda - 1}{b} \right) y^3 \right]_{y_{in}}^{y_{out}} \quad (5.2)$$

with $C_{L\alpha}$ slope of the wing lift curve, C_{root} wing root chord, y coordinate along the wing which goes from the aileron inner position y_{in} to the aileron outer position y_{out} . Equation (5.2) is based on a simple strip integration method applied to the wing (the interested reader can find the detailed derivation in Chapter 12 of [22]). The rolling moment coefficient is easily obtained as

$$C_{\mathcal{L}} = C_{\mathcal{L}\delta_a} \delta_a^{max+}. \quad (5.3)$$

The rolling moment in cruise conditions due to the aileron deflection is computed as

$$\mathcal{L} = \frac{1}{2} \rho_{cr} v_{cr}^2 S C_{\mathcal{L}} b. \quad (5.4)$$

To compute the bank angle reached with the aileron deflection δ_a^{max+} , it is necessary to start from a simple scheme of the maneuver as the one in Figure 5.3. The rolling moment equilibrium is

$$2y_a \Delta L - y_D \Delta D = I_{xx} \dot{p} \quad (5.5)$$

where ΔL and ΔD are, respectively, the change in lift and drag due to the aileron deflection. According to [22], y_a is the average distance between each aileron and the roll axis and y_D is the average distance between the rolling drag center and the roll axis. Reference [22] states that a typical value of y_D is 40% of the wing semispan. I_{xx} is the roll inertia (computed from the SolidWorks CAD) and \dot{p} is the time rate of change of the roll rate p , which can be written as

$$\dot{p} = \frac{d}{dt} p. \quad (5.6)$$

The roll rate is defined as

$$p = \frac{d}{dt} \phi \quad (5.7)$$

with ϕ roll angle. Combining equation (5.6) with equation (5.7) it can be easily obtained

$$\dot{p} d\phi = p dp \quad (5.8)$$

and, solving equation (5.8) for ϕ , it gives

$$\phi = \int \frac{p}{\dot{p}} dp. \quad (5.9)$$

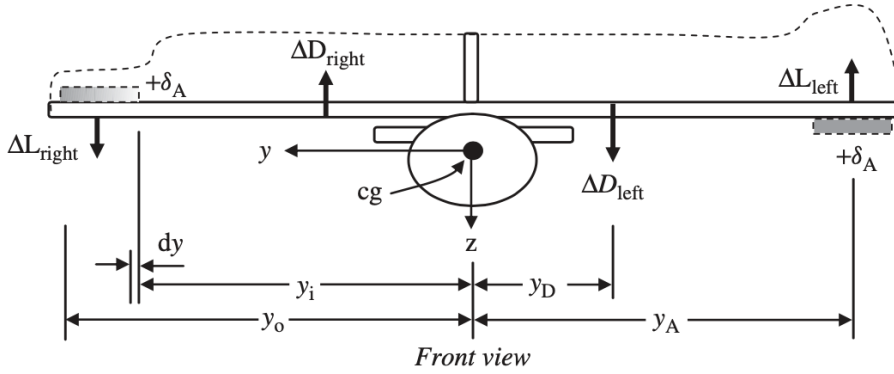


Figure 5.3: Incremental change in lift and drag in generating a rolling motion with aileron deflection. Source [22].

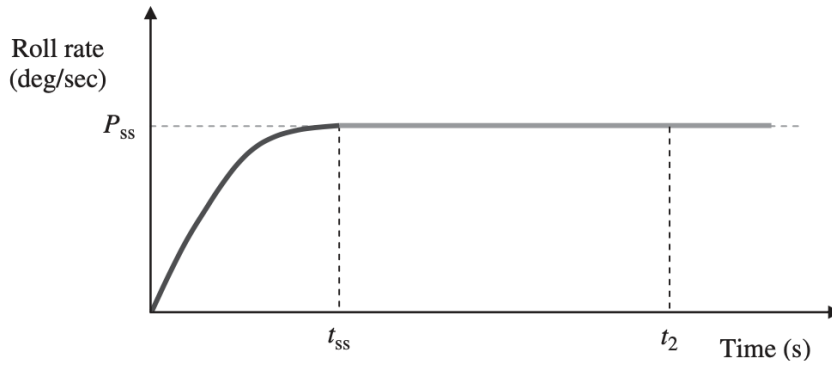


Figure 5.4: Aircraft roll rate response to aileron deflection; source [22].

Computing \dot{p} from equation (5.5) and substituting it into equation (5.9) leads to

$$\phi_1 = \int_0^{p_{ss}} \frac{I_{xx} p}{\mathcal{L} + y_d \Delta D} dp. \quad (5.10)$$

Both ϕ_1 and p_{ss} are related to the typical response to an aileron maneuver: as it can be seen in Figure 5.4, the roll rate increases up to a steady state value, called p_{ss} , then it remains constant and equal to p_{ss} . The roll angle for which the steady state roll rate is reached is called ϕ_1 . When the roll rate is equal to p_{ss} there is equilibrium between the aileron rolling moment and the aircraft drag due to roll motion:

$$\mathcal{L} = \Delta D y_d. \quad (5.11)$$

Since

$$\Delta D = \frac{1}{2} \rho (p_{ss} y_d)^2 (S + S_v + S_h) C_{D_{roll}} y_d, \quad (5.12)$$

with S wing surface, S_v vertical tail surface, S_h horizontal tail surface and $C_{D_{roll}}$ drag due to roll coefficient, solving equation (5.11) for p_{ss} after the substitution of equation (5.12) gives

$$p_{ss} = \sqrt{\frac{2\mathcal{L}}{\rho(S + S_v + S_h)C_{D_{roll}}y_d^3}}. \quad (5.13)$$

Combining equation (5.10) and equation (5.13), with some mathematical manipulation it is obtained

$$\phi_1 = \frac{I_{xx}}{\rho(S + S_v + S_h)C_{D_{roll}}y_d^3} \ln(p_{ss}^2). \quad (5.14)$$

The time to reach ϕ_1 is computed as

$$t_1 = \sqrt{\frac{2\phi_1}{\dot{p}}}; \quad (5.15)$$

if the value of ϕ_1 is greater than the required value $\phi_{required}$, then the time to reach $\phi_{required}$ is smaller than t_1 . Therefore, equation (5.15) has to be modified into

$$t_{required} = \sqrt{\frac{2\phi_{required}}{\dot{p}}}. \quad (5.16)$$

The value of $t_{required}$ computed with equation (5.16) has to be compared to the initial requirements from [20]: 1.7 s for acceptability level 1 and 2.5 s for acceptability level 2. According to [22], $C_{D_{roll}}$ values are in a range between 0.7 and 1.2. $C_{D_{roll}}$ is assumed to be the mean value of the interval, namely $C_{D_{roll}} = 0.95$. The value of the inertia I_{xx} is obtained from the SolidWorks CAD: $I_{xx} = 1 \text{ kg m}^2$. It is obtained $t_{required} = 0.9 \text{ s}$, which is lower than the requirement for level 1. Given that, the designed aileron satisfies the requirement from [20].

5.2.2 Elevator design

The elevator design procedure proposed in [22] is based on the take-off rotation requirement, which is the most demanding condition for a general aviation aircraft. Since the VTOL UAV does not take-off conventionally, this procedure cannot be adopted. Then it has been decided to use common elevator values from [22] and to check *a posteriori* that the proposed design can trim the aircraft in all the speed range from the stall speed to the maximum one.

The values selected are:

- $b_e = b_h$,
- $MAC_e = 0.3MAC_h$,

- $\delta_e^{max+} = 20^\circ$,
- $\delta_e^{max-} = -25^\circ$.

A standard flight mechanics formulation has been used to compute the equilibrium elevator deflection $\delta_e^{equilibrium}$ for flight at v_s and v_{max} . The obtained values of elevator deflection are well inside the range $\delta_e^{max-} \div \delta_e^{max+}$, meaning that the selected elevator values are ok.

5.2.3 Rudder design

The rudder design procedure is the same adopted in Section 2.5, so the reader can refer to it. The procedure has been updated with the U tail values of Table 5.1 and the FF engine values of Table 4.2. The resulting rudder specifications are:

- $b_r = 0.6 b_v$,
- $MAC_r = 0.15 MAC_v$,
- $\delta_r^{max+} = 30^\circ$,
- $\delta_r^{max-} = -30^\circ$.

5.2.4 Servomotors selection

Once the moving surfaces have been designed, the servomotors can be selected. The choice is based on the hinge moments computed using XFLR5. The software computes the hinge moment coefficient per unit length; this value is then multiplied for the moving surface span to obtain the hinge moment coefficient C_H . The value of the hinge moment is

$$M_H = \frac{1}{2} \rho v^2 MAC^2 C_H b_{mov} \quad (5.17)$$

according to [69]; b_{mov} is the moving surface span. Three values of C_H have been computed, one for the aileron, one for the elevator and one for the rudder. The maximum value has been then multiplied for a safety factor equal to 1.7, leading to $M_H^{max} = 0.24$ Nm. The online store HobbyKing ([61]) has been searched looking for servomotors capable of delivering M_H^{max} . To make the assembly and future maintenance easier, only one model have been considered for all the moving surfaces, not a different one based on the specific hinge moment of each moving surface. The selected model is the Corona 939 Metal Gear shown in Figure 5.5. It is a 12.5 g_f servomotor capable of at most 0.27 Nm.



Figure 5.5: Corona 939 Metal Gear servomotor for moving surfaces.

5.3 Production design

This section presents the practical aspects related to the production design: changes to the wing due to the manufacturing process and engine mountings.

5.3.1 Wing production

At the moment the designed wing has taper ratio $\lambda = 0.8$. This means that each foam part of the wing changes section along the quarter of chord axis. Once the design has been completed the DAER facility technicians have been contacted to arrange the production of the foam components. Since the hot wire machine in the DAER facility can produce only components extruded from a 2D profile, a tapered wing cannot be easily manufactured. A possible solution is to divide each foam block into several parts and then to fillet them by hand. This is a very difficult process and a good result is not guaranteed, then it has been decided to change the taper ratio to 1 and to produce a straight wing with the same span. This decision has influence on the aerodynamics of the aircraft, increasing the induced drag. However, the drag penalty has been accepted to make the production easier. The limitation of the hot wire machine does not affect the tail foam components since they have already unit taper ratio.

The change of the wing taper ratio has impact also on the wing and tail incidence: as explained in Chapter 2, the values of incidence are selected to achieve vertical force and pitch moment equilibrium in cruise conditions. In this way the aircraft can fly without aileron deflection in the longer flight phase. Changing the taper ratio without changing the span produces an increase in wing surface and a larger S affects the trim speed. The adjustments to wing incidence i_w and horizontal tail incidence i_h are performed using XFLR5: the software allows to

compute the trim condition (*i.e.*, $C_{MCG} = 0$ and $L = W_{TO}$) for different values of i_w and i_h . In the first attempt both incidences are changed simultaneously: i_w changes of 0.1° at each iteration while i_h of 0.01° . The trim condition is obtained for $i_w = 5^\circ$ (which is $+1^\circ$ with respect to the initial value) and $i_h = 3.1^\circ$ (which is $+0.1^\circ$ with respect to the initial value). Since the change in i_h is small and a modification of the tail CAD requires a larger effort than adjusting the wing incidence, it has been decided to leave i_h unchanged and to perform a second iteration changing only the wing incidence. At this iteration the trim in cruise speed is reached with $i_w = 4.9^\circ$ (i_h is still equal to 3°).

It has been decided to leave unchanged the moving surfaces design since the impact of taper ratio change on them is small.

5.3.2 Engine mountings

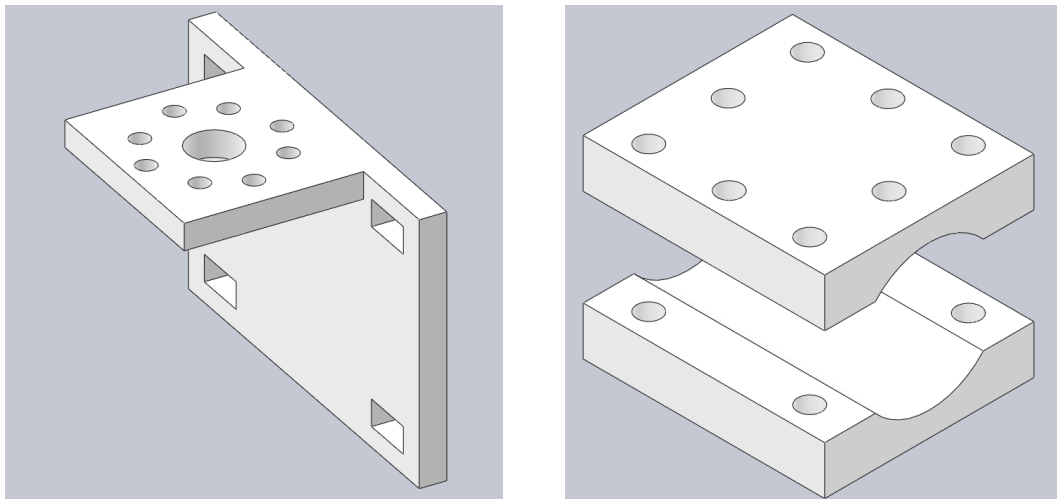
A custom design is done to connect the motors to the carbon fiber tubes with 3D printed supports. The important aspect is to design an easy connection that makes assembly simple and fast. Each mounting has to accommodate the engine and its ESC.

The firsts to be considered are the VF motors; to make things simpler a single model has to fit both right and left motors. The final design is made of two parts: a plate for the engine and the ESC (Figure 5.6a) and another for the carbon fiber tube (Figure 5.6b). In this way it is easy to connect the propulsive components to the first plate and then this plate directly to the one attached to the boom, as shown in Figure 5.6c.

The FF engine mountings are different for left and right booms; the structure is designed to increase the propeller clearance from the ground. Figure 5.7 presents the FF engine support.

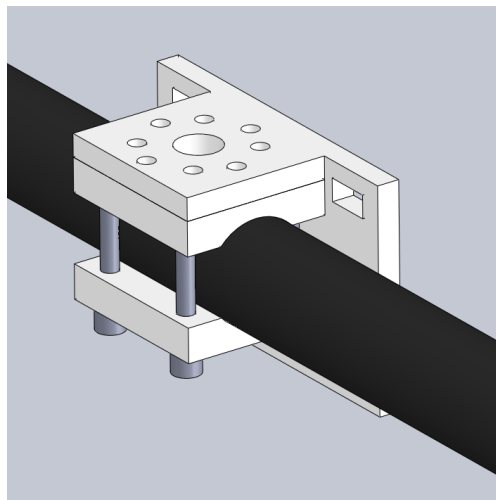
5.4 Trimmed polar and flight dynamics analysis

In the early stages of the design (see Chapter 1) an estimate of the UAV parabolic drag polar has been performed based on a procedure from [21]. Now a model of the aircraft aerodynamics is available in XFLR5 and can be used to produce a parabolic drag polar in trimmed conditions. This curve is important since it presents the values of C_L and C_D in trimmed flight conditions. Since the aircraft weight is fixed to W_{TO} and the maximum altitude range is very limited due to EU UAVs regulations ([17] and [18]), only one trimmed polar has been computed. The simulation conditions used in XFLR are the cruise ones. The trimmed drag polar obtained in XFLR5 is presented in Figure 5.8. It has to be stated that the C_D computed is surely smaller than the real one because the XFLR5 model



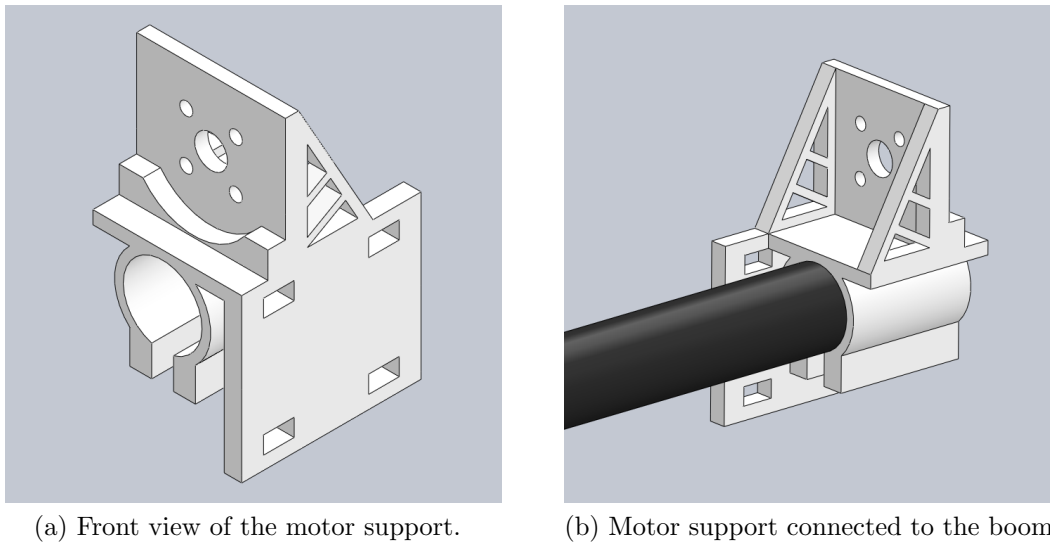
(a) Support plate for motor and ESC.

(b) Boom connection element.



(c) Vertical engine support connected to the boom.

Figure 5.6: VF engine supports.



(a) Front view of the motor support.

(b) Motor support connected to the boom.

Figure 5.7: FF engine supports.

neglects the fuselage and engines drag contributions³. These two C_{D_s} have not been computed using the empirical procedures proposed in [42] and [43] since these methods were developed for other types of aircraft (large jet/turboprop engines) which are different from the VTOL ones⁴. The difference in terms of drag is clearly visible in Figure 5.8 comparing the actual trimmed polar to the initial estimate of the drag polar. As stated in Chapter 1, the zero lift drag coefficient C_{D_0} of the preliminary drag polar has been computed starting from geometrical data of the competitors and it has been increased by 20% to be more conservative, so this emphasizes the difference.

The procedure adopted to compute the trimmed drag polar gives the opportunity to check again the design of the elevator: each trimmed condition represented by a couple $C_L - C_D$ is associated with an elevator deflection δ_e . As for the hand computation mentioned in Section 5.2.2, also in the XFLR5 model the maximum and minimum elevator deflections for trim are well inside the maximum design range. Since the deflection at stall speed is -2.0° ⁵ and the deflection at maxi-

³XFLR5 developer, A. Deperrois, plans to add fuselage modeling to the next release of XFLR5.

⁴An attempt to compute the fuselage C_D has been performed. However, the input data for the empirical procedure presented in [42] are below the minimum values considered in such procedure, so a lot of extrapolations have to be done. The result of these extrapolations is too sensitive: a small change of some input parameters produces a C_D which is four times the previous. Given that, no additional drag contribution has been taken into consideration in the parabolic drag polar.

⁵The elevator deflection is positive for downward deflections and negative for upward deflections.

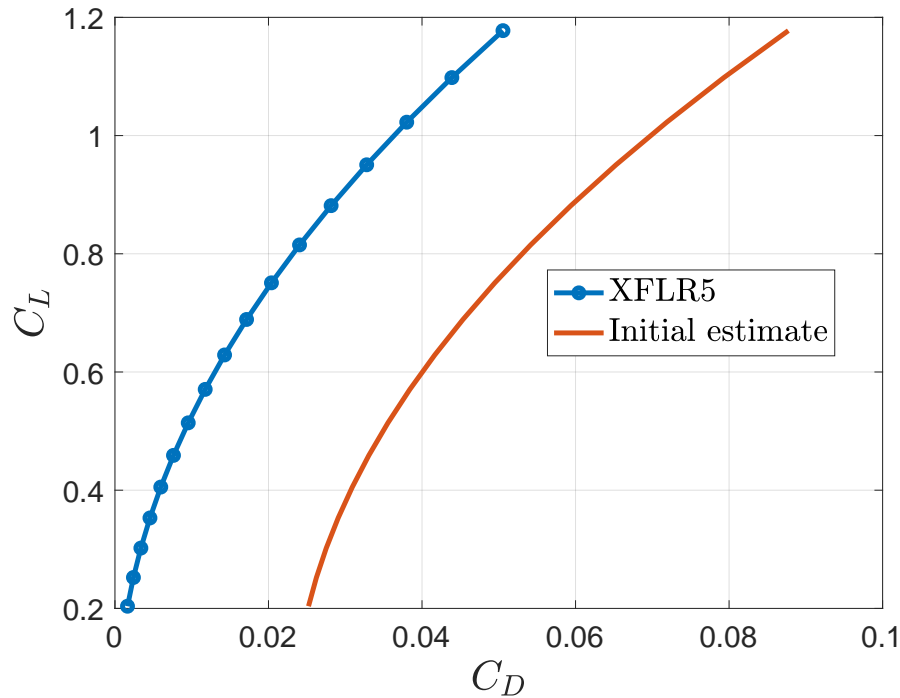


Figure 5.8: Trimmed drag polar in cruise conditions at W_{TO} .

mum speed is 1.5° , the proposed elevator design can be considered oversized with respect to the operative conditions. For future versions of the UAV a reduced elevator can be considered. Figure 5.9 presents the elevator deflection in the speed range as computed through XFLR5.

As further step in the analysis and evaluation of the designed aircraft, it has been decided to estimate the flight dynamics characteristics of the aircraft. At the moment the UAV has not been built yet, however there are lots of data that can be used to compute the flight modes in forward flight configuration in terms of frequency and damping. The evaluation is done using XFLR5, which allows to compute the longitudinal and lateral modes of an aircraft. As mentioned in Section 5.2.1 for the aileron design, MIL F 8785 C (reference [20]) has been selected for the evaluation of the flight qualities of the UAV. The reference aircraft class is 1 with flight phase B; the same class and phase have been considered for the evaluation of the UAVs of Southampton University ([16]).

The aerodynamic data is computed directly inside XFLR5 while the mass and inertia information is taken from the SolidWorks 3D model of the UAV. This data is used to build the six degree of freedom model of the aircraft (XFLR5 follows the approach proposed in [70]); from the model the eigenvalues associated to the longitudinal modes (short period and phugoid) and the lateral modes (roll, dutch roll and spiral) are computed. Table 5.2 presents the real and imaginary parts of each eigenvalue. The position of the eigenvalues is shown in the complex plane in Figure 5.10 and Figure 5.11. As it can be seen, all the modes except the spiral

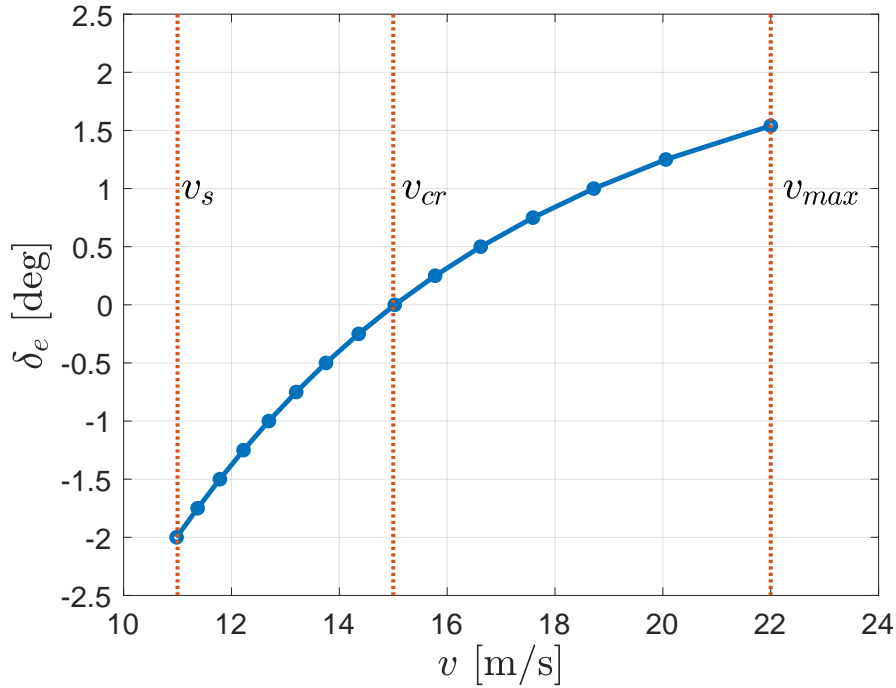


Figure 5.9: Elevator deflection as function of the speed range.

Mode	Real part	Imaginary part
Short period	-5.3	4.25
Phugoid	-0.0053	0.59
Roll	-21.2	0.0
Dutch roll	-1.0	4.1
Spiral	0.18	0.0

Table 5.2: Eigenvalues of the flight modes in forward flight configuration.

have negative real part, so they are stable. Moreover, the real part of the spiral eigenvalue is small, close to the origin of the complex plane.

The MIL F 8785 C regulation sets requirements in terms of damping ratio for the short period, the phugoid and the dutch roll, in terms of time constant for the roll mode and, for the unstable spiral mode, in terms of time to double. Given an eigenvalue $\lambda = a + ib$, its natural frequency ω_n is defined as

$$\omega_n = \sqrt{a^2 + b^2} \quad (5.18)$$

while its damping ratio ξ (for eigenvalues with $a < 0$) is

$$\xi = -\frac{a}{\omega_n}. \quad (5.19)$$

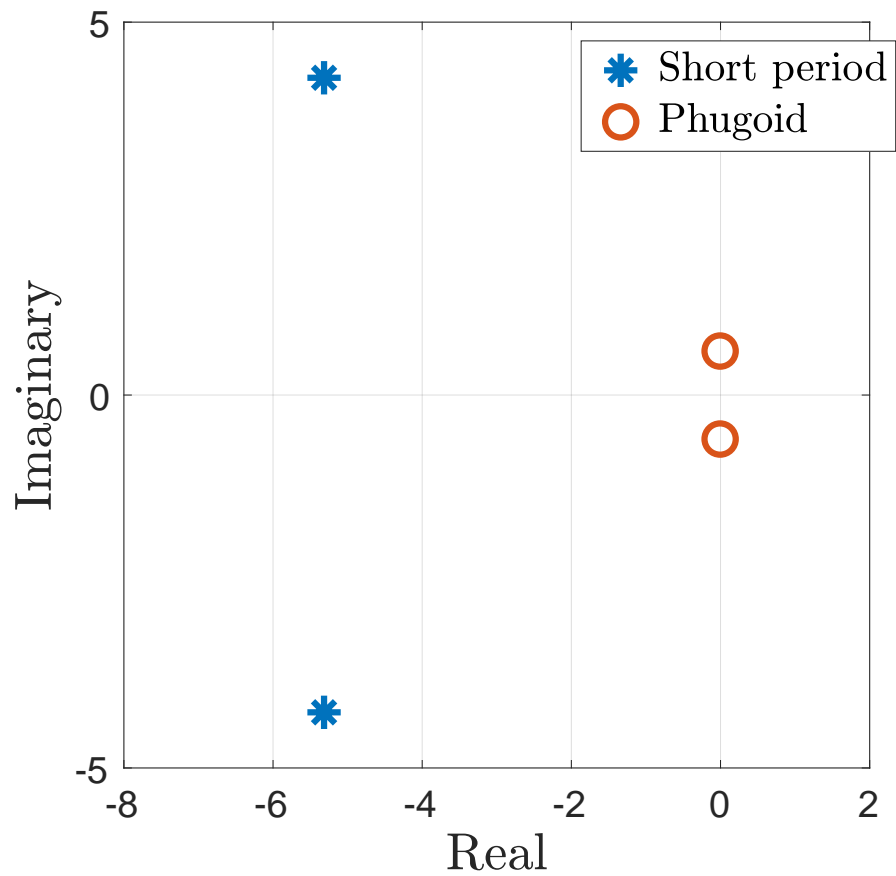


Figure 5.10: Longitudinal flight modes in the complex plane.

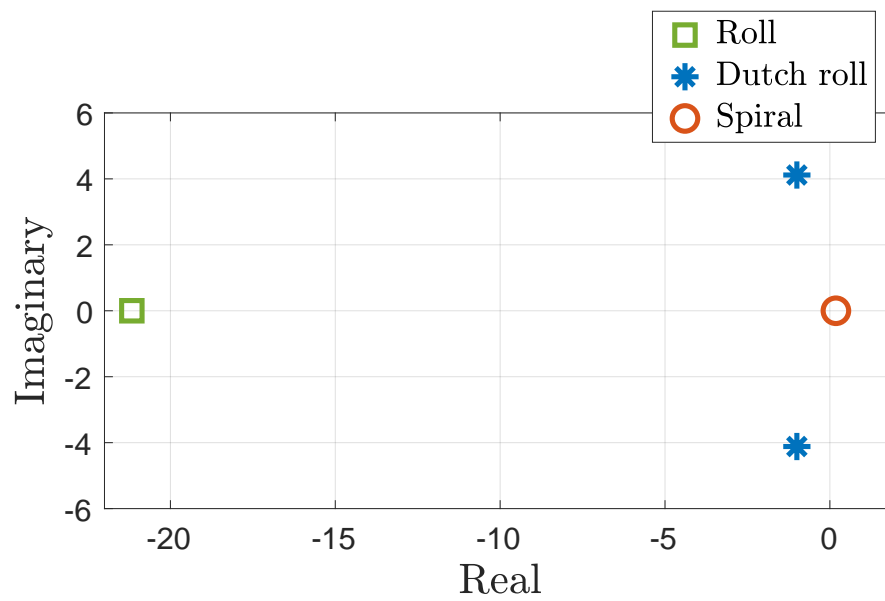


Figure 5.11: Lateral flight modes in the complex plane.

Mode	$\omega_n[Hz]$	ξ	Requirement for level 1	Level obtained
Short period	1.08	0.78	$\xi \in [0.3 \div 2.0]$	Level 1
Phugoid	0.09	0.01	$\xi > 0.04$	Level 2
Roll	3.37	1.00	$\tau_R < 1.4$ s	Level 1
Dutch roll	0.67	0.24	$\xi > 0.08$ & $\omega_n > 0.4$ rad/s	Level 1
Spiral	0.03	-1.00	$T_2 > 12$ s	Level 3

Table 5.3: Flight modes comparison with respect to MIL F 8785 C regulation. $\tau_R = 0.047$ s for the roll mode and $T_2 = 3.8$ s for the spiral mode.

In the case of the roll mode it is required to evaluate the time constant τ_R defined, according to reference [16], as

$$\tau_R = \frac{\ln(1 - 0.632)}{a}. \quad (5.20)$$

Equation (5.20) defines the roll mode time constant as the time it takes to achieve 63.2% of the final roll rate following a step input. In the case of the spiral mode the time to double T_2 has to be defined:

$$T_2 = \frac{\ln(2)}{|a|}. \quad (5.21)$$

Table 5.3 presents a comparison of the values of each mode with the requirement from MIL F 8785 C. Moreover, Table 5.3 presents the levels of acceptability reached for each flight mode. It has been assigned to the spiral mode a level 3 even if the requirement for this level from [20] is $T_2 > 4$ s and the obtained T_2 is only 3.7 s since the difference is small. In the future a detailed analysis of the flight modes can be performed after the flight testing of the real UAV. The spiral mode can be investigated further to increase its time to double with small design changes.

Chapter 6

LPV model of the forward flight mode

This chapter presents the implementation of a linear parameter varying (LPV) model of the aircraft forward flight mode. A LPV model is a linear model which depends on one (or more) variable parameter(s), called scheduling parameter(s). In the case of an aircraft, examples of the scheduling parameter can be the air-speed v , the flight altitude h or the CG position. A model of this kind is useful for control or simulation purposes since it allows to represent the system in different conditions, each one corresponding to a particular value of the scheduling parameter.

This chapter is organized as follows: the first section presents a brief theoretical background about LPV models, the second shows the approach adopted in the implementation and the third one is devoted to the results obtained.

6.1 LPV model theory

The idea of a LPV model is to provide a full-envelope model for control and simulation purposes. In fact, the linear time invariant (LTI) models obtained from identification of experimental data are accurate only near the reference condition, so they cannot be used too far from it: to cover the full flight envelope a large number of LTI models is required, leading to high flight testing costs. A LPV model stitches a group of LTI models together into one continuous model that represents the system. The model stitching architecture adopted in this work is presented in [71] and it is briefly discussed in the following.

The starting point is a set of LTI models and relative trim and control values for different values of the scheduling parameter ρ (in case of multiple scheduling parameters ρ is a vector). It is important that ρ spans all the aircraft envelope: for example, if $\rho = [v, h]^T$, it has to span from the minimum to the maximum speeds and altitudes. In this way the whole flight envelope can be modeled with the LPV

model. The set of LTI models, obtained both by identification of experimental data or by linearization of a more complicated model, makes up a grid of points called anchor points. The scheduling parameter in the anchor point is known and assumes the value ρ_0 . The LTI systems are in the form:

$$\dot{x} = A|_{\rho_0}x + B|_{\rho_0}u \quad (6.1)$$

$$y = C|_{\rho_0}x + D|_{\rho_0}u \quad (6.2)$$

with $A|_{\rho_0}$, $B|_{\rho_0}$, $C|_{\rho_0}$ and $D|_{\rho_0}$ state space system matrices, $x = X - X_0$ perturbation of the state vector around the trim condition X_0 , $y = Y - Y_0$ output perturbation and $u = U - U_0$ input perturbation. The system matrices are referred to the scheduling parameter ρ_0 corresponding to the anchor point. To build the LPV model the data of all the LTI systems are interpolated over the grid and then evaluated for the instantaneous value of the scheduling parameter ρ . The obtained LPV model is written as:

$$\dot{x} = A|_{\rho}(X - X_0|_{\rho}) + B|_{\rho}(U - U_0|_{\rho}) \quad (6.3)$$

$$y = C|_{\rho}(X - X_0|_{\rho}) + D|_{\rho}(U - U_0|_{\rho}). \quad (6.4)$$

As stated both in [71] and [72], the contribution of stability derivatives with respect to state variables which are in the scheduling vector is nulled out since the variation of such parameters with respect to their instantaneous values is zero. This is better explained with an example: in the case in which $\rho = u$, with u horizontal velocity in body axes, the derivatives of horizontal and vertical forces with respect to u , called respectively X_u and Z_u , and the derivative of the pitching moment with respect to u , M_u , are always multiplied by $u - u_0|_{\rho}$. Since $u_0|_{\rho} = u$, then X_u , Z_u and M_u are always multiplied by zero, so their contribution is lost. As pointed out in [72], the contribution of these stability derivatives is preserved in the variations of trim states and inputs with respect to the scheduling parameter. Two possible stitching approaches have been shown in [71] and [72]:

- explicit model stitching, presented in Figure 6.1: the scheduling parameter is fixed externally (*i.e.*, the flight condition is externally imposed), thus the effect of the trim variables is not considered;
- implicit model stitching, presented in Figure 6.2: the loop is closed and the effect of the trim variables is considered inside the model.

In this work only the explicit model stitching approach has been adopted since its implementation is easier.

When the stitched model has been built, it is verified against the grid points; then it is possible to validate it against other trim conditions different from the anchor points obtained from the initial source of LTI models (identification or more complicated model). After passing these checks, the LPV model can be used for control and simulation purposes.

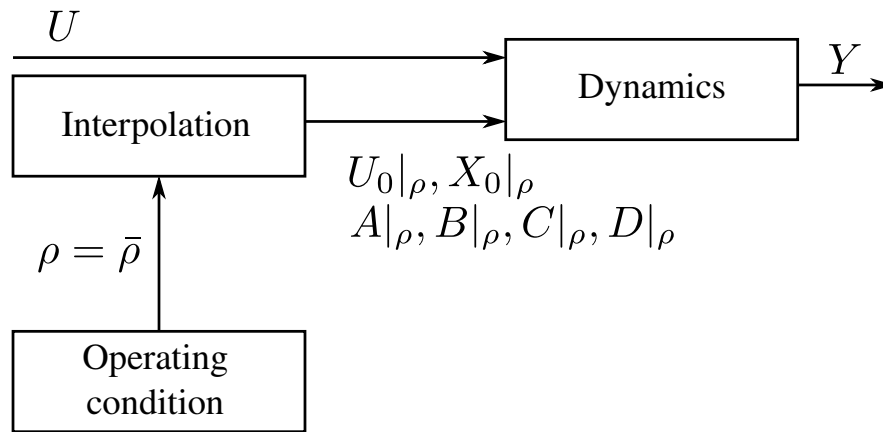


Figure 6.1: Explicit model stitching architecture.

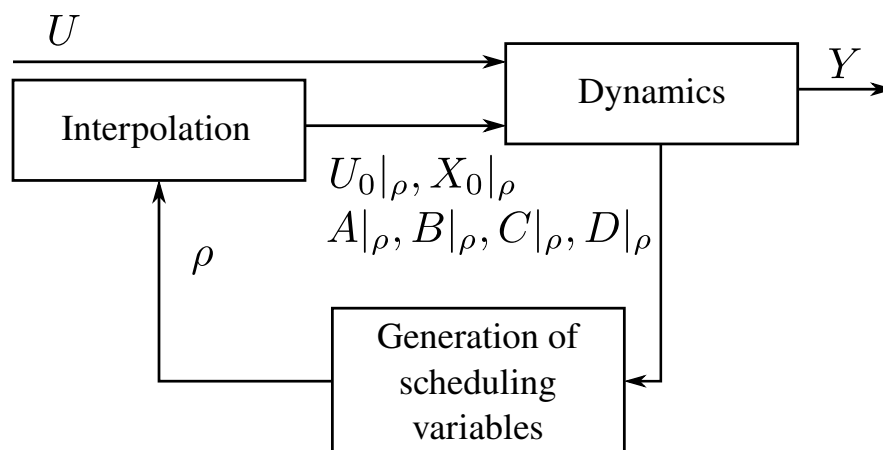


Figure 6.2: Implicit model stitching architecture.

6.2 LPV model implementation

The first step performed is the selection of the scheduling parameter/parameters. References [72], which develops the LPV models of an helicopter, selects horizontal speed, vertical speed, altitude and sideslip angle as scheduling parameters. In the case at hand most of them can be neglected given the operating conditions of the UAV: the flight altitude range is narrow, limited by the EU regulations for unmanned aerial vehicles ([17] and [18]) so it is useless to consider different flight altitudes; the vertical speed can also be neglected since the aircraft is intended to climb and descend in vertical flight mode and to cruise more or less at constant altitude; last but not least the sideslip angle is neglected because of little interest in such an aircraft. Therefore, the selected scheduling parameter is the flight speed. The whole speed range is considered, starting from the stall speed v_s to the maximum speed v_{max} : the interval goes from 11 m/s to 22 m/s, so it is divided into twelve points separated by 1 m/s. Six points will be used as anchor points for the grid, the other six for the validation procedure. The two sets of points are:

- grid set: 11 m/s, 13 m/s, 15 m/s, 17 m/s, 19 m/s and 22 m/s;
- validation set: 12 m/s, 14 m/s, 16 m/s, 18 m/s, 20 m/s, 21 m/s.

After the selection of the scheduling parameter it is important to collect the LTI models. It has been decided to use LTI models that represent the aircraft in horizontal steady level flight conditions. As presented in [70], the equations of motion of an aircraft in this condition can be written decoupling the longitudinal motion from the lateral one. In this way two state space systems are obtained:

- longitudinal dynamics, with state vector $[u, w, q, \theta]^T$ and input vector $[\delta_e, \delta_p]^T$;
- lateral dynamics, with state vector $[v, p, r, \phi]^T$ and input vector $[\delta_a, \delta_r]^T$;

with u horizontal speed, v lateral speed, w vertical speed, p roll rate, q pitch rate, r yaw rate, θ pitch angle, ϕ roll angle, δ_e elevator deflection, δ_p throttle percentage, δ_a aileron deflection and δ_r rudder deflection. Both the longitudinal and the lateral equations of motion are written in stability axes, *i.e.*, a body axes reference frame with the x axis aligned to the direction of the speed vector $V = [u, v, w]^T$ at the moment of the trim. The longitudinal dynamics state space system is:

$$\begin{pmatrix} \Delta \dot{u} \\ \dot{w} \\ \dot{q} \\ \Delta \dot{\theta} \end{pmatrix} = \begin{bmatrix} \frac{X_u}{m} & \frac{X_w}{m} & 0 & -g \cos \theta_0 \\ \frac{Z_u}{m-Z_{\dot{w}}} & \frac{Z_w}{m-Z_{\dot{w}}} & \frac{Z_q+mu_0}{m-Z_{\dot{w}}} & -\frac{mg \sin \theta_0}{m-Z_{\dot{w}}} \\ \frac{1}{I_y} \left(M_u + \frac{M_{\dot{w}} Z_u}{m-Z_{\dot{w}}} \right) & \frac{1}{I_y} \left(M_w + \frac{M_{\dot{w}} Z_w}{m-Z_{\dot{w}}} \right) & \frac{1}{I_y} \left(M_q + \frac{M_{\dot{w}} (Z_q+mu_0)}{m-Z_{\dot{w}}} \right) & -\frac{M_{\dot{w}} mg \sin \theta_0}{I_y (m-Z_{\dot{w}})} \\ 0 & 0 & 1 & 0 \end{bmatrix} \begin{pmatrix} \Delta u \\ w \\ q \\ \Delta \theta \end{pmatrix} + \begin{bmatrix} \frac{X_{\delta_e}}{m} & \frac{X_{\delta_p}}{m} \\ \frac{Z_{\delta_e}}{m-Z_{\dot{w}}} & \frac{Z_{\delta_p}}{m-Z_{\dot{w}}} \\ \frac{M_{\delta_e}}{I_y} + \frac{M_{\dot{w}} Z_{\delta_e}}{I_y (m-Z_{\dot{w}})} & \frac{M_{\delta_p}}{I_y} + \frac{M_{\dot{w}} Z_{\delta_p}}{I_y (m-Z_{\dot{w}})} \end{bmatrix} \begin{pmatrix} \Delta \delta_e \\ \Delta \delta_p \end{pmatrix} \quad (6.5)$$

while the lateral dynamics state space system is

$$\begin{pmatrix} \dot{v} \\ \dot{p} \\ \dot{r} \\ \dot{\phi} \end{pmatrix} = \begin{bmatrix} \frac{Y_v}{m} & \frac{Y_p}{m} & \frac{Y_r}{m} - u_0 & g \cos \vartheta_0 \\ \frac{L_v}{I'_x} + I'_{zx} N_v & \frac{L_p}{I'_x} + I'_{zx} N_p & \frac{L_r}{I'_x} + I'_{zx} N_r & 0 \\ I'_{zx} L_v + \frac{N_v}{I'_z} & I'_{zx} L_p + \frac{N_p}{I'_z} & I'_{zx} L_r + \frac{N_r}{I'_z} & 0 \\ 0 & 1 & \tan \vartheta_0 & 0 \end{bmatrix} \begin{pmatrix} v \\ p \\ r \\ \phi \end{pmatrix} + \begin{bmatrix} \frac{Y_{\delta_a}}{m} & \frac{Y_{\delta_r}}{m} \\ \frac{L_{\delta_a}}{I'_x} + I'_{zx} N_{\delta_a} & \frac{L_{\delta_r}}{I'_x} + I'_{zx} N_{\delta_r} \\ I'_{zx} L_{\delta_a} + \frac{N_{\delta_a}}{I'_z} & I'_{zx} L_{\delta_r} + \frac{N_{\delta_r}}{I'_z} \\ 0 & 0 \end{bmatrix} \begin{pmatrix} \Delta \delta_a \\ \Delta \delta_r \end{pmatrix}. \quad (6.6)$$

The X_k terms in equation (6.5) represent the derivatives with respect to the k -th state or control input of the force acting on the x direction (where k can be u , w , q , δ_e or δ_p); the same notation applies also to the force in z direction Z , and to the pitching moment M . The term I_y is the inertia about the y axis, while m represents the aircraft mass. The same notation is used also in equation (6.6); in this case the derivatives of the y force Y , of the rolling moment L and of the yawing moment N are performed with respect to the lateral states v , p , r and to the lateral inputs δ_a and δ_r . The terms I'_x , I'_z and I'_{zx} are a combination of the aircraft inertias, namely:

$$I'_x = \frac{I_x I_z - I_{zx}^2}{I_z}, \quad (6.7)$$

$$I'_z = \frac{I_x I_z - I_{zx}^2}{I_x}, \quad (6.8)$$

$$I'_{zx} = \frac{I_{zx}}{I_x I_z - I_{zx}^2}. \quad (6.9)$$

The terms with subscript 0 represent the values in trim conditions. The perturbation symbol Δ is dropped if the trim variable is zero to simplify the notation, as done in [70]: $w_0 = q_0 = v_0 = p_0 = r_0 = \phi_0 = 0$ so these states are written without the Δ .

XFLR5 has been used to produce the LTI models in the anchor points and in the validation ones, even if the procedure to obtain the complete state space system is a bit cumbersome. XFLR5 follows the theory explained in [70], so the final output of the software can be directly used to build the LPV model. As mentioned in Section 6.1, the LTI models have to be produced from identification of flight data or from linearization of a more complicated model; at the time of this work none of these options is available for the VTOL UAV, so it has been decided to use LTI models from XFLR5, even if it produces low fidelity models, since it is computationally cheap and the state space matrices and trim inputs and states can be easily obtained for an arbitrarily thick grid of the scheduling parameter. Given that the complete procedure to get the LTI models with all the control inputs is not clearly presented in [69] and it has been reconstructed thanks to the online XFLR5 community, it is considered useful to present it briefly in the following.

The first step is to build the 3D model of the aircraft with no control surface deflected; then a stability analysis has to be performed with the elevator as control input. In this way several trim conditions are found: a different trim speed is found for each elevator deflection in the imposed range. The elevator deflections corresponding to the desired trim speeds have to be noted, then a new 3D aircraft model has to be built for each trim speed, setting the elevator with the corresponding deflection. At this point, the stability analysis of each aircraft model produces the longitudinal and lateral state matrices and the first column of the longitudinal control matrix. Two new models have to be produced for each trim speed to obtain the lateral control matrix: one with the aileron deflected and the other with the rudder deflected. The stability analysis with these two models has to be performed with the deflected control surface as control input and its deflection has to be complementary to the one in the 3D model (*i.e.*, if the 3D model has aileron deflected of $+5^\circ$, the control input has to be -5° so that the trim condition is the same as neutral aileron). At this point only the second column of the longitudinal control matrix is missing; this is because XFLR5 is designed for sailplanes only, so it does not model the propulsion.

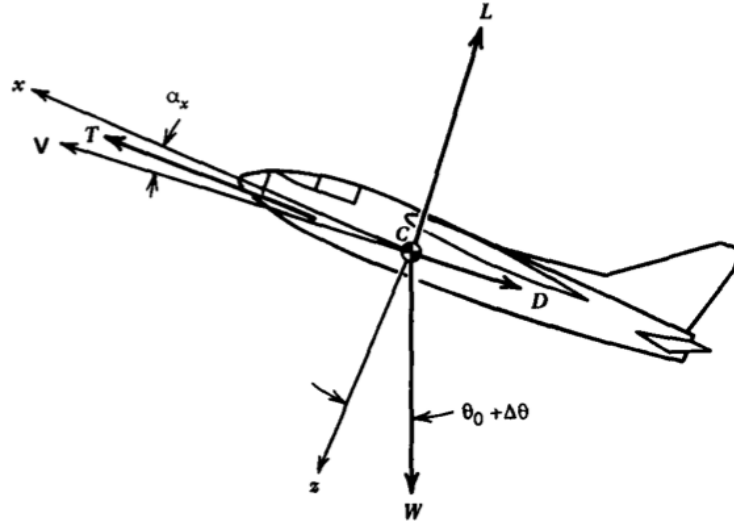


Figure 6.3: Forces in symmetric flight, source [70].

The propulsive force produces effects in the longitudinal plane, so it affects only equation (6.5). According to [70], if the propulsive force is aligned with the body axis, and this is the case of the VTOL UAV, then it contributes only to the horizontal force X , as it can be seen in Figure 6.3. Moreover, [70] states that X_w does not depend on the propulsion, so the only coefficient inside the longitudinal state matrix affected by the absence of propulsion inside the XFLR5 model is the derivative X_u . The horizontal force X has a large contribution related to the drag D ; since XFLR5 does not model the fuselage and the engine booms, the drag is underestimated, as shown also in Section 5.4. Given that, it has been considered of little help to recover the contribution of the propulsion to X_u while neglecting the drag one.

Instead, it has been decided to recover the propulsion contribution to the longitudinal control matrix with a custom procedure. The column to be computed is

$$\begin{bmatrix} \frac{X_{\delta_p}}{m} \\ \frac{Z_{\delta_p}}{m - Z_{\dot{w}}} \\ \frac{M_{\delta_p}}{I_y} + \frac{M_{\dot{w}} Z_{\delta_p}}{I_y (m - Z_{\dot{w}})} \\ 0 \end{bmatrix}. \quad (6.10)$$

Considering that the vertical distance between the x body axis and the engine axis is very small, as presented in Subsection 4.1.2, the term M_{δ_p} can be neglected. Also $M_{\dot{w}}$ and $Z_{\dot{w}}$ are very small, as stated in [69], so they can be neglected as well.

The resulting column of the longitudinal control matrix is:

$$\begin{bmatrix} \frac{X_{\delta_p}}{m} \\ \frac{Z_{\delta_p}^n}{m} \\ 0 \\ 0 \end{bmatrix}. \quad (6.11)$$

The data of the thrust as function of the throttle has been taken from the engine manufacturer website (reference [56]); it is presented in Figure 6.4. From this data it has been possible to compute T_{δ_p} , the thrust derivative with respect to the throttle input and the trim value of δ_p , once the required thrust is known. The propulsive force has been decomposed in stability axes following the scheme in Figure 6.5. The resulting terms are:

$$X_{\delta_p} = T_{\delta_p} \cos(\alpha_w - i_w) \quad (6.12)$$

$$Z_{\delta_p} = -T_{\delta_p} \sin(\alpha_w - i_w), \quad (6.13)$$

with α_w angle between the velocity vector and the *MAC* line (the model in XFLR5 includes only the lifting surfaces, so α_w is the angle of attack from the software) and i_w wing incidence, known from the aircraft geometry.

As already stated, XFLR5 model does not include the fuselage and the engines, so their drag contribution is not taken into account. Since the required thrust is computed applying the horizontal force equilibrium in trim,

$$T = D, \quad (6.14)$$

the T computed based on XFLR5 data is incorrect. Then, also the δ_p , X_{δ_p} and Z_{δ_p} computed with the just presented procedure are incorrect (or at least underestimated since XFLR5 drag is inferior to the real one). Two possible options are available: 1) neglect completely the propulsion contribution and complete the LPV model when a better drag estimate will be available or 2) include a drag contribution to account for the fuselage and the engines. The latter option is preferable since it allows to complete the LPV model and use it for the preliminary design of flight controllers. The drag contribution cannot be computed using the empirical procedures in [42] and [43], as mentioned in Section 5.4. However, it can be computed starting from the parabolic drag polar presented in the same section: the difference between the analytical drag polar based on the procedure from [21] and the one from XFLR5, namely

$$\Delta C_D = C_{D_0}^{analytical} - C_{D_0}^{XFLR5}, \quad (6.15)$$

can be added to the drag coefficients from XFLR5 used in the LPV model. It is certainly a rough correction (it is constant with the speed and probably overestimated) but it allows to obtain a complete LPV model. The drag increment is

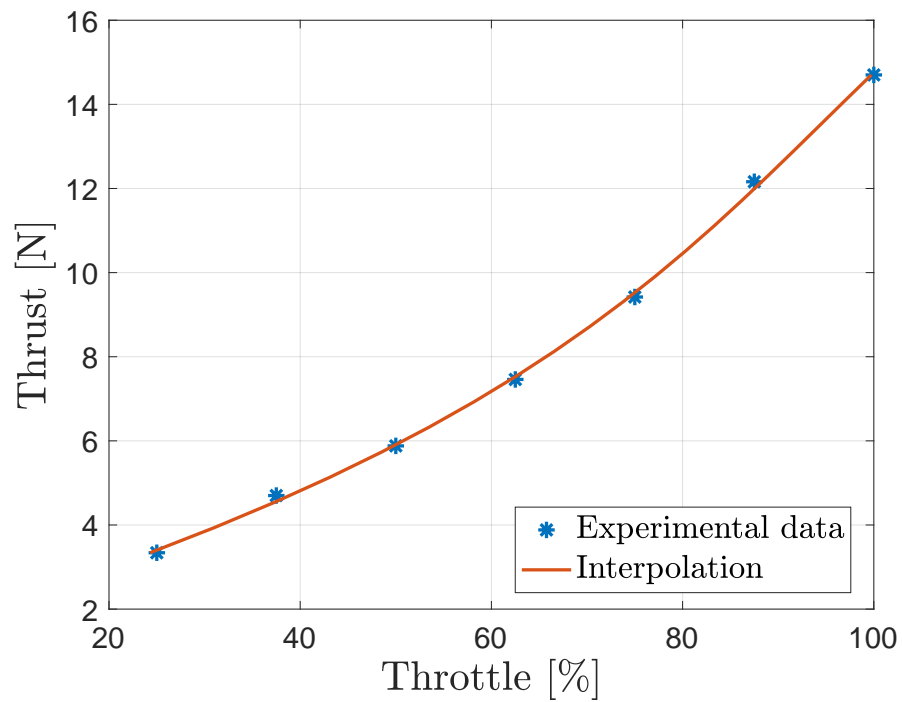


Figure 6.4: Horizontal flight engines thrust as function of the throttle percentage (the values presented are related to the overall thrust output of both FF motors); data from the manufacturer ([56]).

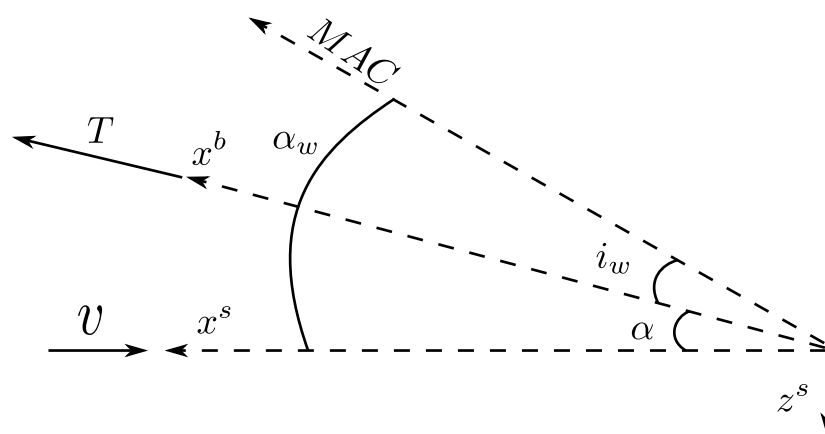


Figure 6.5: Force scheme for the propulsion decomposition in stability axes.

$\Delta C_D = 0.035$. In the future a more accurate aerodynamic analysis will have to be done to improve this aspect of the LPV model.

The last element that has to be discussed in this section are the interpolation techniques adopted to stitch together the LTI model coefficients. Starting from [72], two different methods have been employed: a polynomial interpolation has been used for the matrices coefficients while a spline interpolation has been adopted for the trim values of states and control inputs. The order of the interpolating polynomial has been found with an iterative procedure: starting from order zero, at each step the root mean square error

$$RMSE = \sqrt{\frac{\sum_{i=1}^N (x_i - \bar{x}_i)^2}{N}} \quad (6.16)$$

is evaluated substituting to x the interpolated coefficient and to \bar{x} the grid value of the same coefficient (in this case the number of elements N is equal to 1). If the $RMSE$ is superior to a tolerance of 1×10^{-4} , the interpolating polynomial order is increased. A maximum order equal to 3 is set to prevent numerical problems and overfitting in polynomial interpolation. The trim values, instead, are interpolated with cubic splines.

6.3 LPV model verification and validation

It is now time to analyze the result of the model stitching procedure. As mentioned in the chapter introduction, the results check have been performed in two stages: first the model has been verified in the grid points, then it has been validated in the second set of points obtained from XFLR5. Both for verification and validation, as done in [71], some stability and control derivatives and some trim values have been compared between LPV model and LTI models. Moreover, a frequency domain comparison has been carried out. Considering equation (6.5) and equation (6.6), the following quantities have been computed:

- longitudinal dynamics: $X_u, Z_u, Z_{\delta_e}, \delta_e, \delta_p$ and θ ;
- lateral dynamics: Y_v, Y_p, Y_{δ_a} and Y_{δ_r} .

The frequency domain responses are computed, for the longitudinal dynamics, considering the elevator deflection as input and the pitch rate as output. For the lateral dynamics, instead, two frequency responses have been computed: one with the aileron deflection as input and the roll rate as output, the other with the rudder as input and the yaw rate as output. The frequency responses have been computed for all the velocities in the speed range. Figure 6.6 and Figure 6.7 present, as example, the frequency responses for the cruise speed of 15 m/s (one of the verification points). Figure 6.8 and Figure 6.9 show the stability and

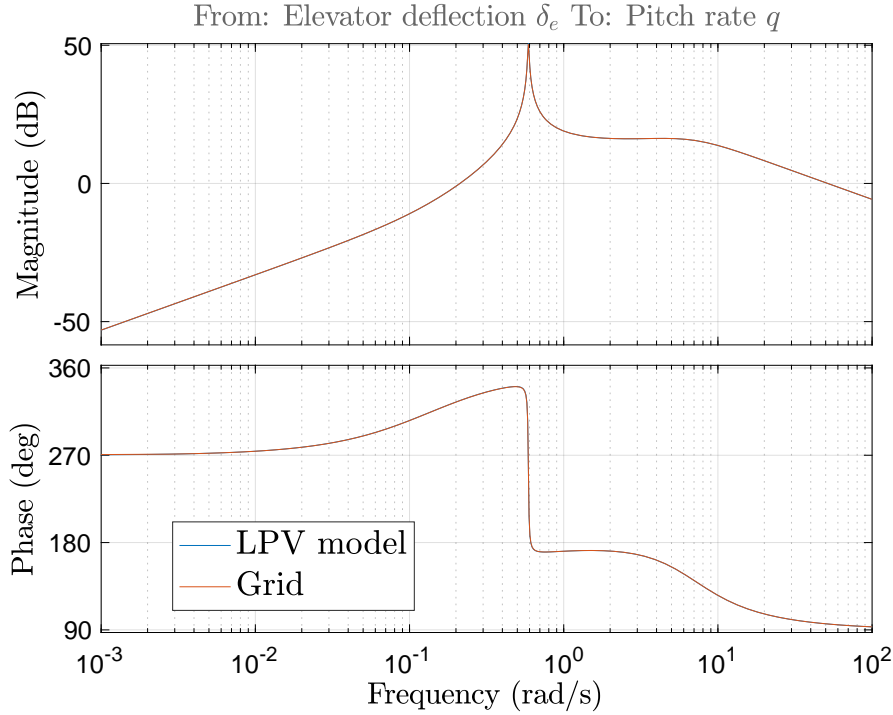
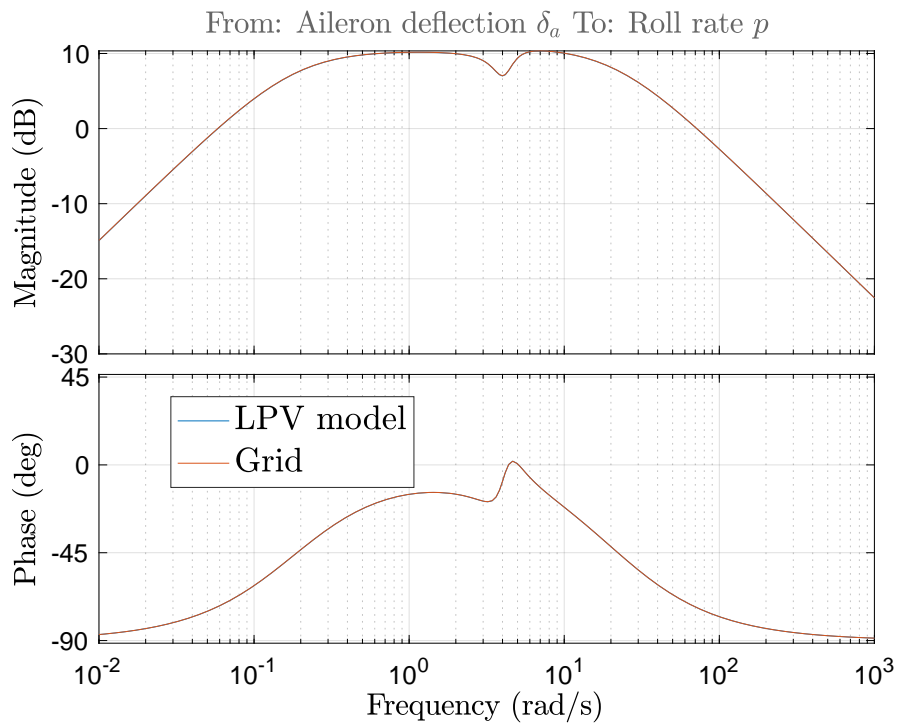


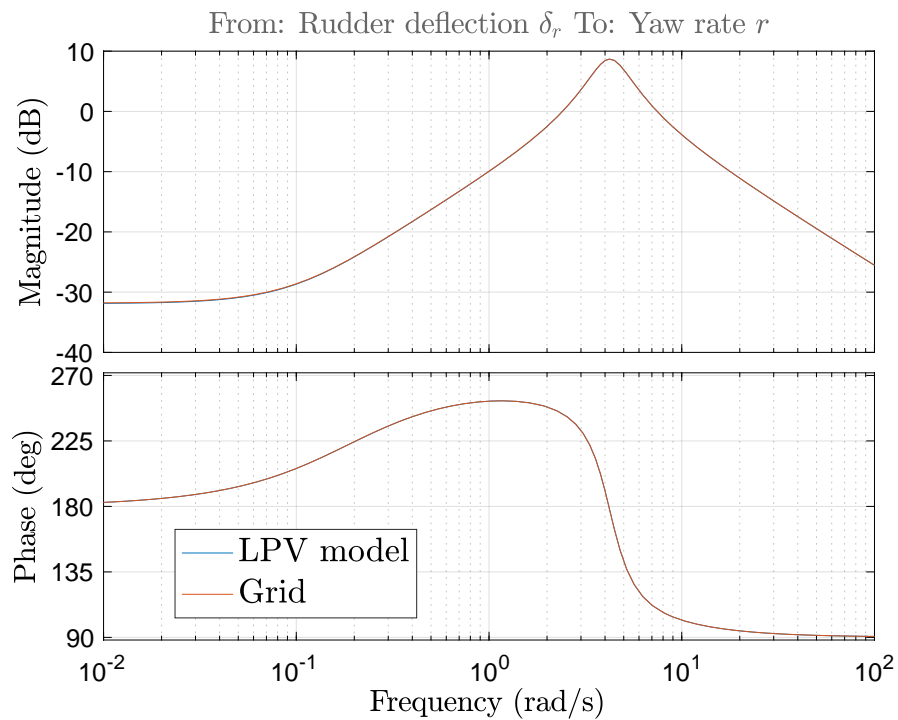
Figure 6.6: Longitudinal dynamics frequency response: from elevator deflection to pitch rate. The frequency response is performed in cruise conditions.

control derivatives and the trim values in the verification and validation points. It is worth making some comments about the propulsion modeling: as it can be seen from Figure 6.8f, the throttle curve as function of the airspeed presents a reasonable and familiar trend (as shown in Figure 6.4 there is an almost-linear relation between throttle and thrust). Looking better at Figure 6.8f, however, it is clear that at maximum speed ($v_{max} = 22$ m/s) not all the engines capabilities are fully exploited (55% of the throttle only). This is coherent with the FF engine selection performed in Subsection 4.1.2 and the data presented in Table 4.2: the motors have been selected to achieve the power required to fly at v_{max} , called P_b^{FF} , at most at 75% of the throttle since P_b^{FF} has to be supplied for a continuous time, not for few seconds. Moreover, since the cruise speed $v_{cr} = 15$ m/s requires more or less 30% of the throttle when both FF motors work, it has been accepted to adopt an oversized engine type to account for the possibility of one engine inoperative situations: if one motor stops working the other can supply the whole thrust required for the cruise to continue.

Both the verification and the validation plots show that the LPV model can reproduce with high fidelity the dynamic behavior of the system: the model stitching procedure produces good results. To increase the accuracy of the LPV model, however, it is mandatory to increase the accuracy of the initial LTI models: in the future a better estimate of the drag have to be performed (or by testing of a



(a) Lateral dynamics frequency response: from aileron deflection to roll rate.



(b) Longitudinal dynamics frequency response: from rudder deflection to yaw rate.

Figure 6.7: Frequency domain responses in cruise speed conditions.

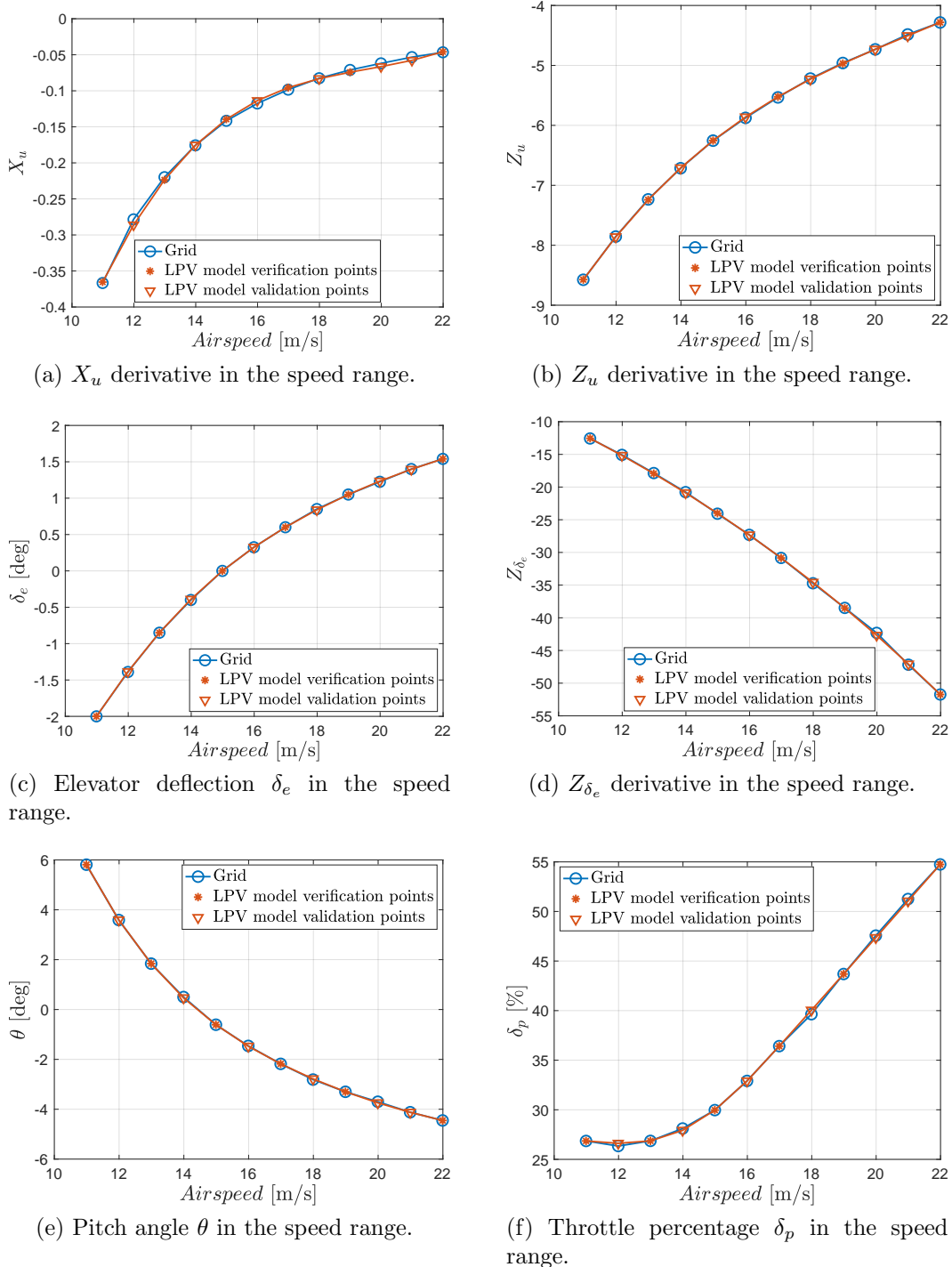


Figure 6.8: Longitudinal dynamics quantities in verification and validation points.

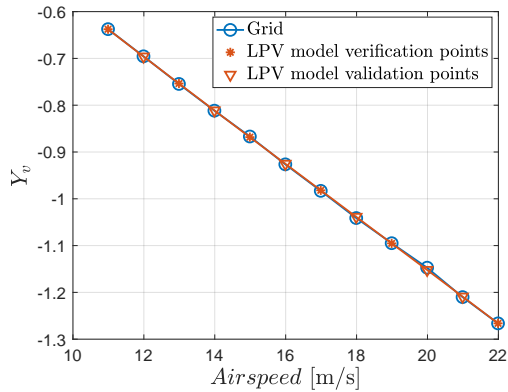
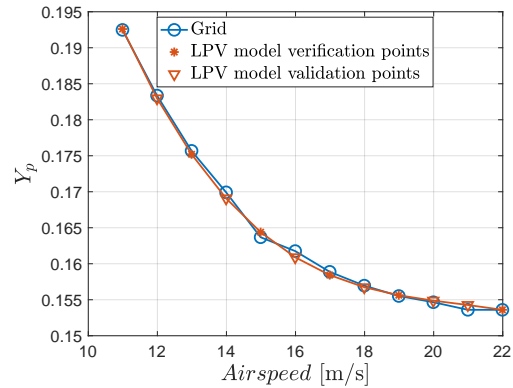
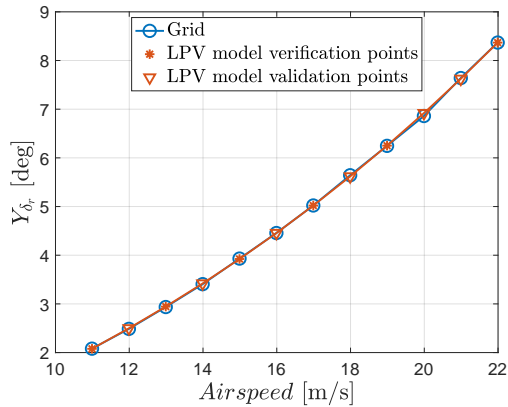
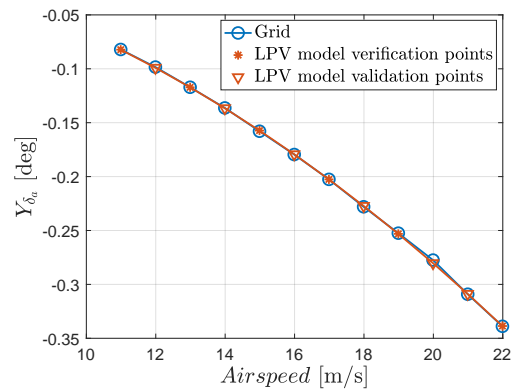
(a) Y_v derivative in the speed range.(b) Y_p derivative in the speed range.(c) Y_{δ_r} derivative in the speed range.(d) Y_{δ_a} derivative in the speed range.

Figure 6.9: Lateral dynamics quantities in verification and validation points.

real model or by CFD analysis of the CAD model); in this way a better estimate of the propulsion contribution can be included to the model. Anyway, a method to recover its contribution has been developed and the actual LPV model can be used to design the initial controller of the horizontal flight mode. These controllers have to be fine tuned when a better model will be developed.

Conclusions

In the thesis a VTOL UAV has been designed and its dynamical model has been developed. In particular, the aircraft has been designed with the aim of prototyping it; as already mentioned in the Introduction, however, this last step has not been possible due to the COVID-19 pandemic.

In detail, the conceptual and preliminary design phases have been carried out: the outputs have been the aircraft configuration and the first numerical information (take-off weight W_{TO} , wing surface S and required power P_b both for forward and vertical flight phases). Next the UAV has been designed in all its aspects: the aerodynamics of wing and tail, the structural layout and the practical manufacturing aspects, the onboard systems, the propulsion units (two separate sets of electric motors for horizontal and vertical flight given the VTOL nature of the UAV and the selected configuration) and the fuselage. In particular, much attention has been paid to the fuselage, since it is the center of the aircraft and allows to reach two initial requirements: the possibility to easily remove and change the wings and the disassembly of the aircraft to transport it in a compact volume. Moreover, it has been decided to 3D print the fuselage in SLS nylon; this decision has unlocked many design possibilities: the ability to design a fuselage that suits perfectly the internal components and the motor booms, the possibility to remove the fuselage cover to access the internal space, the custom-designed locking mechanisms for the engine booms.

Since the main result of the thesis is the VTOL UAV (besides the design procedure developed and its implementation in a Matlab code to speed up future designs), it is important to summarize here the final aircraft specifications and to present the technical drawings of the UAV: Table 6.1 presents the numerical values that describes the aircraft while Figure 6.10 shows the technical drawings of the UAV and its dimensions. Comparing the values of Table 6.1 to the preliminary values computed in Chapter 1, it can be seen that the take-off weight W_{TO} is larger (4.8 kg_f instead of the initial 4.4 kg_f) and also the wing surface S is slightly larger (0.56 m² instead of the initial 0.51 m²) than the preliminary values. The increase in weight is mainly related to the fuselage since the 3D printed fuselage is not fully optimized from a structural point of view; moreover, the initial estimate of the structural weight is based on a database of competitors composed largely of composite-made UAVs and the designed VTOL UAV is not a composite-made

Parameter	Value
W_{TO} [kgf]	4.8
MTOW x_{CG} [m]	0.1
Wing span [m]	2.25
Wing surface [m ²]	0.56
MAC [m]	0.25
Wing airfoil	Selig 2046
Tail airfoil	NACA 0008
λ	1
Γ [deg]	0
Λ [deg]	0
Number of VF motors	8
Number of FF motors	2
Battery capacity [mAh]	8500
Flight control unit	Pixhawk 4

Table 6.1: Summary of design parameters. The position of CG is computed from the nose of the aircraft fuselage.

aircraft. The increase in wing surface is due to the fact that the mean aerodynamic chord has been increased when the taper ratio has been changed in the final phases of the design due to technological constraints in the manufacturing facility. A final remark has to be done about the payload: a payload weight W_{pl} of 200 g_f has been included in the preliminary design phase; after this first design phase W_{pl} has been neglected since, up to now, it has not been decided precisely what this payload is (it depends on the research activities for which the UAV will be used in the future). However, it has been considered in the fuselage design in order to preserve a space for it. In the aircraft specifications of Table 6.1, W_{pl} is not included inside the take-off weight.

The developed LPV model of the UAV reproduces well the aircraft behavior in the full speed range. The propulsion contribution, neglected in the LTI models from XFLR5 used to build the LPV one, has been included starting from engines data from the manufacturer; however, this contribution is not accurate due to a low fidelity model of the aerodynamic drag, which leads to inaccurate thrust computation.

The results obtained present some limitations:

- there is no detailed structural analysis of the fuselage, so its actual design is a bit conservative, based on Southampton University UAVs ([16]): a better knowledge of the structural behavior of 3D printed components would allow to optimize the fuselage structure with clear benefits for the whole aircraft;
- the aerodynamic analysis is in some ways limited by the fact that no fuse-

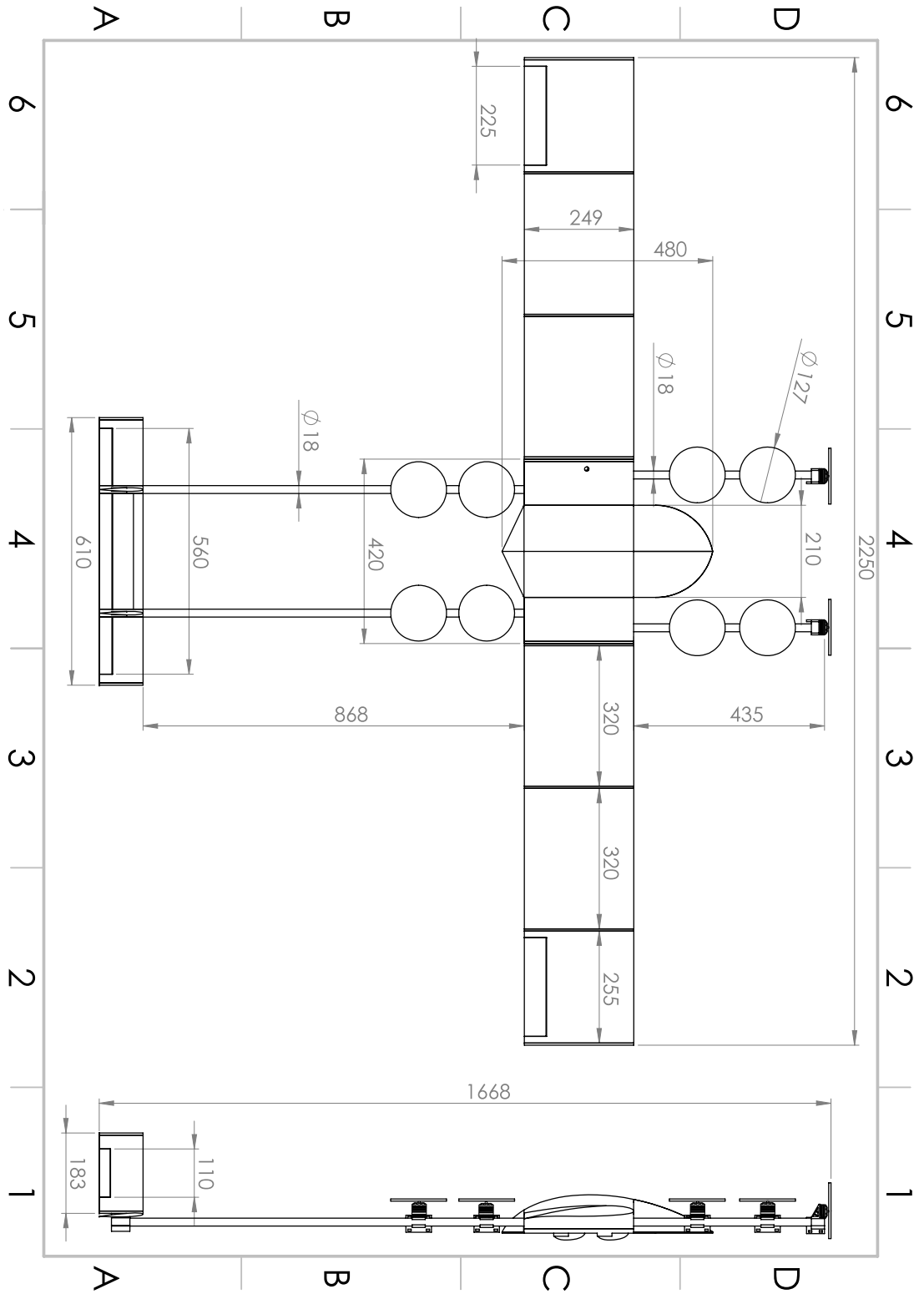


Figure 6.10: Technical drawings of the VTOL UAV, scale 1:10. The measurements are given in mm.

lage and engine booms have been considered in the XFLR5 aerodynamic model: the obtained parabolic drag polar is really different from the initial analytical estimate (which, is important to say, is only an estimate based on the competitors and not a standard to be matched); a better aerodynamic model would have shown how good is the initial analytical method in estimating the aircraft preliminary aerodynamic characteristics;

- no performance analysis has been carried out to check the results of the design in terms of range and endurance; this is due to the not accurate parabolic drag polar estimate. It has to be stated, however, that the battery installed has higher capacity than the required one, so the endurance should meet or exceed the initial target;
- the LPV model is accurate in its implementation, however it is based on the only available LTI models: they are obtained from XFLR5 and not from a more complicated model, as suggested in [71] and [72].

Starting from the obtained results and from their limitations, lots of future activities connected with this thesis can be found:

- the first is obviously the final manufacturing of the UAV; the technical drawings are ready and a large part of the components has already been bought. The wing, the tail and the fuselage have to be produced, then all the internal components have to be integrated and the on board flight software have to be adapted from previous versions developed by ASCL.
- Given the obligatory stop due to the pandemic, it could be useful to improve the modeling accuracy of the aircraft aerodynamics: the panel methods employed in XFLR5 for the preliminary and detailed design are acceptable for first design stages; it could be useful to model the whole aircraft with the fuselage and the motor booms. A CFD analysis would increase the accuracy of the drag estimation with benefits for the design and the LPV model.
- The produced aircraft has to be tested in flight to check the design results and the already performed flight dynamics analysis. Moreover, a flight testing experience allows to check the real performance of the UAV and to produce an identified model. This model from data identification can be compared to the already developed LPV one from XFLR5: in this way it is possible to asses the suitability of XFLR5 as preliminary design tool for future projects.
- As mentioned in Chapter 4, there is room for improvement for the SLS 3D printed fuselage: the structural properties of the material can be studied in detail, allowing to optimize further the fuselage shape. An optimized fuselage allows to reduce the weight and the cost of the aircraft.

-
- Last but not least, the developed Matlab code for preliminary design can be improved to be more flexible and integrated. In this way a tool for the preliminary design of a VTOL UAV (computation of W_{TO} , S , P_b^{FF} and P_b^{VF}) and aerodynamic and structural design will be available for future aircraft projects.

Bibliography

- [1] D. Molloy and J. Copestake. *Drone-to-door medicines trial takes flight in Ireland*. (Visited on 05/05/2020).
- [2] J. Porter. *Alphabet's nascent drone delivery service is booming*. (Visited on 05/05/2020).
- [3] W. Yoo, E. Yu, and J. Jung. "Drone delivery: factors affecting the public's attitude and intention to adopt". In: *Telematics and Informations* 35 (May 2018), pp. 1687–1700.
- [4] Wingcopter press office. *Wingcopter secures further investment from Corecam*. (Visited on 05/05/2020).
- [5] Wingcopter press office. *UPS Flight Forward and Wingcopter to develop versatile new drone fleet*. (Visited on 05/05/2020).
- [6] *Wing Aviation LLC website*. URL: <https://wing.com>.
- [7] J. Porter. *Alphabet's Wing drones get FAA approval to make deliveries in the US*. (Visited on 05/05/2020).
- [8] *Amazon Prime Air website*. URL: <https://www.amazon.com/Amazon-Prime-Air/b?ie=UTF8&node=8037720011>.
- [9] *Wingcopter website*. URL: <https://wingcopter.com>.
- [10] *Wingtra AG website*. URL: <https://wingtra.com>.
- [11] M. Tyan et al. "Comprehensive preliminary sizing/resizing method for a fixed wing-VTOL electric UAV". In: *Aerospace Science and Technology* 71 (Sept. 2017), pp. 30–41.
- [12] R. Czyba et al. "Construction, prototyping, flight dynamics modeling and aerodynamic analysis of hybrid VTOL unmanned aircraft". In: *Journal of advanced transportation* 2018 (2018).
- [13] M. Hochstenbach et al. "Design and control of an unmanned aerial vehicle for autonomous delivery with transition from vertical take-off to forward flight: VertiKUL, a quadcopter tailsitter". In: *International Journal of Micro Air Vehicles* 7.4 (2015), pp. 395–405.

-
- [14] H. Gu et al. “Development and experimental verification of a hybrid vertical take-off and landing (VTOL) unmanned aerial vehicle (UAV)”. In: *International conference on unmanned aircraft systems (IUCAS)*. June 2017, pp. 160–169.
- [15] *SOTON website*. URL: <https://www.sotonuav.uk>.
- [16] A. J. Keane, A. Sobester, and J. P. Scanlan. *Small unmanned fixed-wing aircraft design: a practical approach*. Aerospace Series. John Wiley and Sons, Ltd., 2017.
- [17] “Commission Delegated Regulation (EU) 2019/945”. In: vol. Official Journal L 152. Mar. 2019, pp. 1–40.
- [18] “Commission Implementing Regulation (EU) 2019/947”. In: vol. Official Journal L 152. May 2019, pp. 45–71.
- [19] *NATO standard AEP-83: light unmanned aircraft system airworthiness requirements*. Allied Engineering Publications. Nato standardization agency, 2014.
- [20] *MIL F 8785 C. Military Specification: Flying Qualities of Piloted Airplanes*. United States Department of Defense, 1980.
- [21] J. Gundlach. *Designing unmanned aircraft systems: a comprehensive approach*. Ed. by J. A. Schetz. AIAA education series. American Institute of Aeronautics and Astronautics, Inc., 2012.
- [22] M. H. Sadraey. *Aircraft design: a system engineering approach*. Aerospace Series. John Wiley and Sons, Ltd., 2013.
- [23] S. Gudmundsson. *General aviation aircraft design: applied methods and procedures*. Butterworth-Heinemann, 2014.
- [24] F. Cakici and M. K. Leblebicioglu. “Analysis of a UAV that can hover and fly level”. In: *MATEC web of conferences* 59.07010 (2016).
- [25] Y. Zhou, H. Zhao, and Y. Liu. “An evaluative review of the VTOL technologies for unmanned and manned aerial vehicles”. In: *Computer Communications* 149 (2020), pp. 356–369.
- [26] *Quantum Systems website*. URL: <https://www.quantum-systems.com>.
- [27] *Vertical Technologies website*. URL: <https://www.deltaquad.com>.
- [28] *Kapetair website*. URL: <http://kapetair.com>.
- [29] *Sunbirds Aero website*. URL: <https://sunbirds.aero>.
- [30] *Flytech UAV website*. URL: <https://www.flytechuav.com>.
- [31] *Krossblade Aerospace website*. URL: <https://www.krossblade.com>.
- [32] *Heliceo website*. URL: <http://www.heliceo.com/en/home/>.
- [33] *ZeroTech website*. URL: <https://www.zerotech.com>.

-
- [34] *Avy website*. URL: <https://www.avy.eu>.
- [35] *Drone America website*. URL: <http://www.droneamerica.com>.
- [36] *Threod Systems website*. URL: <https://threod.com>.
- [37] *Autel Robotics website*. URL: <https://auteldrones.com>.
- [38] *Tareq UAV website*. URL: <http://tarequav.com/en/>.
- [39] *TTA-America website*. URL: <https://www.tta-america.com>.
- [40] *Sparkle Tech Limited website*. URL: <http://www.sparkletech.hk>.
- [41] *UAV Factory Ltd website*. URL: <https://www.uavfactory.com>.
- [42] J. Roskam. *Airplane design*. DAR Corporation, 1985.
- [43] D. P. Raymer. *Aircraft design: a conceptual approach*. AIAA education series. American Institute of Aeronautics and Astronautics, Inc., 1992.
- [44] C. E. D. Riboldi and F. Gualdoni. “An integrated approach to the preliminary weight sizing of small electric aircraft”. In: *Aerospace Science and Technology* 58 (Aug. 2016), pp. 134–149.
- [45] W. Johnson. *Helicopter theory*. Dover publications, Inc., 1994.
- [46] P. G. Fahlstrom and T. J. Gleason. *Introduction to UAV systems*. Fourth. Aerospace Series. John Wiley and Sons, Ltd., 2012.
- [47] *UIUC Airfoil coordinates database*. URL: https://m-selig.ae.illinois.edu/ads/coord_database.html.
- [48] B. N. Pamadi. *Performance, stability, dynamics and control of airplanes*. Ed. by J. S. Przemieniecki. AIAA education series. American Institute of Aeronautics and Astronautics, Inc., 1998.
- [49] P. E. Pursee and J. P. Campbell. *Experimental verification of a simplified vee-tail theory and analysis of available data on complete models with vee tails*. Tech. rep. Langley Memorial Aeronautical Laboratory, National Advisory Committee for Aeronautics, 1944.
- [50] H. R. Pass. *Analysis of wind-tunnel data of directional stability and control*. Tech. rep. Langley Memorial Aeronautical Laboratory, National Advisory Committee for Aeronautics, 1940.
- [51] I. G. Recant and A. R. Wallace. *Wind-tunnel investigations of the effect of vertical position of the wing on the side flow in the region of the vertical tail*. Tech. rep. Langley Memorial Aeronautical Laboratory, National Advisory Committee for Aeronautics, 1941.
- [52] R. S. Swanson and S. M. Crandall. *Analysis of available data on the effectiveness of ailerons without exposed overhang balance*. Tech. rep. Langley Memorial Aeronautical Laboratory, National Advisory Committee for Aeronautics, 1944.

- [53] F. Perini. “Structural design, manufacturing and testing of a new wing for the CSIR’s Modular UAS in composite materials”. MA thesis. Alma Mater Studiorum - Università di Bologna, 2012.
- [54] *eCalc website*. URL: <https://www.ecalc.ch>.
- [55] *Dualsky Advanced Power Systems website*. URL: <http://www.dualsky.com>.
- [56] *KDE Direct website*. URL: www.kdedirect.com.
- [57] *Scorpion Power System Ltd website*. URL: www.scorpionsystem.com.
- [58] *MAD Components website*. URL: <http://madcomponents.co>.
- [59] *T Motor website*. URL: <http://store-en.tmotor.com>.
- [60] *Cobra Motors USA website*. URL: <https://www.cobramotorsusa.com>.
- [61] *HobbyKing website*. Jan. 2020. URL: https://hobbyking.com/it_it.
- [62] *Gens Ace and Tattu website*. URL: <https://www.genstattu.com>.
- [63] *Holybro website*. URL: <http://www.holybro.com>.
- [64] *PX4 website*. Jan. 2020. URL: <https://px4.io>.
- [65] *FrSky website*. Jan. 2020. URL: <https://www.frsky-rc.com>.
- [66] *FriendlyElec website*. Dec. 2019. URL: <https://www.friendlyarm.com/index.php?route=common/home>.
- [67] A. J. Keane et al. “Maritime flight trials of the Southampton University laser sintered aircraft - Project Albatross”. In: *The aeronautical journal* 121.1244 (Oct. 2017), pp. 1502–1529.
- [68] M. Ferraro et al. “Design and flight test of a civil unmanned aerial vehicle for maritime patrol: the use of 3D printed structural components”. In: *4th Aircraft Structural Design Conference*. 2014.
- [69] A. Deperrois. *XFLR5: analysis of foils and wings operating at low Reynolds numbers*. 2009.
- [70] B. Etkin and L. D. Reid. *Dynamics of flight: stability and control*. Ed. by C. Robichaud, C. Beckham, and C. Ronda. Third. John Wiley and Sons, Ltd., 1996.
- [71] E. L. Tobias and M. B. Tischler. *A model stitching architecture for continuous full flight-envelope simulation of fixed-wing aircraft and rotorcraft from discrete-point linear models*. Final. U.S. Army Research, Development and Engineering Command, Apr. 2016.
- [72] S. Panza et al. “qLPV modelling of helicopter dynamics”. In: *IFAC PapersOnLine* 52.28 (Dec. 2019), pp. 82–87.
- [73] G. D. Goh et al. “Additive manufacturing in unmanned aerial vehicles (UAVs): Challenges and potential”. In: *Aerospace Science and Technology* 63 (2017), pp. 140–151.

Appendix A

Aerodynamic software considerations

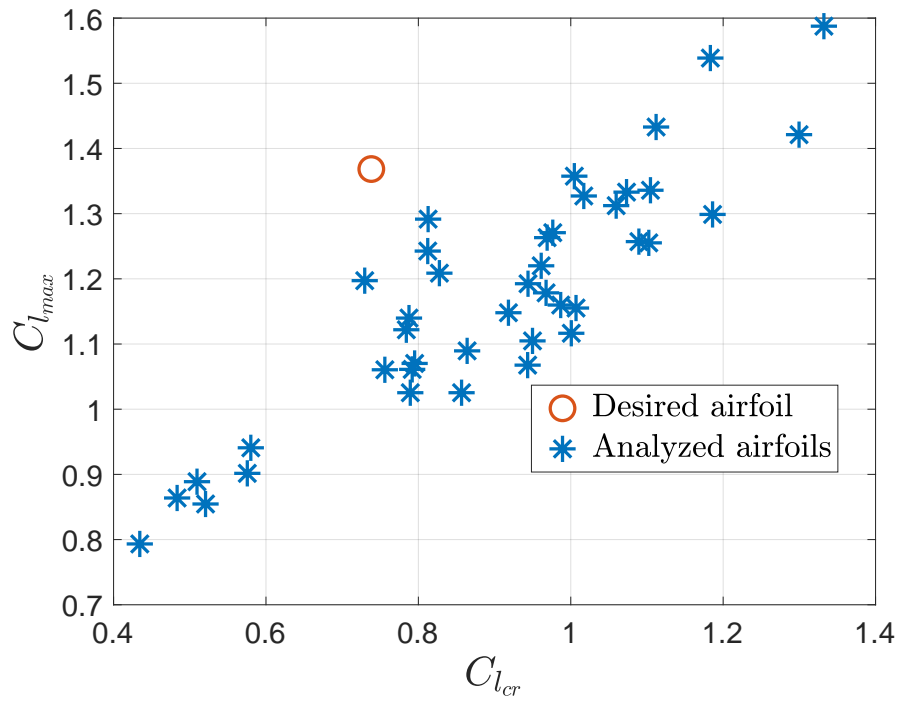
In this appendix a brief explanation of the aerodynamic software used and of its limitations is done. XFLR5 has been developed by André Deperrois to provide a translation of XFOIL by Mark Drela from FORTRAN to C/C++ code with a more user-friendly interface. In several years different components have been added, allowing to compute not only 2D airfoil aerodynamic performance but also 3D performance of complete models. Several methods are implemented in 3D case, such as lifting line theory (LLT) and vortex lattice method (VLM). It is important to state that the code has been intended and developed for the design of model sailplanes, for which it gives reasonable and consistent results. The use of the code for all other purposes, especially for the design of real size aircraft is strongly disapproved from the author. Nevertheless, it can be used for the aerodynamic design since the size and flight conditions of the UAV are not too far from those of large model-aircraft. In 2020 the developer has decided to stop the development of XFLR5, transferring its features to a new software, called Flow5, developed from the beginning with new technologies and increased capabilities (for example the fuselage modeling from STL CAD files and new numerical methods for aerodynamic analysis). For more details about XFLR5 refer to [69].

Appendix B

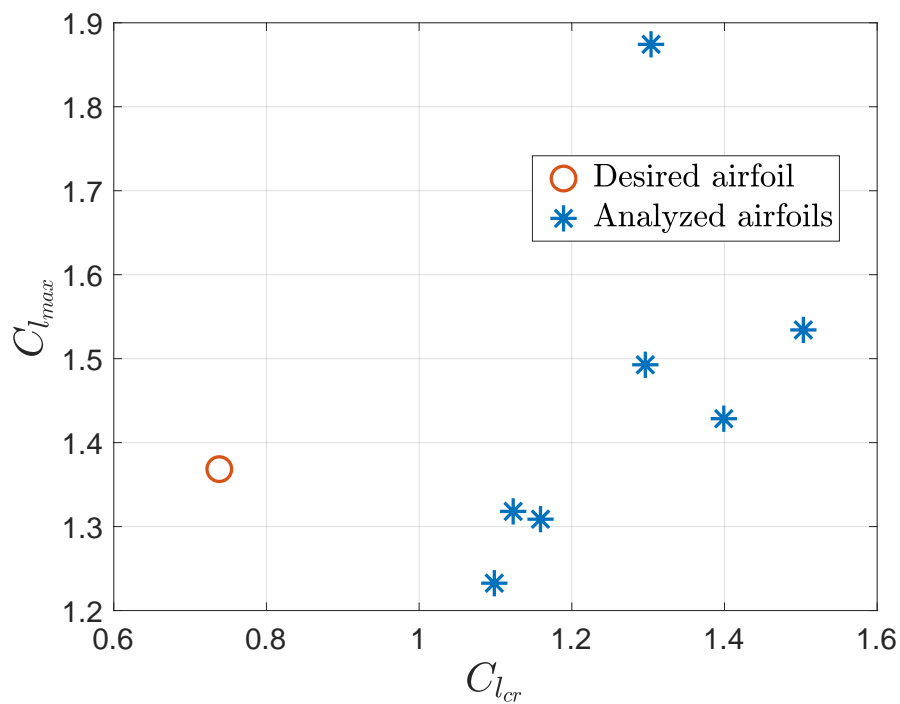
Airfoil simulations

This appendix presents the graphical analysis of the airfoil sections described in Section 2.1. Each airfoil has been simulated using XFLR5 aerodynamic software to compute its maximum lift coefficient $C_{l_{max}}$ and its cruise lift coefficient $C_{l_{cr}}$. These values have been compared with the required ones computed starting from SMP and cruise conditions. In this appendix the graphical comparison of the following airfoil families is presented:

- Eppler airfoils for low Reynolds;
- Eppler airfoils for general purpose;
- Eppler airfoils for general aviation;
- NACA series 4;
- NACA series 5;
- NACA series 6;
- Selig airfoils for low Reynolds;
- Wortmann airfoils for low Reynolds;
- various airfoils for low Reynolds.

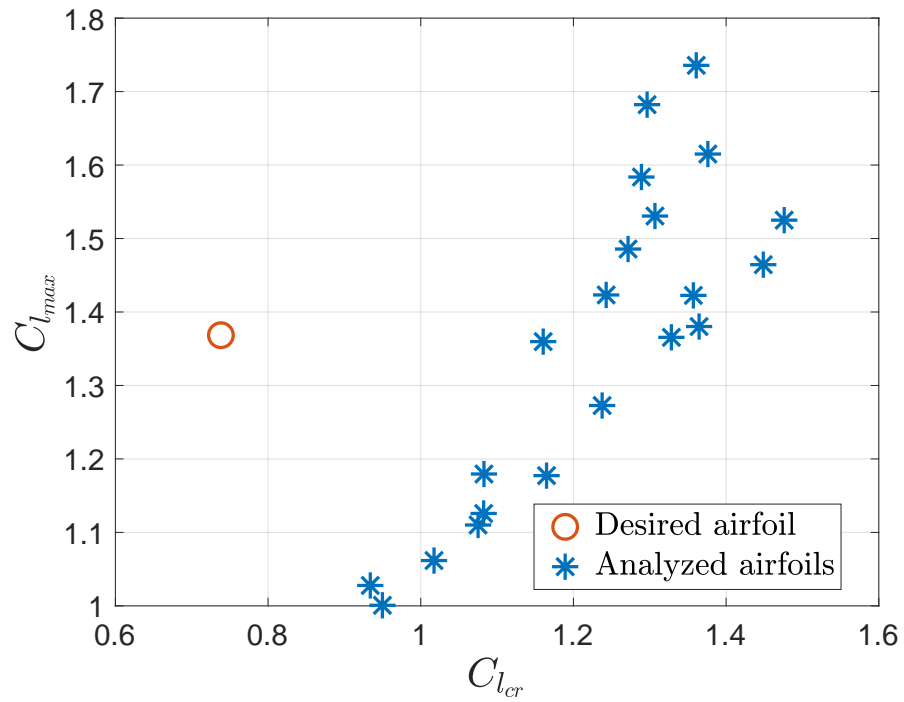


(a) Eppler for low Reynolds airfoils.

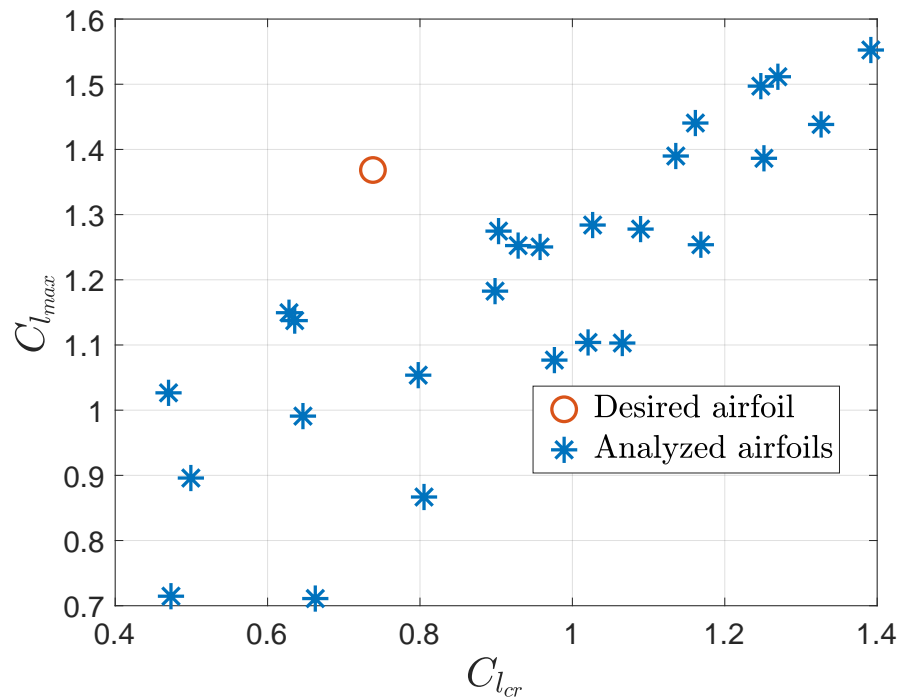


(b) Eppler for low general purpose.

Figure B.1: Airfoil sections analyzed to select the best one; part 1.

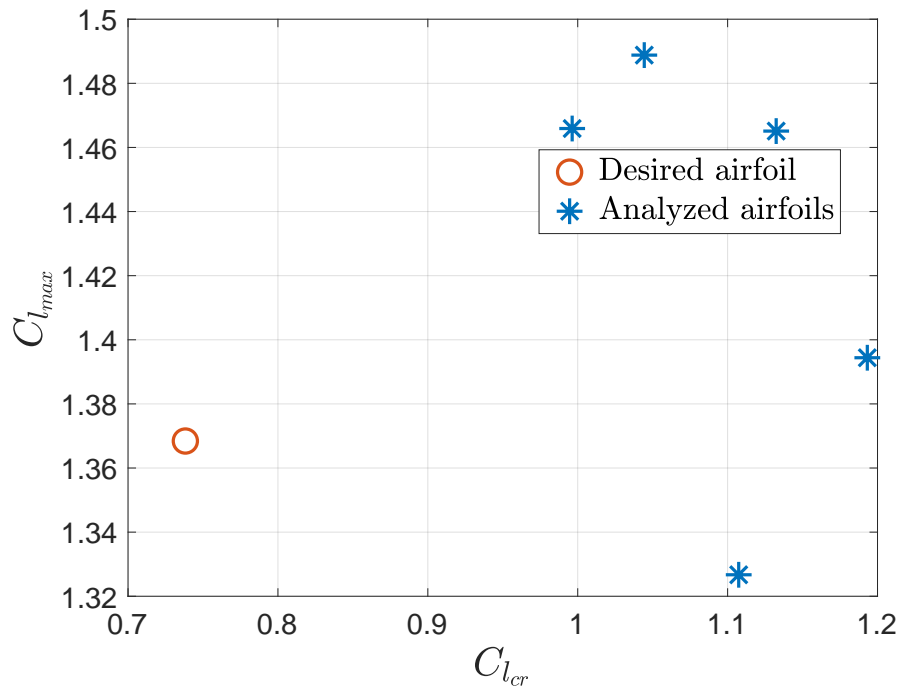


(a) Eppler for low general aviation.

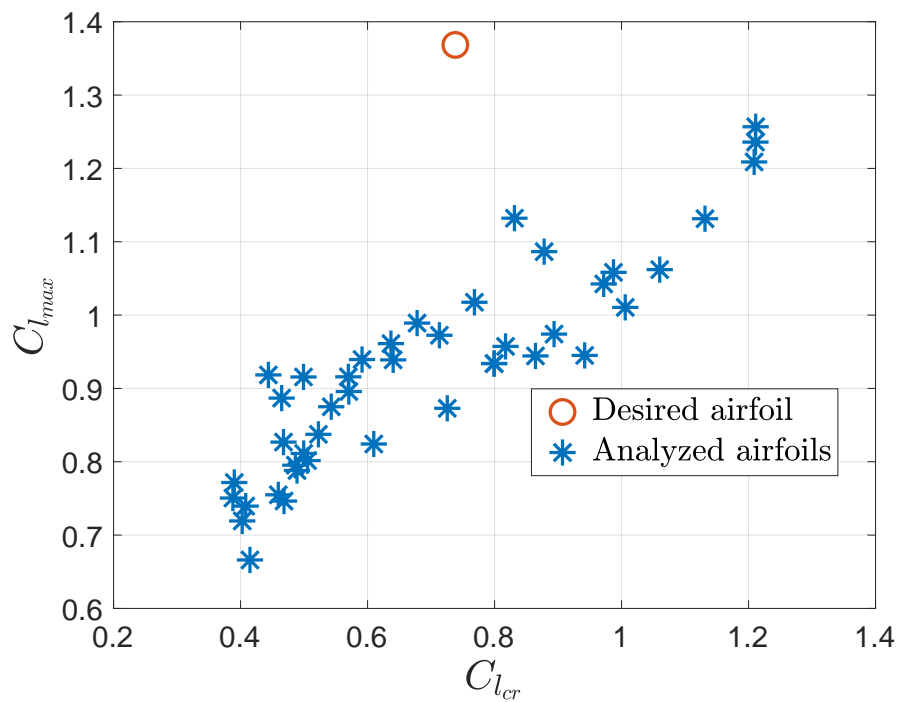


(b) NACA series 4 airfoils.

Figure B.2: Airfoil sections analyzed to select the best one; part 2.

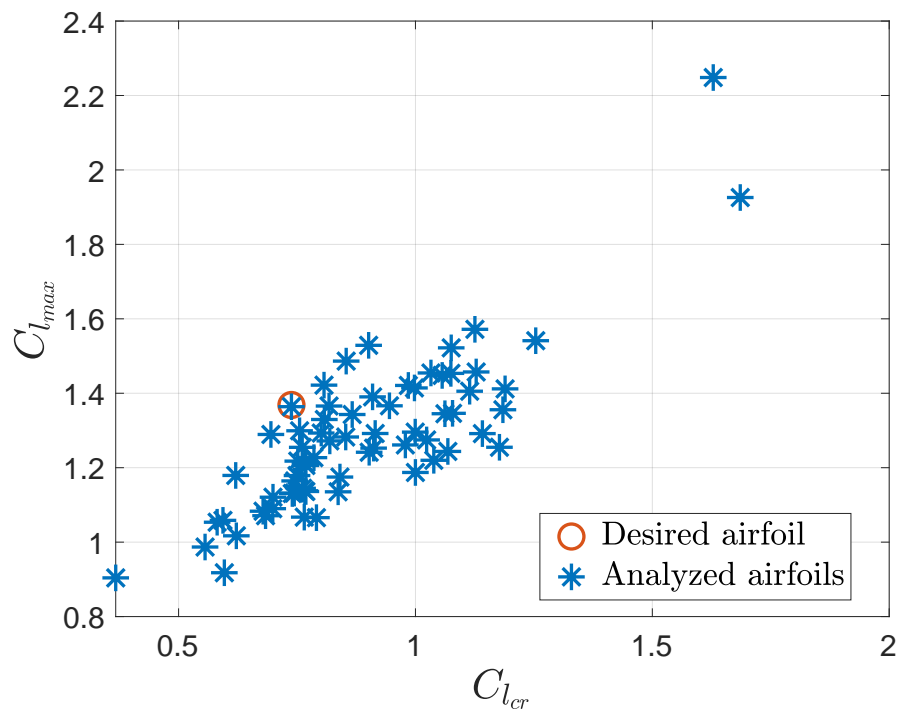


(a) NACA series 5 airfoils.

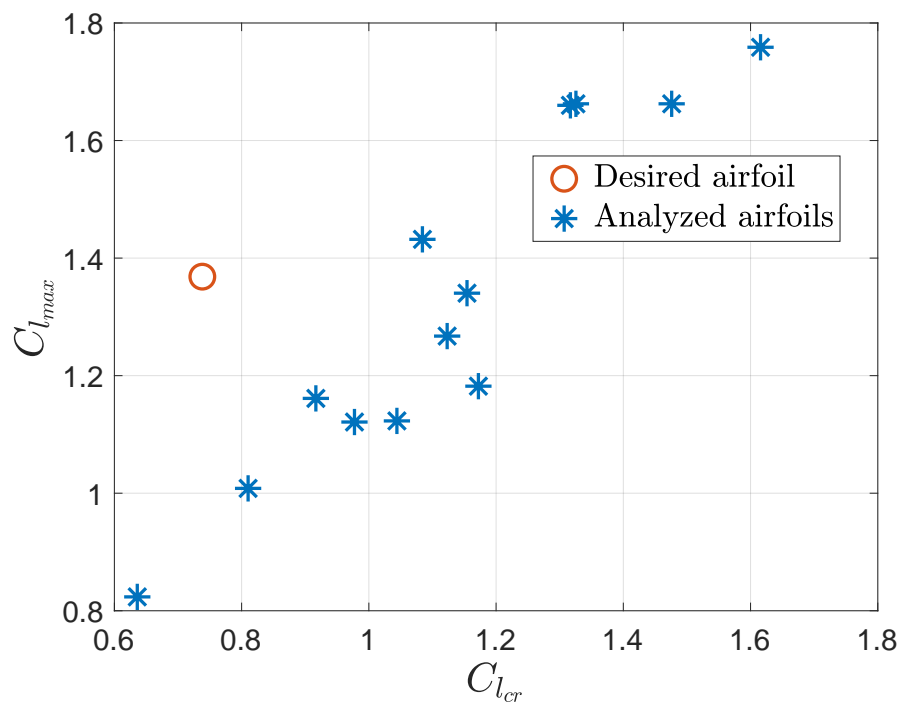


(b) NACA series 6 airfoils.

Figure B.3: Airfoil sections analyzed to select the best one; part 3.



(a) Selig for low Reynolds airfoils.



(b) Wortmann for low Reynolds airfoils.

Figure B.4: Airfoil sections analyzed to select the best one; part 4.

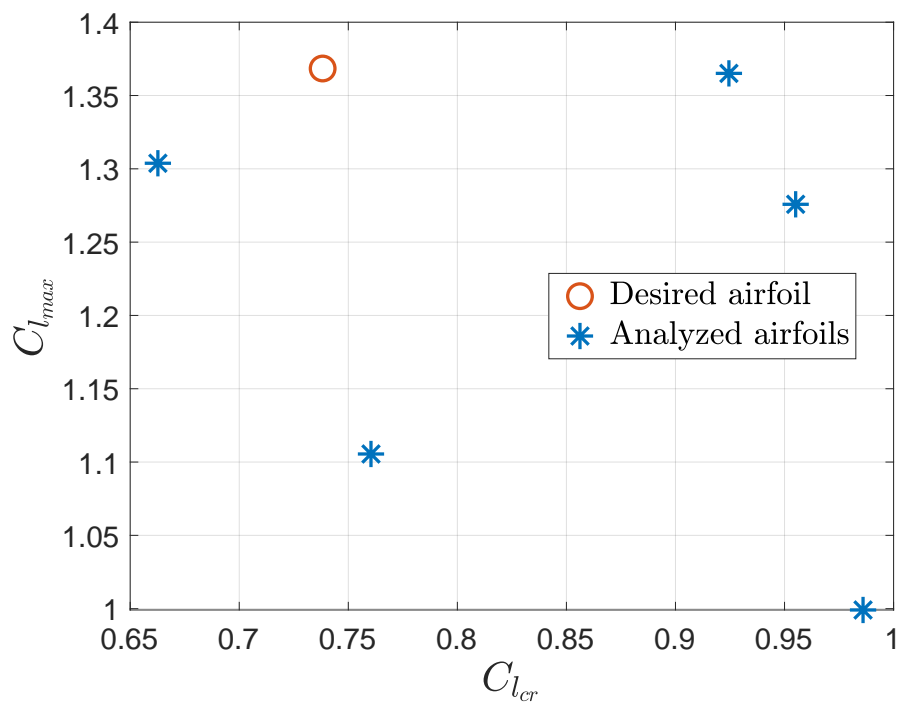


Figure B.5: Various airfoils for low Reynolds.

Appendix C

3D printing technologies

In the design of this VTOL UAV several additive manufacturing (AM) technologies have been considered, in particular 3D print. They have been considered since, with respect to conventional methodologies such as composite materials or metallic structures, allows to the designer to optimize better the structure and produces more innovative layouts (reference [73]). Moreover, 3D printing allows to the designer to refine each component easily with CAD software and, virtually, until a short time before assembly of the aircraft (based on the AM typical production time), as highlighted in [16]. It is important to state that, given the small scale of the UAV, the structural loads are limited.

Starting from a literature survey, two main alternatives have been adopted for the components of the VTOL UAV: fused deposition modeling (FDM), which uses ABS or PLA filaments, or selective laser sintering (SLS) of nylon powder. These two AM methodologies have been implemented in [16], [67] and [68] to build several UAVs. In the following a brief presentation of both these technologies is done, presenting their pros and cons.

The FDM technology is based on the deposition of a heated plastic filament to reproduce the desired shape. The plastic filament is heated passing through a nozzle; in this way it is in semiliquid form when deposited on the base of the printer. The basement plate is fixed and the nozzle moves on top of it following the geometrical coordinates that produces the desired shape. When the filaments cool down they are welded together into one solid object. Figure C.1 presents the scheme of FDM technology. According to [16] it is suitable for non structural components. The main disadvantage of this technology is that it provides a poor surface finish and there is a stair stepping effect which highlights the layers in the vertical direction. FDM components can be printed inside the DAER facility with a $20 \times 20 \times 22$ cm print, so this technology can be used for components of small dimensions.

The SLS technology works by fusing of small powder with a laser; the fine-grained powder can be stainless steel or nylon (as adopted in the design of the VTOL UAV and in [68], first UAV entirely manufactured in SLS nylon). The laser

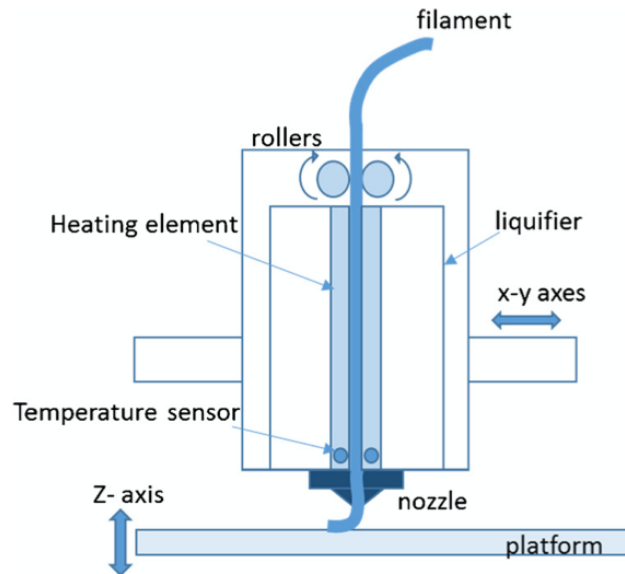


Figure C.1: FDM printing technology scheme, source [73].

fuses the powder only in the points required to build the 3D shape, the remaining powder acts as a support for the already built part. At the end of the process it is important to remove the unused powder to avoid useless weight and save material for future works. To make this process easy it is important to avoid enclosures, so all the internal powder can be removed. According to [16] SLS nylon can be used for structural components, as successfully established in [67] and [68]. Figure C.2 presents an example of SLS manufacturing. The SLS process, according to [73], allows to produce components with good mechanical strength and with large dimensions; however, the external surface can present a rough finish that requires a post-processing polishing. At the time of this work there is no SLS printer inside the DAER laboratories, so every component produced with this technology have to be outsourced.

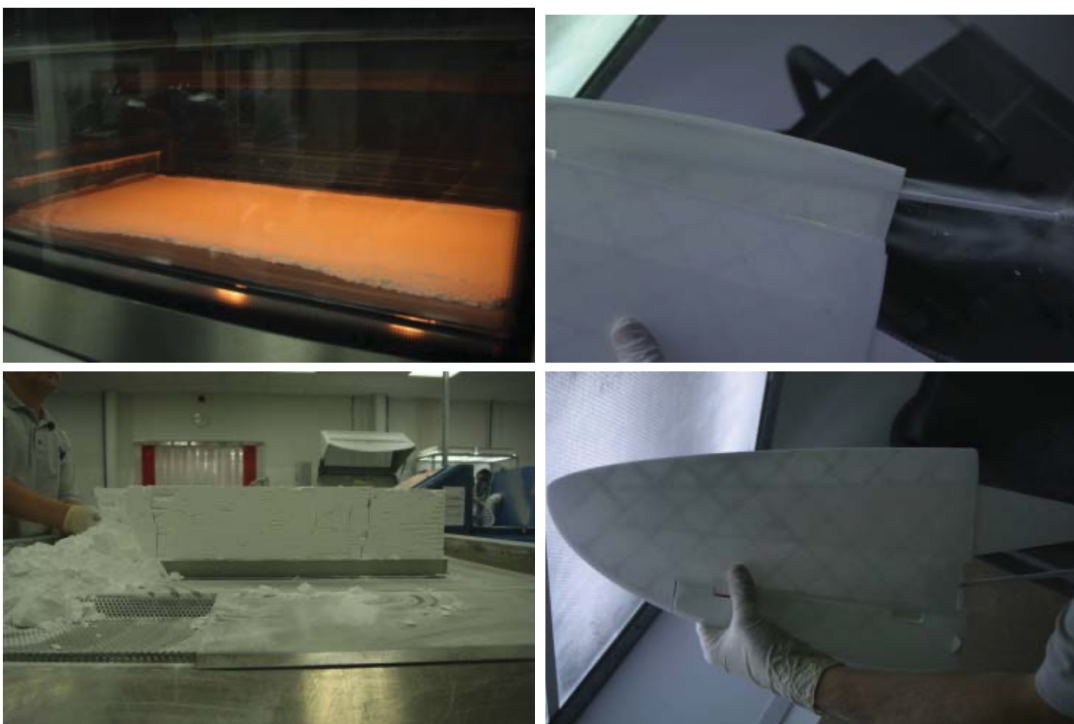


Figure C.2: SLS manufacturing (left column) and depowdering (right column), source [16].

